Physical Foaming of a Thermoplastic Elastomer (Styrene-Isobutylene-Styrene Copolymer) − Microcellular Foam Injection Molding and Stretching-Induced Foaming Methods

Lin Weiyuan

2023

Table of Contents

Chapter 1 Introduction

1.1 Polymer Foaming

Polymer foaming is a specific direction which has been drawing much attention in field of material processing, aiming to fabricate a new light-weight material of various properties. These properties include thermal and sound insulation,[1-8] enhanced mechanical properties,[4,9-11] and energy absorption[12-13]. Based on these properties, polymer foams have been widely used in our daily life. For example, as one of the most common polymer foams, Polypropylene (PP) foams have a variety of applications in areas of packing, automotive, construction, acoustic and thermal insulators.[14-15] Polyurethane (PU) foams, as a type of elastomer foam, have been used in sporting, furniture cushions, shock absorbents, etc.[12,14,16-17] As a recent focused topic, foaming of thermoplastic elastomer is discussed in Chapter 2.

1.2 Foaming Mechanism

The basic mechanism of foaming can be attributed to two aspects: cell (bubble) nucleation and cell growth. According to classic nucleation theory (CNT),[18-19] homogeneous nucleation of cells in polymer foaming involves two types of energy difference: one is the volume energy change and the other one is surface energy change.[17] Assume the cell nucleus is spherical with a radius *R*, the total free energy of homogenous nucleation (ΔG_{hom}) can be expressed as:

$$\Delta G_{hom} = -\frac{4}{3}\pi R^3 \Delta P + 4\pi R^2 \gamma_{gl} = -\frac{4}{3}\pi R^3 (P_{cell} - P_{sys}) + 4\pi R^2 \gamma_{gl} \qquad (1\text{-}1)$$

where P_{cell} and P_{sys} are the pressure inside and outside the cell respectively. γ_{gl} represents the surface tension. The differentiation of Eq. (1-1) gives the critical radius (R_{cr}^*) in Eq. (1-2), which is key factor in cell nucleus growth:[18,20]

$$R_{cr}^* = \frac{2\gamma_{gl}}{\Delta P} = \frac{2\gamma_{gl}}{P_{cell} - P_{sys}} \qquad (1\text{-}2)$$

By substituting Eq. (1-2) into Eq. (1-1), expression of energy barrier of homogenous cell nucleation ΔG_{hom}^* without radius can be obtained in Eq. (1-3):

$$\Delta G_{hom}^* = \frac{16\pi\gamma_{gl}^3}{3(P_{cell} - P_{sys})^2} \qquad (1\text{-}3)$$

In heterogenous system, a geometrical factor $F(\theta_c, \beta)$ that dependent on surface geometry of nucleating agents, is added to Eq. (1-3), the energy barrier of heterogenous cell nucleation can be expressed as:

$$\Delta G_{het}^{*} = \frac{16\pi\gamma_{gl}^{3} F(\theta_c, \beta)}{3(P_{cell} - P_{sys})^2} \tag{1-4}$$

where θ_c represents the contact angle between cell surface and nucleating agent surface measured in the polymer phase, and β is related to the surface geometry of nucleating agent. The expression of $F(\theta_c, \beta)$ is expressed in Eq. (1-5):[17,20-21]

$$F(\theta_c, \beta) = \frac{1}{4}\left\{2 - 2\sin(\theta_c - \beta) + \frac{\cos\theta_c \cos^2(\theta_c - \beta)}{\sin\beta}\right\} \tag{1-5}$$

Classic nucleation theory is originally used to understand nucleation in solid or liquid,[22] and has been facing challenges in further application for polymer foaming. More and more studies have been done to modify the mechanism of polymer foaming. According to Albalak et al.,[23] it was firstly found that growth of a nucleated cell can induce the tensile stress, which is beneficial for local pressure decrease and further cell nucleation in the surrounding regions of that nucleated cell. Yarin et al.[24] also claimed that mechanical degradation near the primary cells could facilitate the nucleation of secondary cells. Based on the literatures from Park et al.,[21,25-28] a local pressure variation (ΔP_{local}) was used in modification of degree of supersaturation (ΔP), which is shown below in Eq. (1-6):

$$\Delta P = P_{cell,cr} - (P_{sys} + \Delta P_{local}) \tag{1-6}$$

where $P_{cell,cr}$ is the critical pressure in the cell at the moment of nucleation. ΔP_{local} represents the pressure difference between actual pressure near the nucleating sites and system pressure P_{sys} (i.e. pressure outside the cell). Thus, the critical radius, homogeneous cell nucleation barrier, and heterogeneous cell nucleation barrier, are changed into:

$$R_{cr}^{*} = \frac{2\gamma_{gl}}{P_{cell,cr} - (P_{sys} + \Delta P_{local})} \tag{1-7}$$

$$\Delta G_{hom}^{*} = \frac{16\pi\gamma_{gl}^{3}}{3\left[P_{cell,cr} - \left(P_{sys} + \Delta P_{local}\right)\right]^2} \tag{1-8}$$

$$\Delta G_{het}^{*} = \frac{16\pi\gamma_{gl}^{3}F(\theta_c,\beta)}{3\left[P_{cell,cr} - \left(P_{sys} + \Delta P_{local}\right)\right]^2} \quad (1\text{-}9)$$

By introducing ΔP_{local} into the expression of degree of saturation, Park et al.[21,28] found that ΔP_{local} would be negative with presence of tensile stress in the local region, resulting in increased overall degree of surpersaturation and reduced cell nucleation barrier. On the contrary, ΔP_{local} would be positive when there is a compressive stress, leading to increase in cell nucleation barrier. Furthermore, they reported tensile stress would exist in the local regions surrounding the nucleating agents.[21,27]

Besides, there are studies focusing on the effect of external force on cell nucleation, which will be described in Chapter 4.

For cell growth, the driving force can be divided in two aspects: mass transfer of gas molecule and momentum transfer between the cell and polymer/gas phase.[17] In general, P_{cell} is high at the very start of cell growth because of small size. Since the pressure in the polymer/gas phase is much lower, the gas concentration gradient induces gas diffusion from cell interface into cell. In addition, P_{cell} will decrease when the cell grows in size, which makes cell growth more diffusion-driven.

1.3 Various Foaming Technologies

In general, polymer foams are mainly fabricated by chemical foaming and physical foaming where blowing agents are generated in different ways. Typical foaming process with blowing agents can be summarized in four steps: first, gas sorption leads to formation of single-phase polymer/gas mixture; second, thermodynamic instability is triggered by pressure drop or temperature increase to initiate the cell nucleation. Third, growth of nucleated cell happens due to gas diffusion, and finally cellular structure is stabilized by cooling. Foaming processes of chemical and physical foaming are shown in Figure 1. 1.

In chemical foaming, chemicals that produce gas due to thermal decomposition or chemical reactions, participate in foaming process as blowing agents. The chemical blowing agents (CBAs) are classified into two types: inorganic and organic foaming agents. Inorganic blowing agents such

as sodium bicarbonate can generate CO_2, [14, 29-30] which can decompose at relatively mild temperature range (145-150 ℃).[31] Besides, zinc carbonate is another well-known carbonate blowing agent that produce CO_2.[31] Except for CO_2, H_2 has also been attractive in chemical foaming, where borohydrides (e.g. $NaBH_4$) and hydrides (e.g. MgH_2) are usually used in hydrogen releasing.[31] Organic chemical blowing agents have also been used in chemical foaming process, including well-known azodicarbonamide (ADC) and its blend, which produce carbon dioxide, carbon monoxide, nitrogen, and ammonia when heated up (generally decompose at 230 ℃).[31] Compared with physical blowing agents (PBAs), the benefits of using CBAs include: 1) no specific storage equipment is required because they are usually solid; 2) Diffusion of CBAs is easier to control because they can directly produce gases in the material; 3) The physical state of CBAs is not affected by pressure.[31-32] Despite aforementioned advantages, application of CBAs is limited for several reasons, compared with that of PBAs. First, more cost is required for CBAs than PBAs from a gas cylinder when preparing a foam of same density.[33] Second, by-products produced from incomplete decomposition of CBAs may affect the performance of final foam products. Third, organic CBAs can be harmful to the environment.

In comparison to chemical foaming, physical foaming, is more widely used in foam industry, where green PBAs such as CO_2 and N_2 are usually used. There are various processing techniques that have been developed for physical foaming, including batch foaming, foam extrusion, foaming injection molding and bead foaming. In batch foaming, saturation pressure, saturation time and temperature can be adjusted to control the foaming process. Due to adjustable saturation time, PBAs of high concentration can be dissolved into the material even at low temperature, which results in higher cell density and smaller cell size.[34] However, long saturation time before depressurization leads to long experiment and production cycle. In addition, shape of products is also confined.[35]

As the only way to obtain foams with very low density of various shapes, bead foaming has been gaining a lot of attention, especially in automotive industry. There are two methods of fabricating foamed bead, according to literatures.[36] The first one is to prepare expandable beads that must be pre-expanded. This method can be used in fabrication of foamed beads of amorphous thermoplastic polymer (e.g. polystyrene (PS)), since blowing agent is trapped in the polymer below T_g. Then the gas-laden expandable beads are expanded in pre-expansion step, prior to the sintering

step. The second one is to prepare expanded beads, which mainly focus foaming of semi-crystalline polymer (e.g. PP). Due to presence of crystalline structure, the blowing agent cannot be stored in the polymer.[37] After saturated with the blowing agent, the material is released to an expansion vessel. Finally, the beads are washed by water and cooled down to stop the expansion.[36-38]

Different from batch foaming and bead foaming, foam extrusion is an alternative to prepare foams by melt processing. PBAs are firstly injected into molten polymer, and then mixed with polymer to produce polymer/gas homogeneous phase by a distributive mixing screw. Subsequently, polymer/gas phase is cooled and stabilized. Stabilized polymer/gas phase is afterwards transferred to shaping units where foaming happens.[39]

Foam injection molding (FIM) is a combination of foam extrusion and injection molding process, which has been widely studied and used academically and industrially due to customizable shape, low cycle time and high dimensional stabliliy.[14,15, 39-40] Polymer/gas phase is injected into mold cavity where foaming occurs. After solidification in the mold cavity, foam of designated shape can be obtained. Detailed information about setup of foam injection molding can refer to the literatures.[39,41] Since the dimension of mold is unchanged, in order to fabricate high-expansion foams, foam injection molding incorporating with core-back technique has been developed. In this technique, space in the mold cavity is increased for foam expansion.[5, 42] In spite of promising future of foam injection molding, the major issue of injection-molded foam is low surface quality, which will be further discussed in Chapter 3.

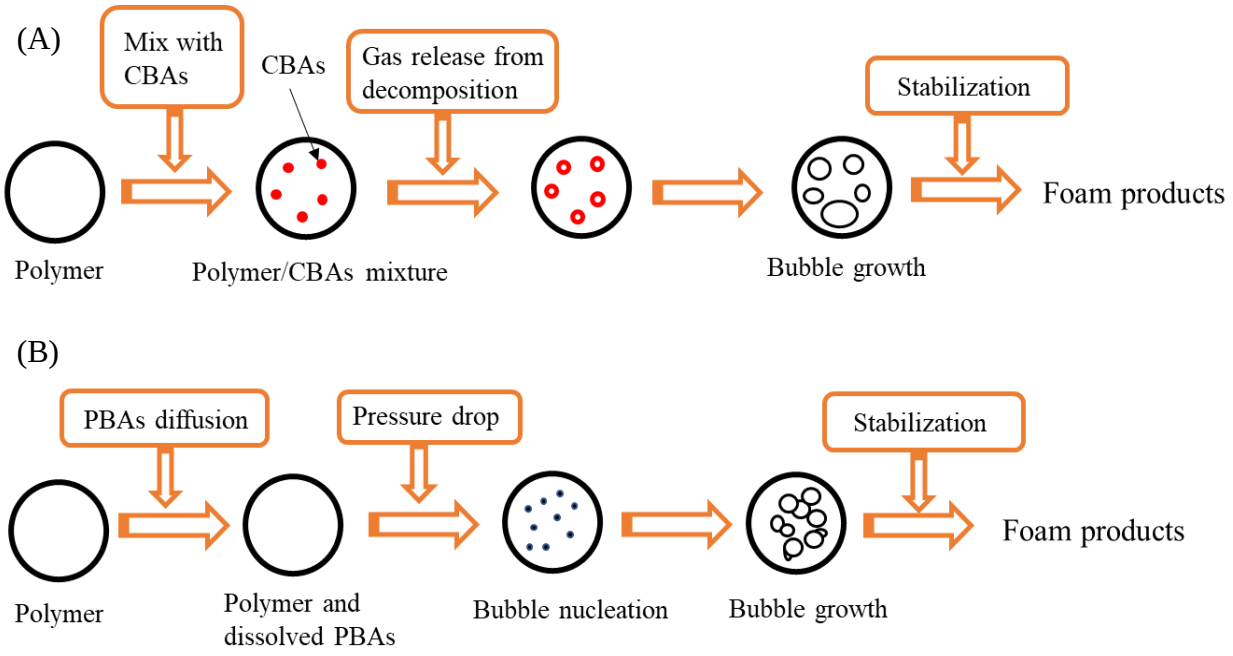

Figure 1.1 Schematic representation of (A) chemical and (B) physical foaming processes.

1.4 Microcellular Foam

1.4.1 Performances of Microcellular Foam

Properties of microcellular polymer foams vary in terms of diverse cellular structure. In order to judge the quality of microcellular polymer foams, performances such as expansion ratio, cell density and cell diameter are usually evaluated. High expansion ratio represents high weight reduction and low material cost, which has been one of desired properties of microcellular foams. However, high expansion ratio can result in low cell density and large cell size, and thus reduced mechanical properties (e.g. compressive strength[43]). Cell density and cell size are generally considered as key features of foam morphology. Generally, inverse relationship between cell density and cell size is observed in microcellular foaming. Microcellular polymer foams are usually characterized by cell density greater than 10^9 cells/cm^3 and cell diameter less than 10 μm.[11, 44] Significantly, small cell size represents thick cell wall, which may lead to improved mechanical properties. For instance, Rachtanapun et al.[45] found cell morphology had strong connect with the impact strength, where finer cell morphology induced higher impact strength. Bai et al.[46] reported

that they prepared PS foams with high cell density and small cell size by compressive-injection molding with core-back foaming strategy. Enhanced tensile and impact strength were observed for foams with high cell density, small cell size.

1.4.2 Strategies and Progress in Polymer Foaming

In order to improve the foamability of polymer, modification of rheology and crystalline structure are commonly considered. For instance, foaming of semi-crystalline PP has been challenging due to poor melt strength and low viscoelasticity.[47] In order to solve this problem, crystal nucleating agents are introduced to enhance the heterogeneity and promote the formation of crystal region. The close packing of molecules and high intermolecular forces[39] in highly-organized crystal regions can impede the formation of bubble and detach the dissolved gas, which induce high pressure in the surrounding area and thus induce bubble nucleation.[48] Thus, the crystals can play the role in bubble nucleating sites. In addition, the local stresses induced by chain movement (especially tensile stress) when crystallization happens may further increase the supersaturation level and possibly cause formation of microcavities.[28] Thus, cell nucleation around the crystals occurs.

Based on this point of view, crystal nucleating agent including inorganic and organic can be employed to improve the foamability. Inorganic fillers such as talc, clay or glass fiber have merits as crystallization nucleating agent, such as low cost and [49,50] Hou et al.[49] reported they prepared PP/talc foam with high weight reduction by mold-opening microcellular injection molding. It was claimed that though talc could promote the PP crystallization with a small amount, over 10 wt.% was required for viscoelasticity improvement. Zhai et al.[50] successfully fabricated PP/clay nanocomposites foams with high expansion ratio of 18 and high cell density. The presence of nanoclay led to increase in melt viscosity and number of heterogeneous sites. Yang et al.[51] prepared microcellular injection-molded foam with PP/glass fiber. It was reported that glass fibers could reduce the crystallization temperature and enhanced the polymer viscosity. In addition, mechanical properties (e.g. tensile modulus, bending modulus) were increased significantly. Organic fillers such as polytetrafluoroethylene (PTFE), 1,3:2,4 bis-O-(4-methylbenzylidene)-D-sorbitol gelling agent (MD) are also effective crystallization agents in polymer foaming. Zhao et al.[47] introduced PTFE fibrils to linear PP foaming. They found that PTFE fibril was effective to

increase the crystallization rate, reduce the crystal size. Besides, viscoelasticity could be also promoted, and remarkable strain hardening behavior was induced, which were beneficial for microcellular foaming. Interestingly, the incorporation of talc and PTFE in PP foaming was reported by Zhao and Zhao[52] recently, where lightweight PP/talc/PTFE foam with excellent flame-retardant function was successfully fabricated. Miyamoto and Ohshima[53] used MD as crystal nucleating agent for preparation of micro/nanocellular PP foam. With addition of only 0.5% MD, PP foam with high cell density, small cell size and high open cell content was obtained. In short summary, these studies profoundly show the high effectiveness of such fillers, and promising future of novel polymer foam.

Except for introduction of fillers, incorporating the long-chain branches is another way to increase the melt strength of polymer. According to the literatures,[42,54] strain hardening property induced by long-chain branches is beneficial for reduction of cell size and narrowing of cell distribution. This year, Embabi and Lee[55] revealed an interesting, novel and cost-effective route to prepare PP foams, instead of introducing long-chain branches. In their study, foamability of linear PP ionomer was clarified. Strain-hardening property was enhanced even at very low level of ion contents (<0.1 mol %).

Foaming of amorphous polymer is slightly different from foaming of semi-crystalline polymer due to absence of crystalline structure. Thus, glass transition temperature (T_g) is a key temperature that impacts on the foaming process. Krause et al.[56] successfully prepared microcellular foam of amorphous polymer with high glass transition temperature (T_g) with CO_2. It was claimed that foaming was strongly dependent on the T_g. In order to enhance the foam performance (i.e. cell density, cell size) of amorphous polymer (e.g. PS, PMMA), blending can be an effective way to improve the cell nucleation by forming sea-islands structure. For example, Qu and Wang[57] blended PS with thermoplastic polyurethane (TPU) of 10, 15 and 20% content and prepared microcellular foam by batch foaming. The introduction of 5% TPU was claimed to be beneficial for enhancement of cell nucleation. Interestingly, bimodal cell structure was observed when TPU content was over 5%, according to their results. According to the previous report in our lab, Sharudin and Ohshima[58] introduced PP into amorphous PS and PMMA as cell nucleating agent and successfully increased the cell density and reduced the cell size. PP could be excellent nucleating agent with good dispersibility.

Introduction of filler can be an alternative to fabricate amorphous polymer foam of multi-function. Zhao et al.[59] reported an ultra-light, super-insulating PS/carbon nanofiber (CNF) nanocomposite foam prepared by microcellular foaming. It was demonstrated that CNF could improve the T_g, rheological properties and the foamability. In addition, mechanical properties and thermal insulation performance were improved. Gong and Park[60] developed a novel bimodal PS foam with addition of multi-wall carbon nanotube (MWCNT) which had low thermal conductivity of 30 mW/m-K without employing any insulation gas. They clarified the increased efficiency in infrared absorption with increasing MWCNT concentration. Other filler such as graphene,[61,62] graphite[63] and carbon black[64] have been also used as reinforcing agents, which give alternatives to produce foams with diverse functions.

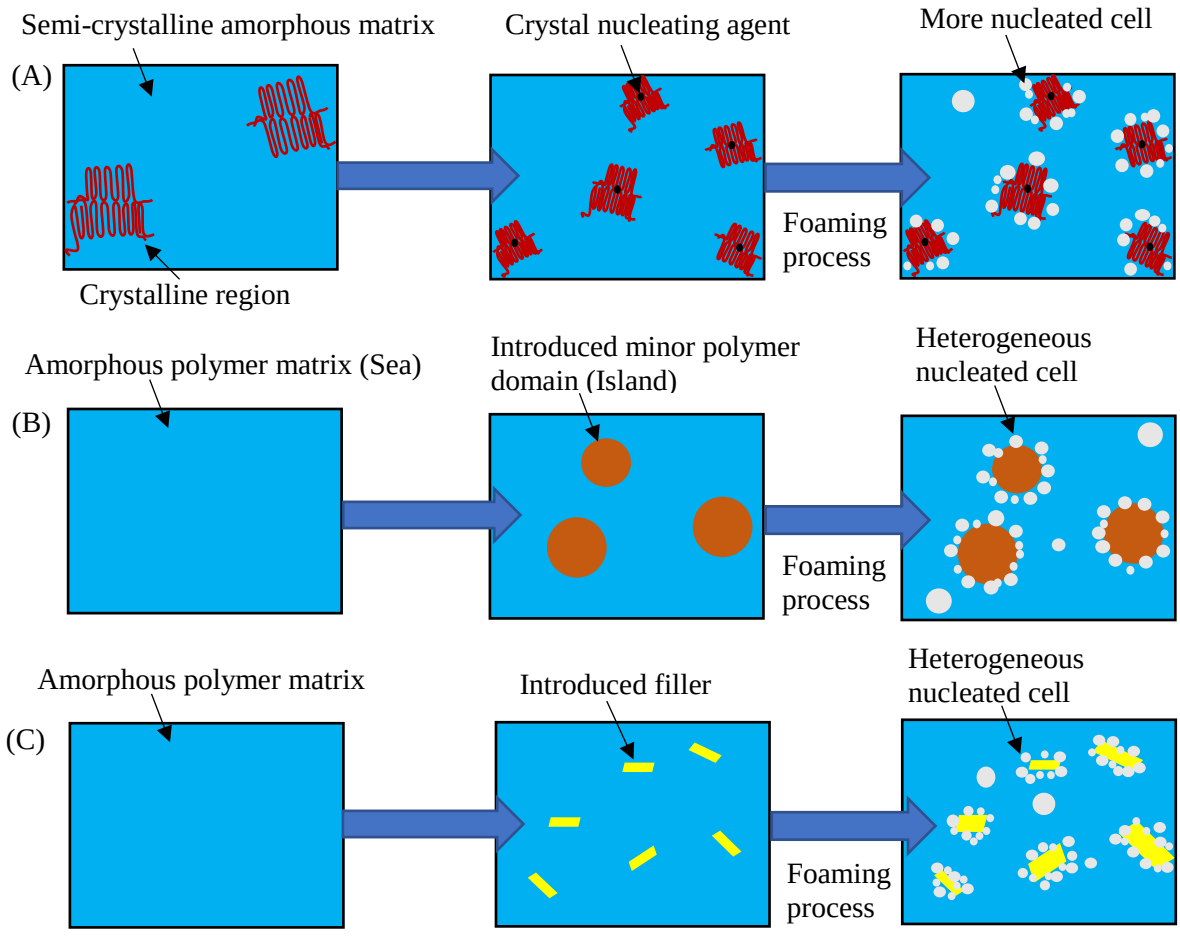

Figure 1.2 Schematic diagrams of various strategies for improving the foamability: (A) Addition with crystal nucleating agents; (B) Blended with minor polymer to form sea-islands structure; (C) Addition with filler to increase the heterogeneity.

1.4.3 TPE Foaming

Thermoplastic elastomer (TPE) is a type of new polymer which consists of hard segments and soft segments. It is believed that this micro-phase separation structure leads to ease of processing.[7,] The hard segments generally work as physical crosslink site to form a three-dimensional network, while the soft segments endow high flexibility. Furthermore, the deformability of hard segments enables controllable and reversible transformation of physical crosslink network under thermal treatment (e.g. melt processing), which is beneficial for foaming of TPE. In fact, the successful application of TPE foams in sports field[12] (e.g. sports shoes[65]) has proven the advantage of TPE foaming. To further explore the possibility and application of TPE foams, many new TPE foams have been studied. For example, thermoplastic polyether ester elastomer (TPEE) is one of potential candidate for TPE foaming, with excellent mechanical strength at low temperature. Jiang et al.[66] prepared foams of TPEE by batch foaming and investigated the effect of chain topology and molecular structure on foamability improvement. According to their report, they modified TPEE with chain extenders and chain branching modifiers, to tune the rheological properties, crystallization properties and foamability. As a result, branched structure was found to be effective in fabricating high-expansion foam with improved cell structure. Poly(ether-block-amide) (PEBA) is another type of TPE which has been attractive due to its superior elasticity and flexibility, and stable mechanical properties under different temperatures.[5] To develop a novel PEBA-based material with various functionalities such as insulation, foaming is a promising method. Wang et al. successfully prepared PEBA foams with super elasticity and excellent thermal-sound insulation by mold-opening foam injection molding.[5] Besides, foamability and crystallization kinetics of PEBA were also studied by adjusting the amount of crystalline hard segments (i.e. polyamide blocks) by Barzegari et al.[67] It is believed that the hard segment crystals can be act as heterogeneous nucleating sites in the foaming process.[68]

Different from those TPES which has crystalline hard segments, thermoplastic styrenic elastomers (TPSs) are a group of elastomers in which non-crystalline polystyrenes act as rigid hard segments. TPSs mainly includes styrene-butadiene-styrene copolymer (SBS), styrene-isoprene-styrene copolymer (SIS), styrene-ethylene-butylene-styrene copolymer (SEBS), and styrene-isobutylene-styrene copolymer (SIBS).[69] Compared with other styrenic elastomers, SIBS is the one which has been commercially developed in recent years by Kaneka Corporation, with super

elasticity, excellent heat aging resistance, superior gas barrier ability, and damping behavior.[70-72] These features allow a wide range of demanding application of SIBS, such as packing material, sports equipment, automobile parts. In addition, the high biocompatibility of SIBS makes it promising for biomedical application.[70,73] To further exert the potential of SIBS, foaming is an effective way to produce novel materials based on SIBS.

Table 1.1 Composition of different grades of SIBS from Kaneka Corporation[71]

Grade of SIBS	Molecular Weight	Styrene content (%)	Isobutylene content (%)
SIBS062M	Low	23	77
SIBS062T	Low	23	77
SIBS072T	Low	23	77
SIBS073T	Low	30	70
SIBS102T	High	15	85
SIBS103T	High	30	70

1.5 Dissertation Overview

As discussed in Section 1.3, as one of developed foaming techniques, FIM has been popular in both academic and industrial area. The merits include short cycle time, less material usage, and higher dimensional stability of the foams, which is favorable to massive production. By incorporating the green physical blowing agents (e.g. N_2, CO_2) as mentioned above, and adjusting the operation conditions, physical foaming of polymer can be successfully achieved.

This dissertation aims to focus on the production of TPE foams with desirable performance with N_2 or CO_2 by foaming injection molding. However, there are some critical issues of injection-molded elastomer foam products. First, TPEs usually have a slow crystallization rate or no crystallization rate,[5] inducing ununiform cellular structure and limited foamability that hinder the performance and application in industry. Moreover, the shrinkage has been one of the critical issues of injection-molded TPE foams. Second, the surface imperfections of injection-molded foam (e.g. PP foam), which significantly impedes the industrial application.

The TPE used in this dissertation is SIBS. The reason for choosing SIBS is that, it has many advantages as mentioned in previous section. These advantages endow the potential application of SIBS foams. Based on this concept, physical foaming of SIBS is conducted and several issues concerning SIBS are investigated, in order to realize the commercialization and application of SIBS and corresponding foam products in industry.

In Chapter 2, PP is blended with a type of amorphous thermoplastic elastomer SIBS to improve the foamability and cellular structure. In this case, foam injection molding process with high pressure is employed. PP which acts as crystallization and cell nucleating agent, is added into SIBS matrix to form a see-island blend morphology. The resultant SIBS/PP blend foams not only has higher cell densities and smaller cell sizes, but also possesses higher shrinkage resistance, compared with neat SIBS foam. These results also reveal an effective method of polymer blending to modify the cellular structure and also reduce the shrinkage of other TPEs.

To address the second issue, we introduced SIBS, low-modulus PP (LMPP) and crystal nucleating agent MD to improve surface quality of PP foams from material property perspective. SIBS can work as a kind of heterogeneity in HPP matrix and control the viscosity. LMPP has very low tacticity and consists of a branched chain structure, which can be helpful to reduce crystallization. On the contrary, MD can be favorable to promote the crystallization. In Chapter 3, the efficacy of SIBS, LMPP and MD on surface quality improvement will be clarified.

In Chapter 4, stretching-induced foaming of CO_2-laden SIBS is introduced. As mentioned above in Chapter 2, high pressure is applied to foam SIBS. However, due to the low gas permeability property of SIBS[73] especially when it solidifies, foam injection molding with low pressure is not sufficient for microcellular foam production. It is found that CO_2 can be trapped in the SIBS in the injection molding process. Thus, stretching is utilized to foam the CO_2-laden SIBS parts successfully, and stretching-induced foams are compared in terms of different gas pressures, stretching rates and strains.

Lastly in Chapter 5, summary of the results in this dissertation are shown. Moreover, future prospects of physical foaming focusing on thermoplastic elastomer are discussed.

References

[1] Wang, G.; Zhao, J.; Mark, L. H.; Wang, G.; Yu, K. Wang, C.; Park, C. B.; Zhao, G. Ultra-Tough and Super Thermal-Insulation Nanocellular PMMA/TPU. *Chem. Eng. J.* 2017, 325, 632–646.

[2] Gong, P.; Wang, G. Tran, M. P.; Buahom, P.; Zhai, S.; Li, G.; Park, C. B. Advanced Bimodal Polystyrene/Multi-Walled Carbon Nanotube Nanocomposite Foams for Thermal Insulation. *Carbon* 2017,120, 1–10.

[3] Wang, G.; Wang, C.; Zhao, J.; Wang, G.; Park, C. B.; Zhao, G. Modelling of Thermal Transport through a Nanocellular Polymer Foam: Toward the Generation of a New Superinsulating Material. *Nanoscale* 2017, 9, 5996–6009.

[4] Wang, G.; Zhao, J.; Wang, G.; Mark, L. H.; Park, C. B.; Zhao, G. Low-Density and Structure-Tunable Microcellular PMMA Foams with Improved Thermal-Insulation and Compressive Mechanical Properties. *Eur. Polym. J.* 2017, 95, 382–393.

[5] Wang, G.; Zhao, G.; Dong, G.; Mu, Y.; Park, C. B.; Wang, G. Lightweight, Super-Elastic, and Thermal-Sound Insulation Bio-Based PEBA Foams Fabricated by High-Pressure Foam Injection Molding with Mold-Opening. *Eur. Polym. J.* 2018, 103, 68–79.

[6] Oliviero, M.; Verdolotti, L.; Stanzione, M.; Lavorgna, M.; Iannace, S.; Tarello, M.; Sorrentino, A. Bio-Based Flexible Polyurethane Foams Derived from Succinic Polyol: Mechanical and Acoustic Performances. *J. Appl. Polym. Sci.* 2017, 134, 45113.

[7] Jahani, D.; Ameli, A.; Saniei, M.; Ding, W.; Park, C. B.; Naguib, H. E. Characterization of the Structure, Acoustic Property, Thermal Conductivity, and Mechanical Property of Highly Expanded Open-Cell Polycarbonate Foams. *Macromol. Mater. Eng.* 2015, 300, 48–56.

[8] Zhao, J.; Wang, G.; Chen, Z.; Huang, Y.; Wang, C.; Zhang, A.; Park, C. B. Microcellular Injection Molded Outstanding Oleophilic and Sound-Insulating PP/PTFE Nanocomposite Foam. *Compos. B. Eng.* 2021, 215, 108786.

[9] Miller, D.; Kumar, V. Microcellular and Nanocellular Solid-State Polyetherimide (PEI) Foams Using Sub-Critical Carbon Dioxide II. Tensile and Impact Properties. *Polymer* 2011, 52, 2910–2919.

[10] Sun, X.; Kharbas, H.; Peng, J.; Turng, L. S. A Novel Method of Producing Lightweight Microcellular Injection Molded Parts with Improved Ductility and Toughness. *Polymer* 2015, 56, 102–110.

[11] Bao, J.-B.; Nyantakyi Junior, A.; Weng, G.-S.; Wang, J.; Fang, Y.-W.; Hu, G.-H. Tensile and Impact Properties of Microcellular Isotactic Polypropylene (PP) Foams Obtained by Supercritical Carbon Dioxide. *J. Supercrit. Fluids* 2016, 111, 63–73.

[12] Tomin, M.; Kmetty, Á. Polymer Foams as Advanced Energy Absorbing Materials for Sports Applications—a Review. *J. Appl. Polym. Sci.* 2021, 139, 51714.

[13] Miltz, J.; Ramon, O. Energy Absorption Characteristics of Polymeric Foams Used as Cushioning Materials. *Polym. Eng. Sci.* 1990, 30, 129–133.

[14] Jin, F.-L.; Zhao, M.; Park, M.; Park, S.-J. Recent Trends of Foaming in Polymer Processing: A Review. *Polymers* 2019, 11, 953.

[15] Xu, J. Y. *Microcellular Injection Molding*; John Wiley &Sons Ltd.: New Jersey, 2010.

[16] Klempner, D.; Sendijarevic, V. *Handbook of Polymeric Foams and Foam Technology*;

Hanser: Munich, 2004.

[17] Zhai, W.; Jiang, J.; Park, C. B. A Review on Physical Foaming of Thermoplastic and Vulcanized Elastomers. *Polym. Rev.* 2021, 62, 95–141.

[18] Colton, J. S.; Suh, N. P. The Nucleation of Microcellular Thermoplastic Foam with Additives: Part I: Theoretical Considerations. *Polym. Eng. Sci.* 1987, 27, 485–492.

[19] Colton, J. S.; Suh, N. P. Nucleation of Microcellular Foam: Theory and Practice. *Polym. Eng. Sci.* 1987, 27, 500–503.

[20] Leung, S. N.; Wong, A.; Guo, Q. P.; Park, C. B.; Zong, J. H. Change in the Critical Nucleation Radius and Its Impact on Cell Stability during Polymeric Foaming Processes. *Chem. Eng. Sci.* 2009, 64, 4899–4907.

[21] Wong, A.; Park, C. B. The Effects of Extensional Stresses on the Foamability of Polystyrene–Talc Composites Blown with Carbon Dioxide. *Chem. Eng. Sci.* 2012, 75, 49–62.

[22] Karthika, S.; Radhakrishnan, T. K.; Kalaichelvi, P. A Review of Classical and Nonclassical Nucleation Theories. *Cryst. Growth Des.* 2016, 16 (11), 6663–6681.

[23] Albalak, R. J.; Tadmor, Z.; Talmon, Y. Polymer Melt Devolatilization Mechanisms. *AIChE J.* 1990, 36, 1313–1320.

[24] Yarin, A. L.; Lastochkin, D.; Talmon, Y.; Tadmor, Z. Bubble Nucleation during Devolatilization of Polymer Melts. *AIChE J.* 1999, 45, 2590–2605.

[25] Leung, S. N.; Wong, A.; Wang, L. C.; Park, C. B. Mechanism of Extensional Stress-Induced Cell Formation in Polymeric Foaming Processes with the Presence of Nucleating Agents. *J. Supercrit. Fluids* 2012, 63, 187–198.

[26] Wong, A.; Chu, R. K. M.; Leung, S. N.; Park, C. B.; Zong, J. H. A Batch Foaming Visualization System with Extensional Stress-Inducing Ability. *Chem. Eng. Sci.* 2011, 66, 55–63.

[27] Wong, A.; Guo, Y. T.; Park, C. B. Fundamental Mechanisms of Cell Nucleation in Polypropylene Foaming with Supercritical Carbon Dioxide—Effects of Extensional Stresses and Crystals. *J. Supercrit. Fluids* 2013, 79, 142–151.

[28] Wong, A.; Wijnands, S. F. L.; Kuboki, T.; Park, C. B. Mechanisms of Nanoclay-Enhanced Plastic Foaming Processes: Effects of Nanoclay Intercalation and Exfoliation. *J. Nanopart. Res.* 2013, 15, 1815.

[29] Reglero Ruiz, J. A.; Vincent, M.; Agassant, J.-F.; Claverie, A.; Huck, S. Morphological Analysis of Microcellular PP Produced in a Core-Back Injection Process Using Chemical Blowing Agents and Gas Counter Pressure. *Polym. Eng. Sci.* 2015, 55, 2465–2473.

[30] Reglero Ruiz, J. A.; Vincent, M.; Agassant, J.-F.; Sadik, T.; Pillon, C.; Carrot, C. Polymer Foaming with Chemical Blowing Agents: Experiment and Modeling. *Polym. Eng. Sci.* 2015, 55, 2018–2029.

[31] Coste, G.; Negrell, C.; Caillol, S. From Gas Release to Foam Synthesis, the Second Breath of Blowing Agents. *Eur. Polym. J.* 2020, 140, 110029.

[32] Zhou, Y.-G.; Su, B.; Turng, L.-S. Fabrication of Super-Ductile PP/LDPE Blended Parts with a Chemical Blowing Agent. *J. Appl. Polym. Sci.* 2016, 133, 44101.

[33] Eaves, D. *Handbook of Polymer Foams*; Rapra Technol. Ltd.: Shropshire, 2004.

[34] Tomasko, D. L.; Burley, A.; Feng, L.; Yeh, S.-K.; Miyazono, K.; Nirmal-Kumar, S.; Kusaka, I.; Koelling, K. Development of CO_2 for Polymer Foam Applications. *J. Supercrit. Fluids* 2009, 47, 493–499.

[35] Sauceau, M.; Fages, J.; Common, A.; Nikitine, C.; Rodier, E. New Challenges in Polymer Foaming: A Review of Extrusion Processes Assisted by Supercritical Carbon Dioxide. *Prog. Polym. Sci.* 2011, 36, 749–766.

[36] Raps, D.; Hossieny, N.; Park, C. B.; Altstädt, V. Past and Present Developments in Polymer Bead Foams and Bead Foaming Technology. *Polymer* 2015, 56, 5–19.

[37] Doroudiani, S.; Park, C. B.; Kortschot, M. T. Effect of the Crystallinity and Morphology on the Microcellular Foam Structure of Semicrystalline Polymers. *Polym. Eng. Sci.* 1996, 36, 2645–2662.

[38] Sánchez-Calderón, I.; Bernardo, V.; Martín-de-León, J.; Rodríguez-Pérez, M. Á. Novel Approach Based on Autoclave Bead Foaming to Produce Expanded Polycarbonate (EPC) Bead Foams with Microcellular Structure and Controlled Crystallinity. *Mater. Des.* 2021, 212, 110200.

[39] Banerjee, R.; Ray, S. S. Foamability and Special Applications of Microcellular Thermoplastic Polymers: A Review on Recent Advances and Future Direction. *Macromol. Mater. Eng.* 2020, 305, 2000366.

[40] Lee, S.-T.; Park, C. B.; Ramesh, N. S. *Polymeric Foams: Science and Technology*; CRC

Press: Boca Raton, 2006.

[41] Okolieocha, C.; Raps, D.; Subramaniam, K.; Altstädt, V. Microcellular to Nanocellular Polymer Foams: Progress (2004–2015) and Future Directions – a Review. *Eur. Polym. J.* 2015, 73, 500–519.

[42] Wang, L.; Hikima, Y.; Ishihara, S.; Ohshima, M. Fabrication of High Expansion Microcellular Injection-Molded Polypropylene Foams by Adding Long-Chain Branches. *Ind. Eng. Chem. Res*. 2016, 55, 11970–11982.

[43] Wang, L.; Hikima, Y.; Ohshima, M.; Yusa, A.; Yamamoto, S.; Goto, H. Unusual Fabrication of Lightweight Injection-Molded Polypropylene Foams by Using Air as the Novel Foaming Agent. *Ind. Eng. Chem. Res.* 2018, 57, 3800–3804.

[44] Yin, D.; Mi, J.; Zhou, H.; Wang, X.; Fu, H. Microcellular Foaming Behaviors of Chain Extended Poly(Butylene Succinate)/Polyhedral Oligomeric Silsesquioxane Composite Induced by Isothermal Crystallization. *Polym. Degrad. Stab.* 2019, 167, 228–240.

[45] Rachtanapun, P.; Selke, S. E. M.; Matuana, L. M. Relationship between Cell Morphology and Impact Strength of Microcellular Foamed High-Density Polyethylene/Polypropylene Blends. *Polym. Eng. Sci.* 2004, 44, 1551–1560.

[46] Bai, T.; Dong, B.; Xiao, M.; Liu, H.; Wang, N.; Wang, Y.; Wang, C.; Liu, C.; Cao, W.; Zhang, J.; Ma, Y.; Guo, Z. Polystyrene Foam with High Cell Density and Small Cell Size by Compression-Injection Molding and Core Back Foaming Technique: Evolution of Cells in Cavity. *Macromol. Mater. Eng.* 2018, 303, 1800110.

[47] Zhao, J.; Wang, G.; Zhang, L.; Li, B.; Wang, C.; Zhao, G.; Park, C. B. Lightweight and Strong Fibrillary PTFE Reinforced Polypropylene Composite Foams Fabricated by Foam Injection Molding. *Eur. Polym. J.* 2019, 119, 22–31.

[48] Taki, K.; Kitano, D.; Ohshima, M. Effect of Growing Crystalline Phase on Bubble Nucleation in Poly(L-Lactide)/CO_2 Batch Foaming. *Ind. Eng. Chem. Res.* 2011, 50, 3247–3252.

[49] Hou, J.; Zhao, G.; Wang, G. Polypropylene/talc Foams with High Weight-Reduction and Improved Surface Quality Fabricated by Mold-Opening Microcellular Injection Molding. *J. Mater. Sci. Technol.* 2021, 12, 74–86.

[50] Zhai, W.; Kuboki, T.; Wang, L.; Park, C. B.; Lee, E. K.; Naguib, H. E. Cell Structure Evolution and the Crystallization Behavior of Polypropylene/Clay Nanocomposites Foams Blown in Continuous Extrusion. *Ind. Eng. Chem. Res.* 2010, 49, 9834–9845.

[51] Yang, C.; Wang, G.; Zhao, J.; Zhao, G.; Zhang, A. Lightweight and Strong Glass Fiber Reinforced Polypropylene Composite Foams Achieved by Mold-Opening Microcellular Injection Molding. *J. Mater. Sci. Technol.* 2021, 14, 2920–2931.

[52] Zhao, J.; Wang, G.; Zhu, W.; Zhou, H.; Weng, Y.; Zhang, A.; Dong, G.; Zhao, G. Lightweight and Strong Polypropylene/Talc/Polytetrafluoroethylene Foams with Enhanced Flame-Retardant Performance Fabricated by Microcellular Foam Injection Foaming. *Mater. Des.* 2022, 215, 110539.

[53] Miyamoto, R.; Yasuhara, S.; Shikuma, H.; Ohshima, M. Preparation of Micro/Nanocellular Polypropylene Foam with Crystal Nucleating Agents. *Polym. Eng. Sci.* 2014, 54, 2075–2085.

[54] Wang, L.; Wan, D.; Qiu, J.; Tang, T. Effects of Long Chain Branches on the Crystallization and Foaming Behaviors of Polypropylene-g-Poly(Ethylene-Co-1-Butene) Graft Copolymers with Well-Defined Molecular Structures. *Polymer* 2012, 53, 4737–4757.

[55] Embabi, M.; Kweon, M. S.; Wang, Y. X.; Lin, T.-P.; López-Barrón, C. R.; Lee, P. C. Foaming Performance of Linear Polypropylene Ionomers. *Macromolecules* 2022, 55, 5645–5655.

[56] Krause, B.; Mettinkhof, R.; van der Vegt, N. F. A.; Wessling, M. Microcellular Foaming of Amorphous High-TgPolymers Using Carbon Dioxide. *Macromolecules* 2001, 34 (4), 874–884.

[57] Qu, Z.; Mi, J.; Jiao, Y.; Zhou, H.; Wang, X. Microcellular Morphology Evolution of Polystyrene/Thermoplastic Polyurethane Blends in the Presence of Supercritical CO_2. *Cell. Polym.* 2019, 38, 68–85.

[58] Sharudin, R. W.; Nabil, A.; Taki, K.; Ohshima, M. Polypropylene-Dispersed Domain as Potential Nucleating Agent in PS and PMMA Solid-State Foaming. *J. Appl. Polym. Sci.* 2010, 119, 1042–1051.

[59] Zhao, J.; Wang, G.; Zhu, W.; Xu, Z.; Zhang, A.; Dong, G.; Zhao, G. Ultra-Light, Super-Insulating, and Strong Polystyrene/Carbon Nanofiber Nanocomposite Foams Fabricated by Microcellular Foaming. *Eur. Polym. J.* 2022, 173, 111261.

[60] Gong, P.; Wang, G.; Tran, M.-P.; Buahom, P.; Zhai, S.; Li, G.; Park, C. B. Advanced Bimodal Polystyrene/Multi-Walled Carbon Nanotube Nanocomposite Foams for Thermal Insulation. *Carbon* 2017, 120, 1–10.

[61] Zhang, H.-B.; Yan, Q.; Zheng, W.-G.; He, Z.; Yu, Z.-Z. Tough Graphene−Polymer Microcellular Foams for Electromagnetic Interference Shielding. *ACS Appl. Mater. Interfaces* 2011, 3, 918–924.

[62] Shen, B.; Zhai, W.; Lu, D.; Zheng, W.; Yan, Q. Fabrication of Microcellular Polymer/Graphene Nanocomposite Foams. *Polym. Int.* 2012, 61, 1693–1702.

[63] Yeh, S.-K.; Huang, C.-H.; Su, C.-C.; Cheng, K.-C.; Chuang, T.-H.; Guo, W.-J.; Wang, S.-F. Effect of Dispersion Method and Process Variables on the Properties of Supercritical CO_2 Foamed Polystyrene/Graphite Nanocomposite Foam. *Polym. Eng. Sci.* 2013, 53, 2061–2072.

[64] Okolieocha, C.; Beckert, F.; Herling, M.; Breu, J.; Mülhaupt, R.; Altstädt, V. Preparation of Microcellular Low-Density PMMA Nanocomposite Foams: Influence of Different Fillers on the Mechanical, Rheological and Cell Morphological Properties. *Compos. Sci. Technol.* 2015, 118, 108–116.

[65] Zhang, X. H.; Zhai, W. T. Coloured TPU Foam Material, Preparation Method and Use Thereof, as well as Method for Preparing Shaped Body, Sheet and Shoe Material by Using Same. US10035894B2,2016.

[66] Jiang, R.; Yao, S.; Chen, Y. C.; Liu, T.; Xu, Z. M.; Park, C. B.; Zhao, L. Effect of Chain Topological Structure on the Crystallization, Rheological Behavior and Foamability of TPEE Using Supercritical CO_2 as a Blowing Agent. *J. Supercrit. Fluids* 2019,147,48–58.

[67] Barzegari, M. R.; Hossieny, N.; Jahani, D.; Park, C. B. Characterization of Hard-Segment Crystalline Phase of Poly(Ether-Block-Amide) (PEBAXVR) Thermoplastic Elastomers in the Presence of Supercritical CO_2 and Its Impact on Foams. *Polymer* 2017,114,15–27.

[68] Hossieny, N. J.; Barzegari, M. R.; Nofar, M.; Mahmood, S. H.; Park, C. B. Crystallization of Hard Segment Domains with the Presence of Butane for Microcellular Thermoplastic Polyurethane Foams. Polymer 2014, 55, 651–662.

[69] Drobny, J. G. *Handbook of Thermoplastic Elastomers*, William Andrew Inc.: New York, 2007.

[70] Koshimura, K.; Sato, H. Application Study of Styrene-Isobutylene-Styrene Block Copolymer as a New Thermoplastic Elastomer. *Polym. Bull.* 1992, 29, 705–711.

[71] Yoshihashi, K. Industrial Synthetic Method of the Rubbers 11. Living Radical (Carbocationic) Block-Copolymer. *NIPPON GOMU KYOKAISHI* 2016, 89, 129−133.

[72] Nakabayashi, H. Properties and Applications of Polyisobutylene-based Thermo Plastic Elastomer. *NIPPON GOMU KYOKAISHI* 2010, 83, 284−288.

[73] Fittipaldi, M.; Rodriguez, L. A.; Grace, L. R. The Effect of Water Absorption on the Viscoelastic Properties of Poly(Styrene-Block-Isobutylene-Block-Styrene) for Use in Biomedical Applications. *AIP Conf. Proc.* 2015, 1664, 030003-1–030003-5.

Chapter 2 Microcellular Foam of Styrene-Isobutylene-Styrene Copolymer (SIBS) with N_2 Using Polypropylene as a Crystallization Nucleating and Shrinkage Reducing Agent

2.1 Introduction

As mentioned in the Dissertation Overview in Chapter 1, limited foamability of thermoplastic elastomer (TPEs) by foam injection molding is an issue that retrain the performance and application of foam products.

TPEs, including TPU, are block copolymers of an alternating sequence of hard and soft segments. The hard segment can be employed as a physical crosslink site to form a three-dimensional network, and soft segment endows high flexibility. This structure gives TPE an outstanding elastic behavior[1-3] and pronounced processability because of its reversible elasticity with heat.[3] Foaming is a promising method to expand the application of TPE. TPE foams have been used in various fields such as sportswear, automobile parts, packing materials, and medical equipment.[4-5] Chemical foaming has been a central technique for elastomeric foams[6] However, from the viewpoint of environmental issues, the foaming technique with green physical blowing agents (PBA) such as CO_2 and N_2 and without chemical crosslinking agents will play an essential role in increasing the recyclability of foams.[7] Based on this view, there have been many studies on the physical foaming processes of TPE and TPU foams. Nofar and his coworkers investigated the effect of hard and soft segment contents on the batch foaming behaviors of TPU.[8-9] They reported that heterogeneous cell nucleation was improved when the hard segment content was higher. The hard segment formed crystal parts and played the role of cell nucleation sites. The high content of the hard segment also broadened the processing window and hindered the shrinkage of the foams. When the molecular weight of the soft segment increased, the expansion ratio increased, while the hard segment controlled the shrinkage. Ge et al. showed that the expansion ratio could be increased by batch foaming with a lower hard segment content, and the crystalline region made from the hard segment could increase the cell density.[10] Ghariniyat and Leung developed a novel TPU-

hexagonal boron nitride composite foam with an improved thermal conductivity using a batch foaming method. They demonstrated that the formation of a thermally conductive filler network in foams could be promoted by the synergy of the post-foaming elastic recovery and foam-induced filler alignment.[11] Shabani and coworkers conducted batch foaming, foam extrusion, and bead foam of TPU and compared the cell structures of the resulting foams. Their results show that the foams produced by batch foaming had a higher cell density and a smaller cell size than foam extrusion and bead foaming.[12] Qu and his coworkers investigated batch foaming of a blend of polystyrene (PS) and TPU. They reported that the solubility of CO_2 and the rheological properties were enhanced by blending PS with TPU, and a bimodal cellular structure was formed by blending TPU with PS as a dispersed domain.[13] Wang and his coworkers studied the effect of elastic strain energy on the TPU cell nucleation and found that both stretching and compression could facilitate cell nucleation where stretching was much more efficacious.[14] As reviewed, most of the research on TPE or TPU physical foaming was conducted by batch foaming or bead foaming methods, where the presence of hard and soft segments can be used effectively to control the cell structure.

It has been stated previously in Section 1.3 of Chapter 1, the merits of foam injection molding technique for foaming thermoplastic polymers in general involve the short cycle time, less material usage, and higher dimensional stability of the foams.[7,15,16,17] However, the traditional foam injection molding (FIM) with short-shot and full-shot methods have several issues. For example, cell nucleation and cell growth are restricted, especially in the short-shot method. The expansion ratio and weight reduction are low (usually less than 30%), which hinders the applications of injection-molded foam products. Furthermore, the high melt temperature and strong shear flow during the injection stage deteriorate the cell structure, so foam products may suffer poor functionality.[7,18-19] To overcome these shortcomings, the core-back foam injection molding technique or precise mold opening technique has been applied to thermoplastic polymers. The technique significantly improves the cellular structure and mechanical properties, and it can fabricate high-expansion foams. Wang prepared a lightweight polyether block amide (PEBA) foam with excellent elasticity and thermal-sound insulation properties using core-back foam injection molding technology.[20] Ellingham et al. extended core-back foam injection molding to a three-stage microcellular injection molding technique. They produced lightweight TPU foams with various densities, cell structures, and mechanical properties.[21]

Poly(styrene-block-isobutylene-block-styrene) (SIBS) is a kind of amorphous TPE composed of a hard styrene segment and a soft isobutylene segment. Compared with other TPEs or TPUs, it is gaining significant attention in biomedical applications because of its high biocompatibility.[22-23] In addition, it exhibits excellent heat aging resistance, superior gas barrier-ability, and damping behavior, so it is promising for many applications.[24] However, it remains difficult to prepare any foams from neat SIBS by melt processing with a uniform fine cell structure. In addition, Elastomer foams are prone to shrinkage even at room temperature due to lower modulus than plastic foams.[7,20] Polymer blending or the addition of a filler is a simple and effective method to improve the physical properties of SIBS.[25-27]

In this chapter, PP was used to improve the cell structure and foamability of SIBS. PP is a semi-crystalline polymer, and its crystallization behavior can possibly play the role of a cell nucleating agent and improve the foamability with CO_2 or N_2, as shown in thermoplastic polymer foaming.[28-29] SIBS/PP with 10%, 20%, and 30% PP contents were blended to form sea-island morphology, where PP "island" can be dispersed in SIBS "sea" as illustrated in Figure 2.1. Besides, it is believed that PP crystals can provide stiffness to SIBS foams, to suppress their shrinkage. Based on these concepts, foams were fabricated by the core-back injection molding technique, and the effects of PP on SIBS foaming and the shrinkage of the foams were investigated. The crystallization rate, rheology, and morphology of SIBS/PP were evaluated to clarify the effects.

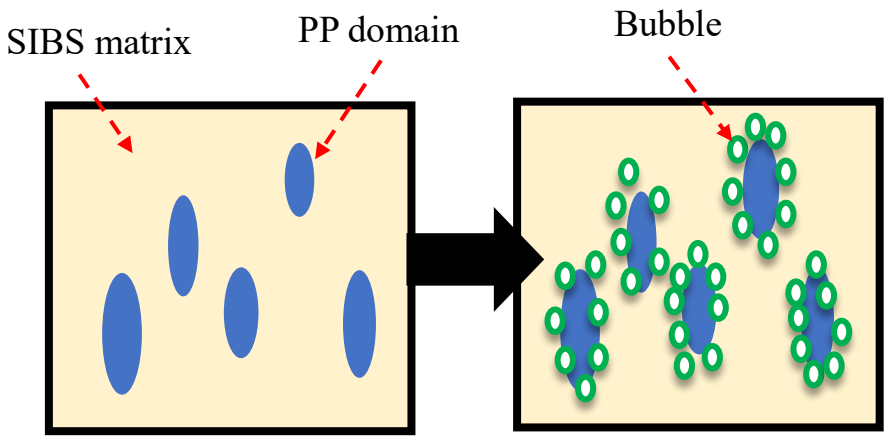

Figure 2.1 Schematic of sea-island morphology in SIBS/PP blends.

2.2 Experimental

2.2.1 Materials

Styrene-isobutylene-styrene block copolymer (SIBS073T, Kaneka, Osaka, Japan) with a 6.0 g/10 min (230 ℃/2.16 kg) melt flow rate was provided and used as is. Polypropylene (Waymax MFX3, Japan Polypropylene Corporation, Tokyo, Japan) with an 8.0 g/10 min (230 ℃/2.16 kg) melt flow rate was used as a viscosity modifier, cell nucleating agent, and shrinkage prohibiting agent. Nitrogen (N_2, Izumi Sanyo, Tokyo, Japan) was utilized as a physical blowing agent (PBA) with a purity over 99%.

2.2.2 Sample Preparation

A 35-ton clamping force MuCell® foam injection molding machine (J35EL III-F, Japan Steel Work, Hiroshima, Japan) and a gas delivery system (SCF device SII TRJ-10-A-MPD, Trexel Inc., USA) were used. N_2 was pressurized to 24 MPa by the gas delivery system and injected into the molten polymer in the barrel of the injection molding machine through an injector valve. The N_2 concentration in the polymer was set at 0.1% by manipulating the valve opening period of the injector valve. Mixing the gas with molten polymer at higher temperatures and pressures with a screw enhances the gas dispersion and dissolution and creates a single-phase N_2/polymer solution. The temperatures of the injection molding machine were set at 150, 180, 200, 200, 200, 200, and 200 °C from the bottom of the hopper (feeding zone) to the shut-off nozzle (nozzle zone). The mold temperature was maintained at 40 °C. The mold has a rectangular cavity with dimensions of 70 mm × 50 mm × 2 mm. The temperature and pressure sensor locations were given in our previous paper.[30] The experimental conditions are summarized in Table 2.1.

Table 2.1 Experimental conditions for the injection molding machine.

Parameters	Values
PP content wt.%	0, 10, 20, 30
Temperature (℃)	150, 180, 200, 200, 200, 200, 200
Mold temperature (℃)	40
Injection speed (mm/s)	100
Screw back pressure (MPa)	15
Dwelling time (s)	7-11.5
Core-back distance (mm)	2
Core-back speed (mm/s)	20
Metering distance (mm)	50
N_2 content (%)	0.1

2.2.3 Thermal Analysis

Fast scanning chip calorimetry (FSC) was conducted using Mettler-Toledo Flash DSC1 (Mettler-Toledo, LLC, USA) to observe the non-isothermal crystallization behavior of PP in the blend polymers. Thin films of SIBS and SIBS/PP blends 10−20 μm in thickness were prepared by hot compression at a temperature of 200 ℃ under 30 MPa mechanical pressure. A small piece specimen was cut out from the thin films and used for measurement. Figure 2.2a shows a temperature profile of the polymer injected into the mold cavity. The temperature profile was divided into several time zones, and a constant cooling rate was assumed in each zone. The temperature change of Flash DSC was programmed as shown in Figure 2.2b by simulating the cooling temperature profile: the temperature was first increased to 200 ℃ at 1000 ℃/s. Then, it was decreased at the constant cooling rates associated with the cooling rate of the time zones. Immediately after reaching the end temperature of the designated number of zones, the temperature was rapidly increased to 200 ℃ at 1000 ℃/s, and the heating curve was obtained. The procedure was repeated by extending the number of zones one by one in the FSC cooling process. The onset of crystallization in the cooling process shown in Figure 2.2a was estimated from the heating curve, where a melting peak first appeared.

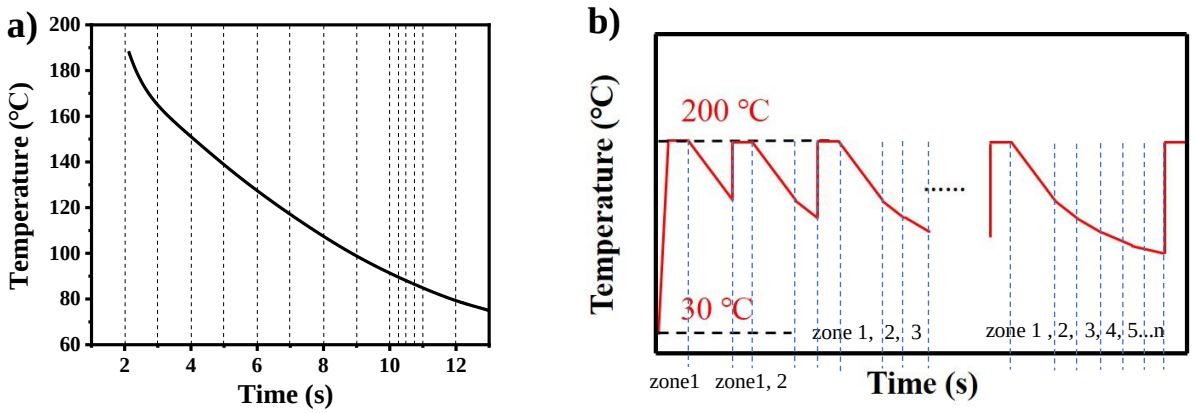

Figure 2.2 a) A temperature profile of the cooling process in the mold cavity; b) the specific FDSC program of the discrete method for determining the onset and the maximum crystallization rate temperatures during the rapid cooling process.

2.2.4 Rheological Characterization

Strain-controlled frequency sweep and temperature ramp sweep measurements were conducted using an ARES rheometer with a 25-mm parallel-plate device. The specimens were prepared 25 mm in diameter and 2 mm in thickness using a hot compressing machine at a temperature of 200 ℃ and compression pressure of 10 MPa. Frequency sweep measurements were conducted in the frequency range of 0.1-100 rad/s with a 1% strain amplitude at 200 ℃. Temperature sweep measurements were conducted in the range of 100–200 ℃ with a 1% strain amplitude and 0.63 rad/s. The damping rate was 2 ℃/min.

2.2.5 Blend Morphology Observation

The blend morphology of SIBS/PP was observed by a scanning electron microscope (FE-SE) (JSM-6340F, JEOL Ltd., Tokyo, Japan). All specimens were cut out from the middle parts of the nonfoamed injection-molded products after cryogenically fracturing in liquid nitrogen. Prior to the SEM observation, RuO_4 was used to differentiate the SIBS matrix and PP domains.[31-33] Then, after three hours of staining, the stained sample was dried in vacuo for at least 6 hours.

2.2.6 Cell Structure Characterization

The cell structure of the foams was evaluated by the cell size and cell density. The cell structure was investigated using a scanning electron microscope (Tiny-SEM Mighty-8, Technex,

Tokyo, Japan). A small slice specimen was cut from the center of the injection-molded product and cryogenically fractured in liquid nitrogen. The fractured surface was gold-coated using a quick coater (VPS-020, ULVAC KIKO, Ltd., Japan). Then, SEM images were analyzed using ImageJ (National Institutes of Health, USA). The cell density (N_0) was calculated by Eq. (2-1), and over 200 cell diameters were measured and averaged in Eq. (2-2):[34-35]

$$N_0 = \left(\frac{n}{A}\right)^{\frac{3}{2}} \qquad (2\text{-}1)$$

where n is the number of cells chosen in the designated SEM image area, and A is the selected area in the image. The average cell diameter can be obtained by Eq. (2-2):[4,5]

$$d = \frac{\Sigma d_i n_i}{\Sigma n_i} \qquad (2\text{-}2)$$

where n_i is the number of bubbles (pores) with diameter d_i, assuming that the bubble is spherical.

2.2.7 Shrinkage Evaluation

The foam shrinkage ratio was calculated from the foam density. The foam density was measured by an electronic densimeter (MDS-300, Alfa Mirage Co., Ltd, Japan) every day after the foam injection molding for 35 days. Then, the shrinkage ratio was given by Eq (2-3):

$$Shrinkage\ Ratio = 1 - \frac{\rho_{foam\_1}}{\rho_{foam\_n}} \qquad (2\text{-}3)$$

where ρ_{foam_1} is the foam density immediately after the foam injection molding, and ρ_{foam_n} is the foam density from day 2 ($35 \geq n \geq 2$).

2.2.8 Mechanical Test

The compressive properties of SIBS-based materials were investigated by using a universal testing machine (Autograph AGS-1kN, Shimazu, Japan) with a compression speed of 1 mm/min. The rectangular-shaped specimen was prepared by cutting the middle of injection-molded nonfoamed products. Four specimens were tested and averaged for each condition. The tensile properties of SIBS-based materials were tested with a tensile speed of 60 mm/min. The dumbbell-shaped samples were cut from injection-molded nonfoamed products by SD Level Sample Cutting Machine (SDL-100, Dumbbell Co., Ltd., Japan).

2.3 Results and Conclusions

2.3.1 Rheological Analysis

Figure 2.3 shows the frequency versus storage modulus (G'), complex viscosity ($|\eta^*|$) and loss modulus (G") of neat PP, neat SIBS, and their blends with three different blend ratios. As shown in Figure 2.3a, G' of neat PP exhibited terminal flow behavior in the low-frequency range,[36-37] and G' of SIBS/PP blends decreased with increasing PP content in the entire frequency region, since the SIBS matrix softened with minor PP domains. A plateau was observed in the low-frequency range of neat SIBS and SIBS/PP blends, which is called the pseudo-solid-like behavior. This behavior indicates the existence of a network-like structure.[26] The G' value in the plateau region reflects the level of network formation, and the level decreased when the PP content increased. $|\eta^*|$ of PP reached a Newtonian plateau in the low-frequency region, and all polymers showed shear-thinning behaviors in the high-frequency range, as shown in Figure 2.3b. Figure 2.3c shows G" of these materials. It can be clearly seen that SIBS-based materials had higher G" and reduced slopes against frequency compared with neat PP. As frequency increased, G" increased, with a lower level than corresponding G' in the low-frequency region. This phenomenon indeed shows the feature of viscoelastic solid.

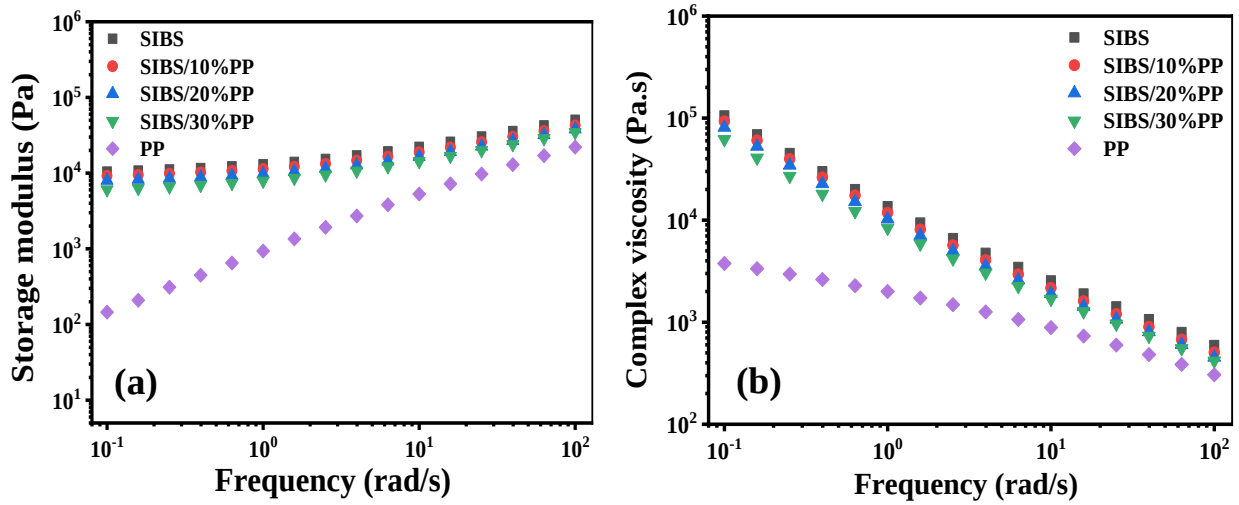

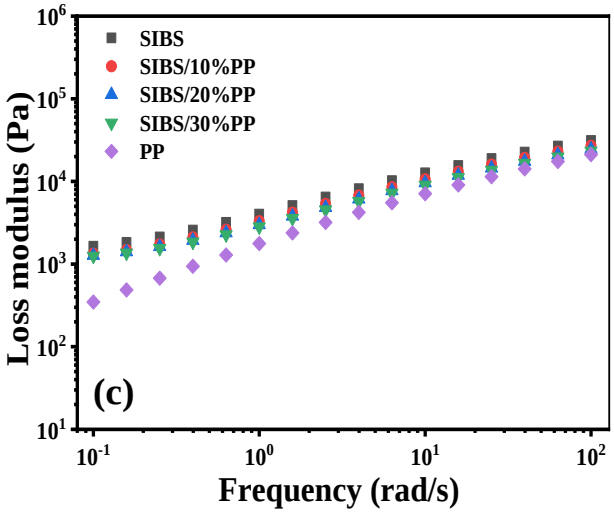

Figure 2.3 Frequency sweep test: (a) storage modulus (G'); (b) complex viscosity ($|\eta^*|$); (c) loss modulus (200 ℃).

Figure 2.4 shows Han's plot of neat PP, neat SIBS, and their blends. As shown in Figure 2.4, neat PP showed a linear relationship between G' and G", while neat SIBS and SIBS/PP blends showed nonlinear correlations. The nonlinear behavior of neat SIBS indicates a microdomain structure of block polymer in neat SIBS, and the nonlinear correlation of blends with different slopes indicates immiscibility and incompatibility between PP and SIBS. It can be speculated that the PS hard segment of SIBS forms the network structure at the experimental temperature (200 ℃). The order-disorder transition temperature of SIBS, where the microdomain structure disappears and becomes a homogenous phase, was reported to be higher than 250 ℃.[38-40]

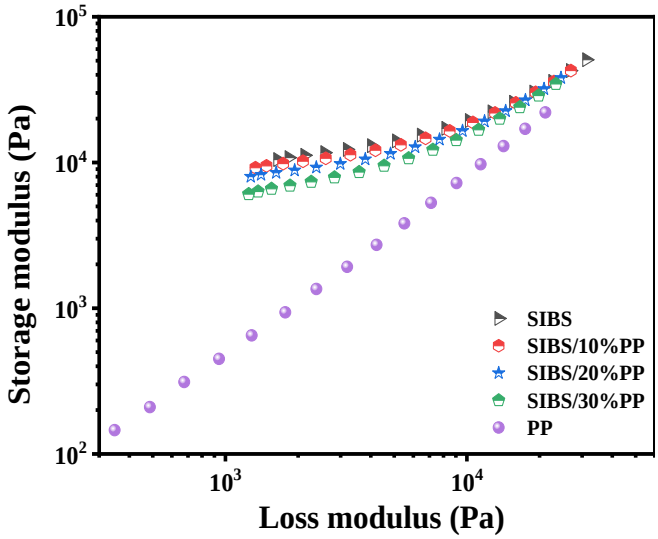

Figure 2.4 G'~ G" Han's plots (200 ℃).

Figure 2.5 shows the temperature dependency of $|\eta^*|$ of neat PP, neat SIBS, and blends. The $|\eta^*|$ values of SIBS and the blends were higher than 10^4 Pa over the entire temperature range, which indicates that a rubber-like behavior exists. It is also clear that changes of $|\eta^*|$ of SIBS and SIBS/10%PP are insensitive to temperature. The $|\eta^*|$ values decreased when the PP content increased; when the PP content exceeded 20 wt.%, a notable viscosity change occurred at a temperature of approximately 135 ℃. The degree of change increased when the PP content increased. These temperature sweep tests demonstrated that crystallization of PP occurred in SIBS/PP blends. Furthermore, the crystallization behavior became prominent when PP content was over 20%, which is attributed to morphology of PP domain in SIBS matrix as signified in Figure 2.6.

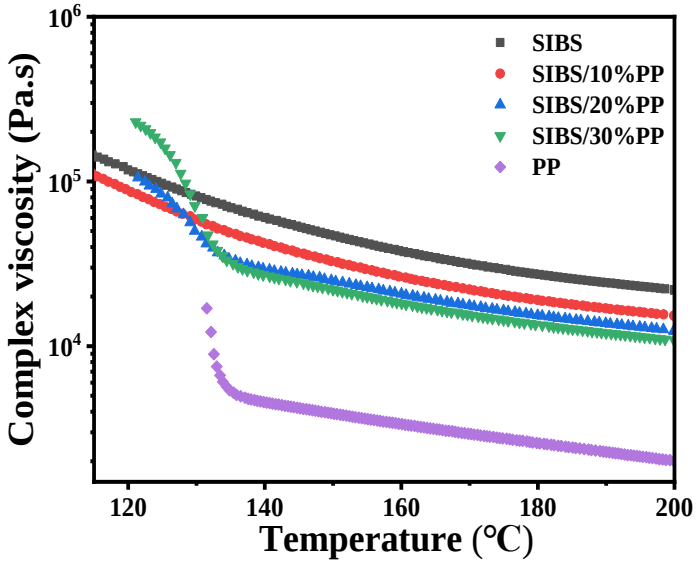

Figure 2.5 Complex viscosity of SIBS-based materials in the range from 115 to 200 °C.

2.3.2 Solid Morphology Observation of SIBS and SIBS/PP Blends

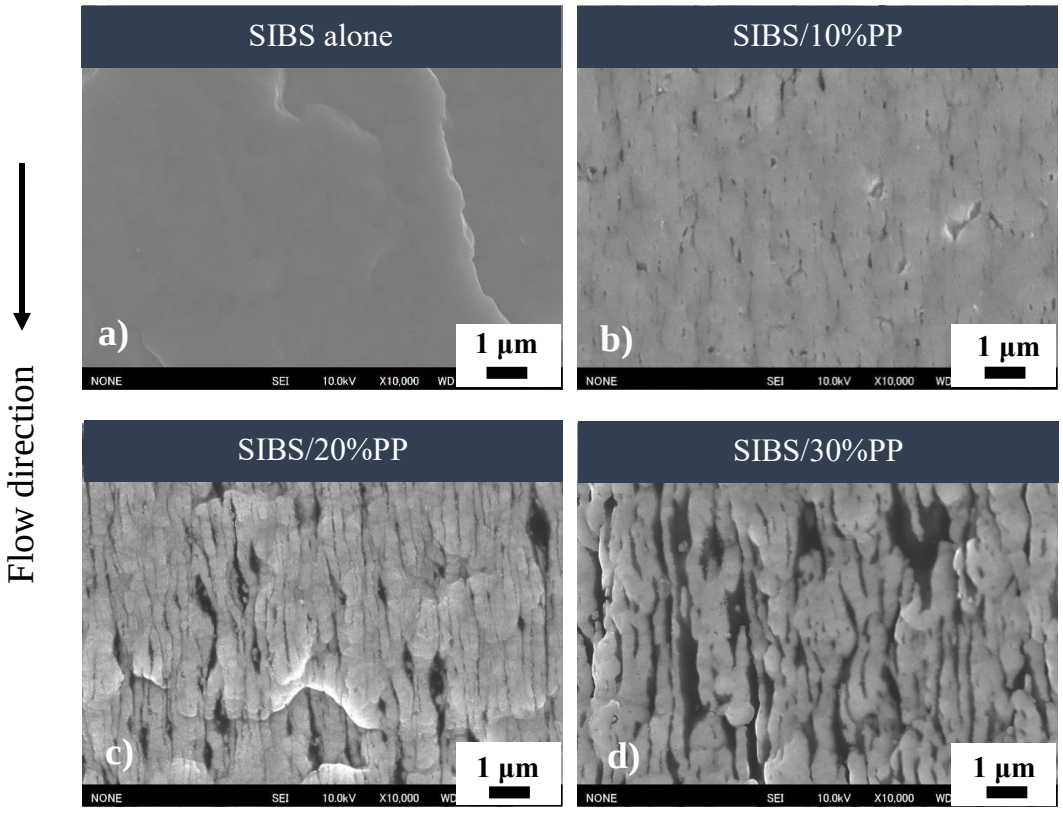

Figure 2.6 SEM images of blend morphology stained with RuO_4: a) SIBS, b) SIBS/10% PP, c) SIBS/20% PP and d) SIBS/30% PP.

Figure 2.6 shows the SEM images of the non-foamed injection-molded SIBS and SIBS/PP blend morphologies. The black domains represent PP, and the grey area is the SIBS matrix. Figure 2.6 illustrates that PP and SIBS were immiscible and incompatible, as the rheological analysis indicated, and the black domains increased with increasing PP content. The fiber-like shaped black domains were observed in the blends, which is attributed to the shear flow induced by injection.

2.3.3 Flash DSC Analysis

The rheological analysis based on temperature sweep tests indicates that the crystallization of PP occurs in SIBS/PP blends. Growing crystals can be used as an effective bubble nucleating agent in the foaming process.[28,41-42] The discrete thermal analysis method using Flash DSC with the temperature program illustrated in Figure 2.2b was helpful to observe that the crystallization of PP occurs in a rapid cooling process of the foam injection molding process. Figures. 2.7a and 2.7b show the heating curves of SIBS/PP (20 wt.%) and SIBS (30 wt.%). Unfortunately, the heat of fusion was too small to be detected in the heating curves of SIBS/PP (10 wt.%). In Figure 2.7, the legend of both figures indicates the temperature at which heating began after a cooling process of Flash DSC, which consisted of the designated number of zones. For SIBS/PP (20 wt.%), a melting peak appeared in the heating curve after the temperature decreased to 95.5 ℃ or lower, while no noticeable peak was observed in the heating curve after cooling until the temperature below 97.9 ℃. Thus, it can be estimated that the crystallization of PP in SIBS/PP (20 wt.%) occurred when the temperature dropped into the range of 95.5-97.9 ℃ during the rapid cooling process. For SIBS/PP (30 wt.%), crystallization occurred when the foaming temperature decreased to 98.4-101.7 ℃ in the rapid cooling process.

Figure 2.8 shows the heat of fusion measured from the heating curves, which clearly indicates the onset of PP crystallization when the temperature decreased to 95-98 ℃ for SIBS/PP (20 wt.%) and 98-100 ℃ for SIBS/PP (30 wt.%). The discrete method results were used to analyze the effect of PP crystals in the blended polymers on the cellular structure. Furthermore, the discrete method shows that the peak of crystallization rate against the temperature was estimated from the ΔH-temperature curves inflection points and was located at approximately 85 ℃ for SIBS/PP (20 wt.%) and 88 ℃ for SIBS/PP (30 wt.%).

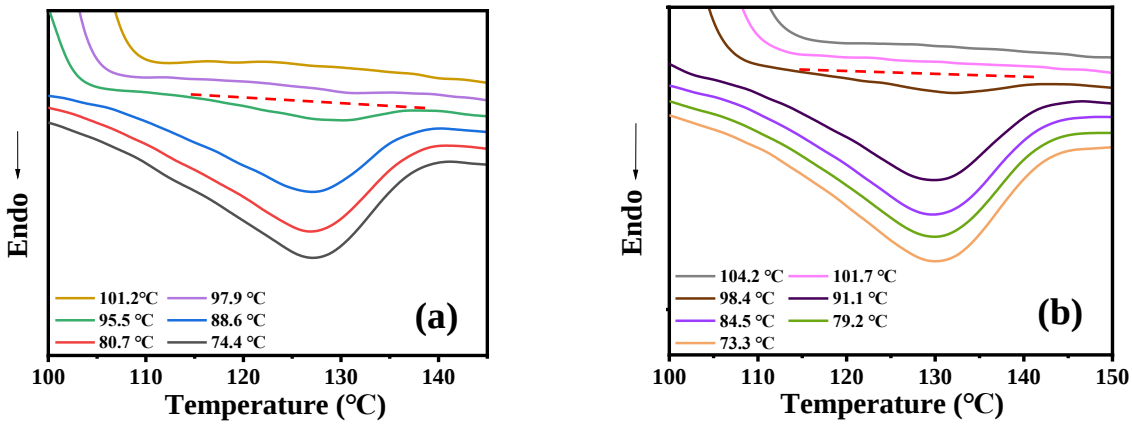

Figure 2.7 Heating curves of SIBS/20%PP (a) and SIBS/30%PP (b) cooled down to the different cooling temperatures along a rapid cooling temperature profile in mold.

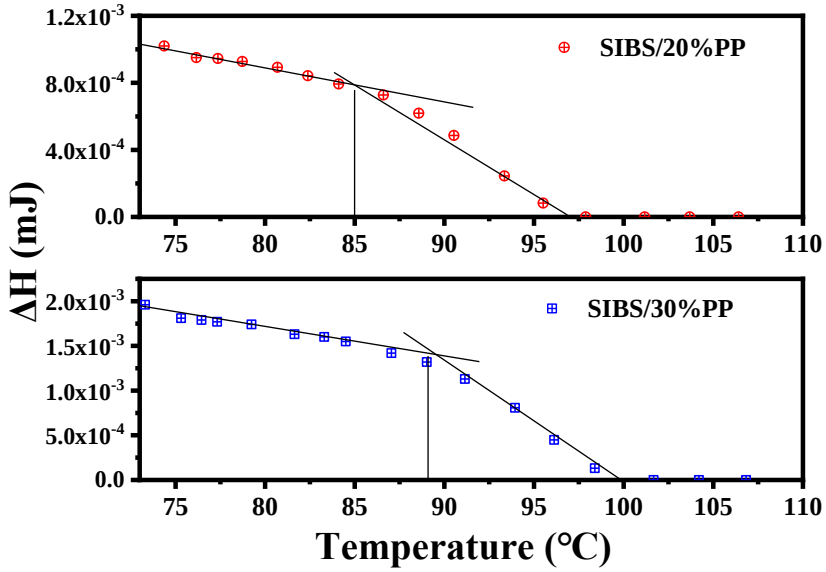

Figure 2.8 Heat of fusion, ΔH, of SIBS/20%PP and 30%PP crystallized by cooling down to the temperature along the cooling temperature profile of Figure 2.2a.

2.3.4 Effects of PP Blending on Cell Structure

Figure 2.9 shows the SEM images of the cell structure of the 2-fold expansion foams prepared at various foaming temperatures. The images were taken from the view perpendicular to the core-back direction. The foaming temperature was the temperature at which the core-back operation commenced. As shown in Figure 2.9, the cell size decreased when the foaming

temperature decreased in both neat SIBS and the blend foams. However, the neat SIBS foams had a few large bubbles together with tiny bubbles even at the lower foaming temperature, while the blend polymer foams showed a relatively uniform microcellular structure with more bubbles. Thus, PP provides bubble nucleation sites and increases the number of bubbles.

It is reported by other researchers that crystalline hard segments can improve foamability of TPU as cell nucleating sites.[8,43] However, in the case of SIBS, the hard segment is non-crystalline glassy PS. In addition, cell nucleating effect of PS was not so effective that poor uniform cellular structure could be observed even at lower foaming temperature (74 ℃), as shown in Figure 2.9. From Table 1.1 in Chapter 1, the composition of SIBS used in this study can be known, where content of PS is 30%. Since the morphology of block copolymer can be changed by adjusting the content of hard and soft segments,[1] it can be speculated that PS domains probably show cylinder structure in a continuous PIB matrix, according to other literatures.[44,45] Different from cell nucleating effect caused by crystallites, cylinder PS domains are amorphous and less closely packed compared with crystallites. The dissolved gas may not be strongly detached from the PS domains even below glass transition temperature of PS, which induces the low degree of supersaturation in the surrounding area of PS domains. Thus, PS has low efficacy as bubble nucleating agent and poor uniform cellular structure is obtained.

Figure 2.10 shows the SEM images of the SIBS/PP (20 and 30 wt.%) foams prepared with foaming temperatures of 94 and 99 ℃ for SIBS/20% PP, and 97 and 100 ℃ for SIBS/30% PP. These images indicate the PP crystallization effect on the cell structure: The cellular structure of blends was changed by decreasing the foaming temperature to below the onset temperature of PP crystallization in the rapid cooling process, as shown in Figures 2.7 and 2.8. At the foaming temperatures higher than 98 ℃, PP was not crystallized when foaming was conducted by a core-back operation. Instead, it provided not only the lower viscosity but also inhomogeneous viscosity domains in the injected polymers and caused the non-uniformity of cell morphology with larger bubbles. At the foaming temperatures below 98 ℃, the PP domains started crystallization and they provided the bubble nucleation sites. As a result, the cell size became smaller and the uniformity of cell morphology increased. However, large cells could be still observed at foaming temperature of 94 and 97 ℃ for SIBS/20% and 30%PP respectively. The formation of these large cells can be mainly attributed to low viscoelasticity at high temperature, and cell nucleation caused by crystallization of large PP domains or long-chain PP. Even though PP crystallization has already

started at 94 ℃ (for SIBS/20%PP) and 97 ℃ (for SIBS/30%PP), chain mobility is not strongly restricted at such high temperatures, which allows large PP domain or long-chain PP to crystallize. The resultant large PP crystals can trigger the nucleation of large cells and reduce the number of nucleated cells, compared with those small PP crystals. Furthermore, the low viscoelasticity of melt at high foaming temperature can cause outward diffusion of blowing agent, resulting in coalescence and collapse of cells and thus increase in cell size[46]. As foaming temperature decreased, the size of PP crystal became small, which can contribute to formation of small cells and uniform cellular structure.

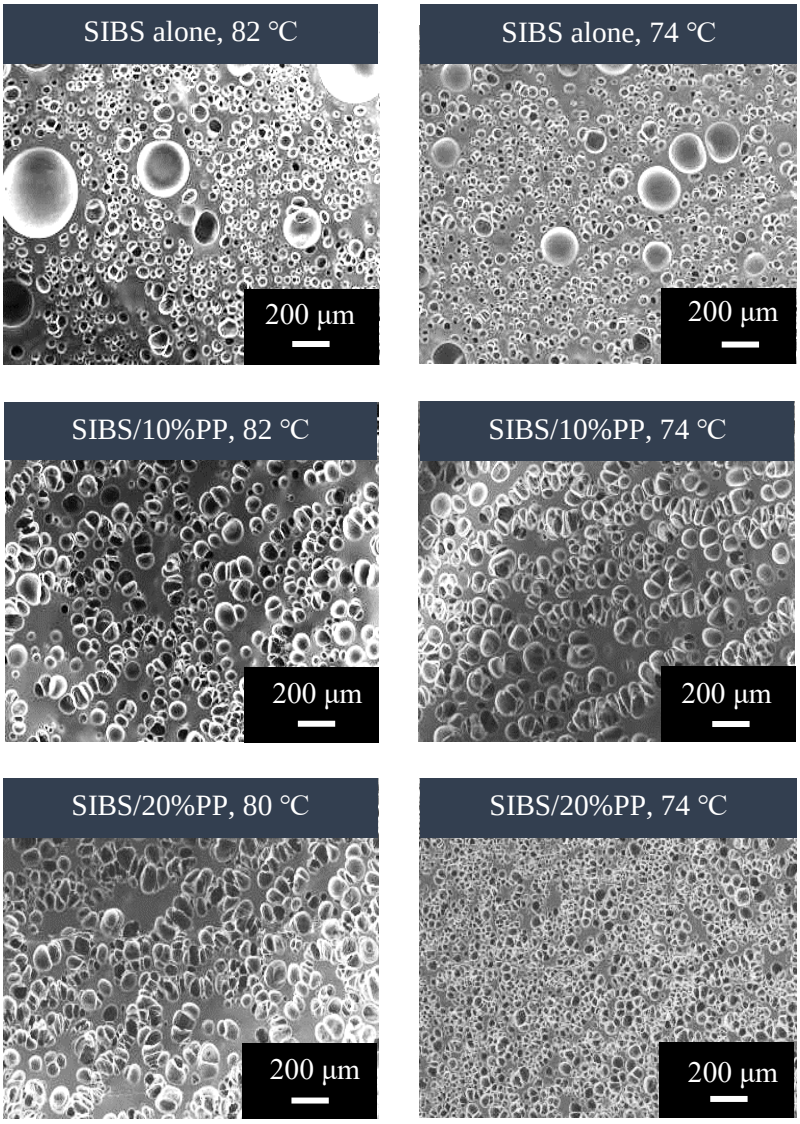

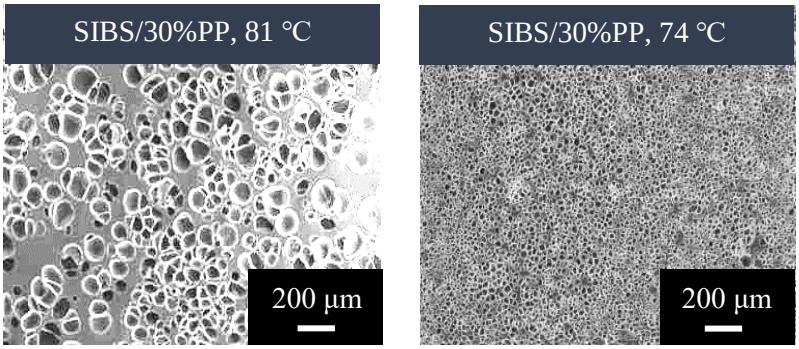

Figure 2.9 SEM images of the cell structure of SIBS and SIBS/PP blend foams prepared at different foaming temperatures.

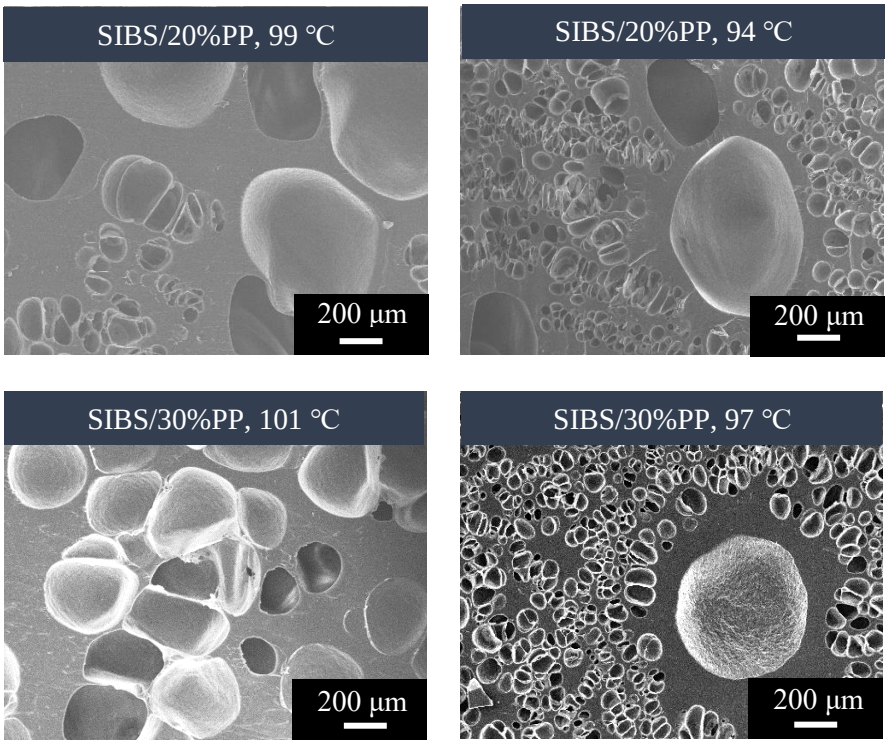

Figure 2.10 SEM images of SIBS/20% and 30%PP at higher foaming temperatures (94 and 99 ℃ for SIBS/20%PP, 97 and 101 ℃ for SIBS/30%PP).

Figure 2.11 shows the cell density and cell diameter estimated from the SEM images of the foams. The cell densities of SIBS/PP blend foams were drastically increased by lowering the foaming temperature. The cell density began to increase at a higher foaming temperature with

increasing PP content in the blend. The degree of increase in cell density also increased with increasing PP content.

Regarding the cell size, the neat SIBS foam shows smaller cell diameters at the entire foaming temperature. Blending PP could not decrease the cell diameter at foaming temperatures above 79 ℃ for SIBS/PP (30 wt.%) and 76 ℃ for SIBS/PP (20 wt.%). The cell diameter of the SIBS/PP (10 wt.%) foam did not decrease compared to that of the neat SIBS foams at all foaming temperatures. The effect of PP on the cell size is attributed to the rheological effect of PP. The viscosity decreased with increasing PP content, as shown in Figure 2.5. When and if the higher viscosity of PP is used for blending, the cell size may decrease with increased PP content in the blend. It is commonly observed in the microcellular foaming when the viscosity increases, the cell size decreases and the cell density increases because the higher viscosity can suppress the bubble growth. However, in the SIBS/PP blends case, the viscosity decreased, and the cell size decreased, but the cell density increased with PP. Figure 2.11 indicates that PP increases bubble nucleation sites to SIBS despite decreasing the viscosity.

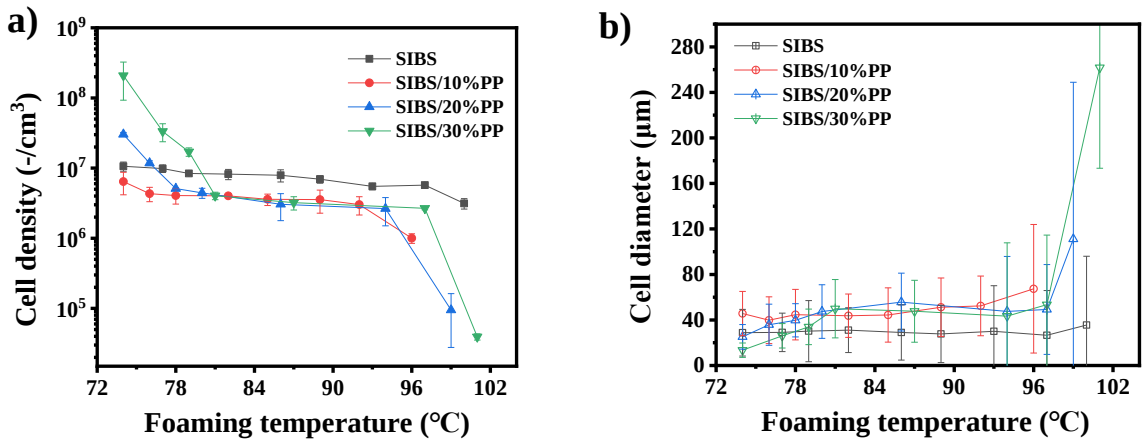

Figure 2.11 Change in cell density and cell diameter of SIBS and SIBS/PP blend foams against foaming temperature.

2.3.5 Shrinkage Evaluation

As described in the introduction, shrinkage is one of the critical issues of TPE and TPU foaming. Shrinkage occurs when the residual blowing agent diffuses out from the foam. Figure 2.12 shows the shrinkage ratio of neat SIBS and SIBS/PP blend foams prepared at 74 ℃ foaming temperature. The shrinkage can be impeded by PP blending. When the PP content increased, the

anti-shrinkage effect of PP became more pronounced. The effect is attributed to the increase in gas permeability of SIBS and increase in modulus due to PP.

Figure 2.13 shows the compression data of SIBS and SIBS/PP blends. SIBS with a higher PP content showed a higher compression modulus. The modulus was enhanced when the PP content increased due to the increase in PP crystallinity. The higher compression modulus acts as a resistance to deformation and shrinkage.[47] Figure 2.14 depicts the tensile test data of SIBS-based materials. It could be clearly seen that high PP content could be beneficial for improvement of elastic modulus. As shown in solid morphology in Figure 2.6, higher modulus of SIBS with higher PP content can be attributed to more oriented PP domains. Due to presence of these oriented PP scaffold, the shrinkage of foam products can be suppressed.

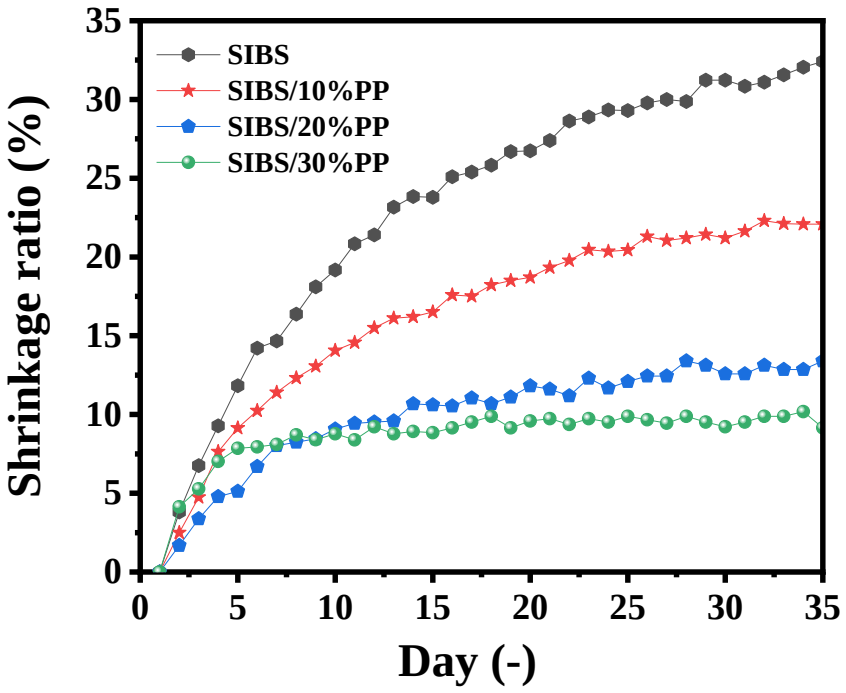

Figure 2.12 Change in shrinkage ratio of the foams with different PP contents throughout the day.

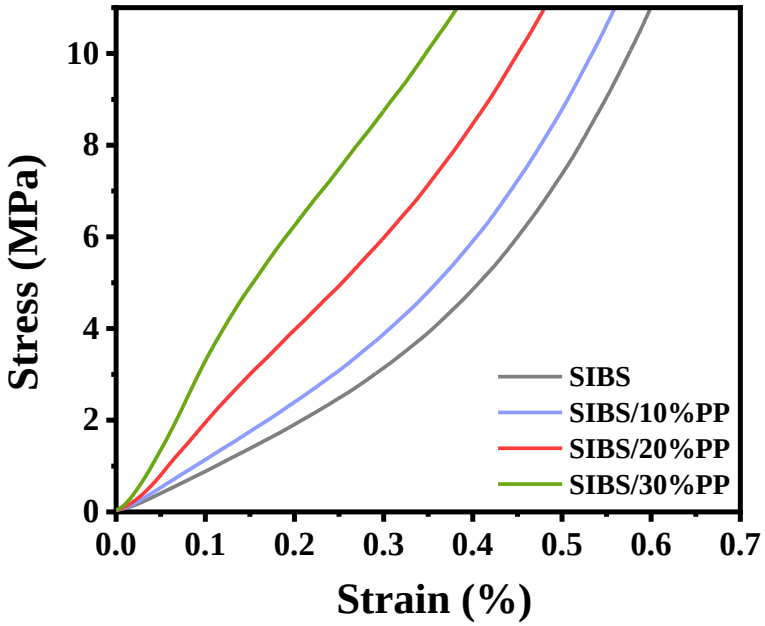

Figure 2.13 Compression vs. strain curve of SIBS and SIBS/PP blends.

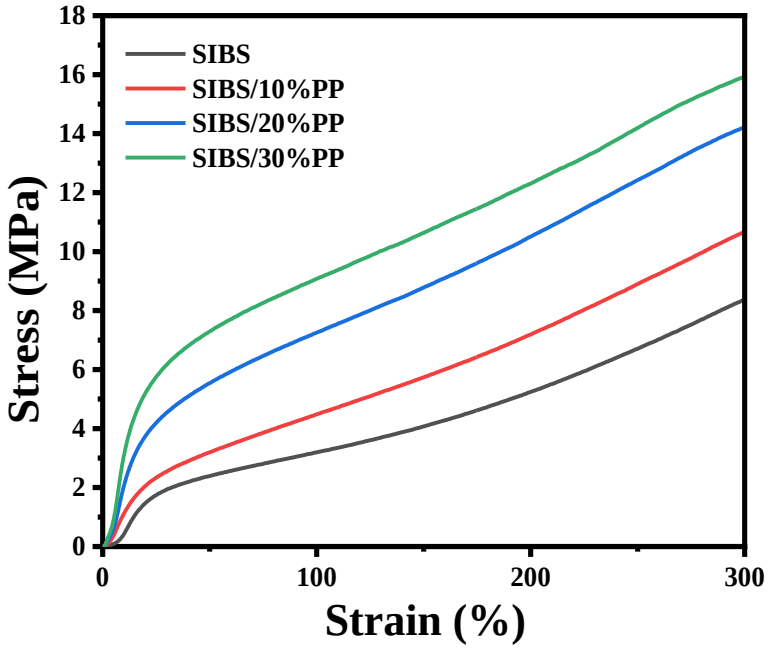

Figure 2.14 Strain-stress curves of tensile test data of SIBS and SIBS/PP blends.

2.4 Conclusion

In this chapter, neat SIBS and SIBS/PP blend foams were prepared by foam injection molding with the core-back operation, and the effect on the cellular structure was investigated. The nucleating effect of PS domains was not so effective that neat SIBS foams showed a relatively poor uniform cellular structure and a higher shrinkage ratio. The possible reason may be that cylinder PS domains are amorphous and less closely packed. The dissolved gas may not be easily released from the PS domains even below glass transition temperature of PS. This phenomenon leads to relatively low gas supersaturation around PS domains, which indicates insignificant cell nucleating effect. Hence, undesirable cellular structures of neat SIBS foams were obtained.

The cell density and anti-shrinkage of the foams were drastically improved by blending PP. PP crystals can provide bubble nucleation sites at a lower foaming temperature than the onset of crystallization temperature in the rapid cooling process of the foam injection molding process. Blending PP restrained the shrinkage of SIBS foam after foaming. The blending of semi-crystalline polymers such as PP offers an effective method to improve the cell structure and anti-shrinkage characteristic of amorphous TPE.

References

[1] Drobny, J. G. *Handbook of Thermoplastic Elastomers*, William Andrew Inc.: New York, 2007.

[2] Shanks, R.; Kong, I. *Thermoplastic Elastomers*; El-Sonbati, A. Z., Ed.; Intech Open: Rijeka, 2012.

[3] Spontak, R. J.; Patel, N. P. Thermoplastic Elastomers: Fundamentals and Applications, *Curr. Opin. Colloid. Interface Sci*. 2000, 5, 334−341.

[4] Kong, H. J.; Lee, S. H.; Kim, D. G.; Kim, H. J.; Park, G. W.; Hyun, K. Investigation of Thermoplastic Elastomer (TPE) Foaming Process Using Blowing Agent by Rheological and Morphological Methods. *J. Appl. Polym. Sci*. 2019, 136, 47358.

[5] Kharbas, H. A.; Ellingham, T.; Manitiu, M.; Scholz, G.; Turng, L.-S. Effect of A Cross-Linking Agent on the Foamability of Microcellular Injection Molded Thermoplastic Polyurethane. *J. Cell. Plast.* 2017, 53, 407–423.

[6] Meng, L.; Liu, H.; Yu, L.; Khalid, S.; Chen, L.; Jiang, T.; Li, Q. Elastomeric Foam Prepared by Supercritical Carbon Dioxide. *J. Appl. Polym. Sci.* 2017, 134, 44354.

[7] Zhai, W.; Jiang, J.; Park, C. B. A Review on Physical Foaming of Thermoplastic and Vulcanized Elastomers. *Polym Rev.* 2022, 62, 95–141.

[8] Nofar, M.; Büşra Küçük, E.; Batı, B. Effect of Hard Segment Content on the Microcellular Foaming Behavior of TPU Using Supercritical CO_2. *J. Supercrit. Fluids* 2019, 153, 104590.

[9] Nofar, M.; Batı, B.; Büşra Küçük, E.; Jalali, A. Effect of Soft Segment Molecular Weight on the Microcellular Foaming Behavior of TPU Using Supercritical CO_2. *J. Supercrit. Fluids.* 2020, 160, 104816.

[10] Ge, C.; Wang, S.; Zheng, W.; Zhai, W. Preparation of Microcellular Thermoplastic Polyurethane (TPU) Foam and Its Tensile Property. *Polym. Eng. Sci.* 2018, 58, E158–E166.

[11] Ghariniyat, P.; Leung, S. N. Development of Thermally Conductive Thermoplastic Polyurethane Composite Foams via CO_2 Foaming-Assisted Filler Networking. *Compos. B. Eng*. 2018, 143, 9−18.

[12] Shabani, A.; Fathi, A.; Erlwein, S.; Altstädt, V. Thermoplastic Polyurethane Foams: From Autoclave Batch Foaming to Bead Foam Extrusion. *J. Cell. Plast.* 2021, 57, 391−411.

[13] Qu, Z.; Mi, J.; Jiao, Y.; Zhou, H.; Wang, X. Microcellular Morphology Evolution of Polystyrene/Thermoplastic Polyurethane Blends in the Presence of Supercritical CO_2. *Cell. Polym.* 2019, 38, 68−85.

[14] Wang, G.; Zhao, J.; Yu, K.; Mark, L. H.; Wang, G.; Gong, P.; Park, C. B.; Zhao, G. Role of Elastic Strain Energy in Cell Nucleation of Polymer Foaming and Its Application for Fabricating Sub-Microcellular TPU Microfilms. *Polymer 2017*, 119, 28–39.

[15] Di Maio, E.; Kiran, E. Foaming of Polymers with Supercritical Fluids and Perspectives on the Current Knowledge Gaps and Challenges. *J. Supercrit. Fluids* 2018, 134, 157–166.

[16] Xu, J. *Microcellular Injection Molding*, John Wiley &Sons Ltd.: New Jersey, 2010.

[17] Gong, S.; Yuan, M.; Chandra, A.; Kharbas, H.; Osorio, A.; Turng, L.-S. Microcellular Injection Molding. *Int. Polym. Proc.* 2005, 20, 202–214.

[18] Yang, C.; Wang, G.; Zhao, J.; Zhao, G.; Zhang, A. Lightweight and Strong Glass Fiber Reinforced Polypropylene Composite Foams Achieved by Mold-Opening Microcellular Injection Molding. *J. Mater. Res. Technol.* 2021, 14, 2920–2931.

[19] Shaayegan, V.; Wang, G.; Park, C. B. Study of the Bubble Nucleation and Growth Mechanisms in High-Pressure Foam Injection Molding Through In-Situ Visualization. *Eur. Polym. J.* 2016, 76, 2–13.

[20] Wang, G.; Zhao, G.; Dong, G.; Mu, Y.; Park, C. B.; Wang, G. Lightweight, Super-Elastic, and Thermal-Sound Insulation Bio-Based PEBA Foams Fabricated by High-Pressure Foam Injection Molding with Mold-Opening. *Eur. Polym. J.* 2018, 103, 68–79.

[21] Ellingham, T.; Kharbas, H.; Manitiu, M.; Scholz, G.; Turng, L.-S. Microcellular Injection Molding Process for Producing Lightweight Thermoplastic Polyurethane with Customizable Properties. *Front. Mech. Eng*. 2018, 13, 96–106.

[22] Pinchuk, L.; Wilson, G. J.; Barry, J. J.; Schoephoerster, R. T.; Parel, J. M.; Kennedy, J. P. Medical Applications of Poly(Styrene-Block-Isobutylene-Block-styrene) (‘‘SIBS’’). *Biomaterials* 2008, 29, 448–460.

[23] Fittipaldi, M.; Rodriguez, L. A.; Grace, L. R. The Effect of Water Absorption on the Viscoelastic Properties of Poly(Styrene-Block-Isobutylene-Block-Styrene) for Use in Biomedical Applications. *AIP Conf. Proc.* 2015, 1664, 030003-1–030003-5.

[24] Koshimura, K.; Sato, H. Application Study of Styrene-Isobutylene-Styrene Block Copolymer as a New Thermoplastic Elastomer. *Polym. Bull.* 1992, 29, 705–711.

[25] Ahmed, M. F.; Li, Y.; Yao, Z.; Cao, K.; Zeng, C. TPU/PLA Blend Foams: Enhanced Foamability, Structural Stability, and Implications for Shape Memory Foams. *J. Appl. Polym. Sci*. 2019, 136, 47416.

[26] Huang, A.; Peng, X.; Turng, L.-S. In-Situ Fibrillated Polytetrafluoroethylene (PTFE) in Thermoplastic Polyurethane (TPU) via Melt Blending: Effect on Rheological Behavior, Mechanical Properties, and Microcellular Foamability. *Polymer* 2018, 134, 263–274.

[27] Li, X.; Wang, G.; Yang, C.; Zhao, J.; Zhang, A. Mechanical and EMI Shielding Properties of Solid and Microcellular TPU/Nanographite Composite Membranes. *Polym. Test*. 2021, 93, 106891.

[28] Sharudin. R. W.; Nabil, A.; Taki, K.; Ohshima, M. Polypropylene-Dispersed Domain as Potential Nucleating Agent in PS and PMMA Solid-State Foaming. *J. Appl. Polym. Sci*. 2011, 119, 1042−1051.

[29] Banerjee, R.; Ray, S. S. Foamability and Special Applications of Microcellular Thermoplastic Polymers: A Review on Recent Advances and Future Direction. *Macromol. Mater. Eng.* 2020, 305, 2000366.

[30] Ishihara S., Hikima, Y.; Ohshima, M. Preparation of Open Microcellular Polylactic Acid Foams with a Microfibrillar Additive Using Coreback Foam Injection Molding Processes. *J. Cell. Plast.* 2018, 54, 765−784.

[31] Trent, J. S.; Scheinbeim, J. I.; Couchman., P. R. Ruthenium Tetraoxide Staining of Polymers for Electron Microscopy. *Macromolecules* 1983,16, 589−598.

[32] Ohlsson, B.; Törnell, B.; The Use of $Ru0_4$ in Studies of Polymer Blends by Scanning Electron Microscopy. *J. Appl. Polym. Sci.* 1990, 41, 1189−1196.

[33] Himelfarb, P. B.; Labat, K. B. Characterization of Polymer Blends and Block Copolymers by Conventional and Low Voltage SEM. *Scanning* 1990, 12, 148−154.

[34] Kumar, V.; Suh, N. P. A Process for Making Microcellular Thermoplastic Parts. *Polym. Eng. Sci*. 1990, 30,1323−1329.

[35] Wang, L.; Hikima Y.; Ohshima, M.; Yusa, A.; Yamamoto, S.; Goto, H. Unusual Fabrication of Lightweight Injection-Molded Polypropylene Foams by Using Air as the Novel Foaming Agent. *Ind. Eng. Chem. Res*. 2018, 57, 3800−3804.

[36] Wang, L.; Hikima, Y.; Ishihara, S.; Ohshima, M. Fabrication of High Expansion Microcellular Injection-Molded Polypropylene Foams by Adding Long-Chain Branches. *Ind. Eng. Chem. Res*. 2016, 55, 11970–11982.

[37] Dealy, J. M.; Larson, R. G. *Structure and Rheology of Molten Polymers*; Hanser: Cincinnati, 2006.

[38] Antony, P.; Puskas, J. E. Investigation of the Rheological and Mechanical Properties of a Polystyrene-Polyisobutylene-Polystyrene Triblock Copolymer and Its Blends with Polystyrene. *Polym. Eng. Sci*. 2003, 43, 243−253.

[39] Han, C. D.; Baek, D. M.; Kim, J. K.; Ogawa, T.; Sakamoto, N.; Hashimoto, T. Effect of Volume Fraction on the Order-Disorder Transition in Low Molecular Weight Polystyrene-Block-Polyisoprene Copolymers. 1. Order-Disorder Transition Temperature Determined by Rheological Measurements, *Macromolecules* 1995, 28, 5043−5062.

[40] Han, C. D.; Kim, J.; Kim, J. K. Determination of the Order-Disorder Transition Temperature of Block Copolymers. *Macromolecules* 1989, 22, 383−394.

[41] Taki, K.; Kitano, D.; Ohshima, M. Effect of Growing Crystalline Phase on Bubble Nucleation in Poly(L-Lactide)/CO_2 Batch Foaming. *Ind. Eng. Chem. Res.* 2011, 50, 3247–3252.

[42] Shaayegan, V.; Wang, G.; Park, C. B. Effect of Foam Processing Parameters on Bubble Nucleation and Growth Dynamics in High-Pressure Foam Injection Molding. *Chem. Eng. Sci.* 2016, 155, 27−37.

[43] Hossieny, N. J.; Barzegari, M. R.; Nofar, M.; Mahmood, S. H.; Park, C. B. Crystallization of Hard Segment Domains with the Presence of Butane for Microcellular Thermoplastic Polyurethane Foams. Polymer 2014, 55, 651–662.

[44] Puskas, J. E.; Antony, P.; El Fray, M.; Altstädt, V. The Effect of Hard and Soft Segment Composition and Molecular Architecture on the Morphology and Mechanical Properties of Polystyrene–Polyisobutylene Thermoplastic Elastomeric Block Copolymers. *Eur. Polym. J.* 2003, 39, 2041–2049.

[45] van Dijk, M. A.; van den Berg, R. Ordering Phenomena in Thin Block Copolymer Films Studied Using Atomic Force Microscopy. Macromolecules 1995, 28, 6773–6778.

[46] Zhao, J.; Qiao, Y.; Wang, G.; Wang, C.; Park, C. B. Lightweight and Tough PP/Talc Composite Foam with Bimodal Nanoporous Structure Achieved by Microcellular Injection Molding. *Mater. Des*. 2020, 195, 109051.

[47] Li, D.; Chen, Y.; Yao, S.; Zhang, H.; Hu, D.; Zhao, L. Insight into the Influence of Properties of Poly(Ethylene-co-octene) with Different Chain Structures on Their Cell Morphology and Dimensional Stability Foamed by Supercritical CO_2. *Polymers* 2021, 13, 1494.

Chapter 3 Improvement of the Surface Quality of Foam Injection Molded Products from a Material Property Perspective

3.1 Introduction

As described in Chapter 1, it is known that microcellular plastic foaming with environmentally benign foaming agents is a technique of growing interest that contributes to sustainable development.[1-4] Compared with standard polymer foams, microcellular foams of cell sizes less than 100 μm and cell densities higher than 10^8 cells/cm^3 show a higher strength-to-weight ratio, better dimensional stability, and lower deterioration of mechanical strength. These features provide microcellular foams with various applications including packaging materials, sports equipment, automobile parts, and thermal insulators,[5-6] which is also discussed in Chapter 1. Since microcellular plastic foams were invented, numerous studies have been conducted on processes and materials. Microcellular foams were produced using batch, extrusion, bead foaming, and foam injection molding (FIM) processes.[1] Among these processes, FIM was considered cost-effective for producing microcellular plastic foams because of its shorter molding cycles. Furthermore, combining microcellular foam injection molding with a core-back or precise mold opening operation could produce higher expansion foams with fine cellular structures.

Despite these advantages, the low surface quality of FIM microcellular foam is a significant problem that limits its industrial applications, especially in the usage of exterior parts. Swirl marks and silver streaks are two common defects that seriously deteriorate the surface appearance of foams. The swirl marks and silver streaks are gas flow marks caused by bubbles trapped on the mold surface when the injected molten polymer was solidified. These are caused mainly by a mechanism in which bubbles nucleated at the melt flow front in the filling stage, are stretched, broken, pushed to the mold side by the fountain flow behavior, and trapped.[7-9] The large broken cells on the surface cause the swirl marks, while the smaller oriented cells form silver streaks.[8]

Several studies have been conducted to reduce and eliminate these surface imperfections. Lee et al.[10] aimed to improve the surface quality by reducing the bubble nucleation rate. They decreased the degree of supersaturation of the physical blowing agent (PBA) in the injected polymer to lower the bubble nucleation rate at the melt flow front. They succeeded in reducing the

swirl marks; however, their scheme contradicted the production of fine foams with a high expansion ratio, which usually requires higher gas content and a higher degree of supersaturation of the PBA.

A typical scheme for improving the surface quality of foams is to control the mold temperature using mold temperature control units with several thermal heating devices or insulators. The scheme was initially developed for erasing weld lines. The rapid heat and cooling mold technique (RHCM) and thermal cycling molding (RTCM) are two representative techniques of the scheme.[11-17] In these technologies, the mold cavity surface is heated rapidly, and during the filling stage, the mold wall temperature is kept high enough for bubbles at the mold surface to be eliminated.[13-15] Some thermal insulators might be inserted into the mold to keep the interface temperature between the mold and the injected molten polymer high.[16,17] The mold temperature control methods are effective; however, the cost of the mold is increased, and the production cycle time is also increased.

The gas counterpressure (GCP) process is another approach that can suppress bubble nucleation at the flow front during the filling stage.[18-20] Before injecting the polymer, high-pressure gas is introduced into the mold cavity to suppress bubble nucleation at the flow front. Then, the pressure is released through a vent hole of the mold before completely filling out the cavity with the polymer. Related to the technique using gas pressure, Hou and coworkers developed a method of combining gas-assisted microcellular injection molding (GAMIM).[21] In operation, pressurized gas is injected into a foaming core polymer through the gas inlets to ensure the completion of the filling stage. Then, the high pressure is held for a certain period to compress the injected polymer to the mold surface and squeeze or erase the bubbles on the surface.

Other methods of improving the surface quality are the in-mold decoration process (IMD) and co-injection or sandwich injection molding, where a solid skin material (metallic or polymeric parts) is introduced before a foaming core polymer is injected.[22,23] By building a sandwiched structure (solid skin-foam core-solid skin), the imperfection of the foam parts is concealed with the introduced skin materials. Guo et al. reported an interesting experimental result using a mold wall decollated with PET film.[24] The film achieved an asymmetrical temperature distribution. Then, bubbles traveled to the PET side due to higher temperature and were flattened by significant shear flow.

From the viewpoint of polymer properties, some methods have been proposed. Lee et al. improved the surface quality of LDPE foams by using a low-molecular-weight polymer as a slip agent.[25] Wang et al. used a nanofiller to enhance the melt strength and the surface quality of PP nanocellular foams prepared by foam injection molding technology.[26] The bubbles can be visually ignored because of their small size.[27] From the early stage of microcellular foam development, it has been believed that higher melt strength or strain hardening behavior is a beneficial polymer property for forming tiny bubbles and preventing bubble breakup during the filling stage.[28-29]

As mentioned above, there are many promising methods for improving the surface quality of foam. Two common key concepts exist in those methods, excluding the IMD. One is to reduce the number and size of the bubbles nucleated at the melt front during the filling stage. The other is to squeeze and erase the bubbles by giving some stress before the polymer is solidified. In this study, keeping these two key concepts in mind, we proposed a method of improving the surface quality of PP microcellular foams from the polymer property aspect. PP is a commercial semicrystalline thermoplastic polymer, and PP microcellular foams have been developed for several automobile parts because of their light weight, low cost, and easy recycling.[30,31] SIBS can be used to introduce the heterogeneity into PP and act as viscosity modifier. The effect of SIBS on surface quality improvement was investigated. LMPP and MD were used to improve the surface quality of the PP microcellular foams. The gelling agent (MD) prevents bubbles from growing and reduces bubble size. LMPP slows the PP crystallization rate, lowers the viscosity of the polymer at the interface, and delays the crystallization at the skin, resulting in producing enough time to squeeze and dissolve the bubbles on the surface. Using this additive and blending with a low-crystalline polymer, we conducted several microcellular foam injection molding experiments with the core-back operation by changing the LMPP blend ratios.

3.2 Experimental

3.2.1 Materials

Thermoplastic elastomer styrene-isobutylene-styrene (SIBS062M, Kaneka, Osaka, Japan) was added as a modifier to introduce the heterogeneity and control the viscosity. Homopolypropylene (HPP, J105G, Prime Polymer Co., Ltd., Japan) with a weight-average molecular weight (M_w) of 260,000 g/mol and melt flow rate (MFR) of 9.0 g/10 min (at 230 ^oC)

was used as the base resin. Low modulus polyolefin (LMPP: L-MODU S901, Idemitsu Kosan Co., Ltd., Japan) with 130,000g/mol M_w and a 50 g/10 min melt flow rate (at 230 ^oC) was used as a blend polymer to control the crystallization rate and crystallization temperature. The blend ratios tested in this study are summarized in Table 3.1 with the abbreviations of the sample name. The sorbitol-based gelling agent (bis-O-(4 methylphenyl) methylene-D-Glucitol: MD, New Japan Chemical Co., Ltd., Japan) was used to control the viscosity at a low strain rate range. A master batch of PP with 3%MD additive was compounded and provided by the same company. When MD was used, the master batch was mixed with the HPP/LMPP blends at the hopper to be 0.3 or 0.5 wt.% content. Since a higher content of MD induces agglomeration of the additive and results in less efficacy, MD was reduced to the most effective content.[32] Nitrogen (N_2, Izumi Sanyo, Japan) with 99.9% purity was used as a physical blowing agent (PBA).

Table 3.1 Compositions of investigated polymers.

Blend	Blend ratio (wt %)
HPP	100/0
HPP/10%SIBS	90/10
HPP/20%SIBS	80/20
HPP/30%SIBS	70/30
HPP/20%LMPP	80/20
HPP/30%LMPP	70/30
HPP/40%LMPP	60/40
HPP/60%LMPP	40/60
HPP/0.3%MD	99.7/0/0.3
HPP/30%LMPP/0.3%MD	69.7/30/0.3

3.2.2 Foaming Experiments

Foam injection molding experiments were conducted using a 35-ton clamping force MuCell machine (J35EL III-F, Japan Steel Work, Japan) with a gas delivery unit (SCF device SII TRJ-10-A-MPD, Trexel Inc., USA). A cylindrical screw 20 mm in diameter with an L/D ratio of 40:1 and a mold with a rectangular-shaped cavity (70 mm × 50 mm × 1 mm) were used for injection molding experiments. N_2 was pressurized to 24 MPa by the gas delivery system and injected into

the molten polymer in the middle of the barrel of the injection molding machine through an injector valve. A single-phase solution of molten polymer and 0.11 wt.% N_2 was injected into the mold cavity. The N_2 concentration was controlled by manipulating the injector valve opening time. The details of the mold geometry and operation of FIM are described in our previous papers.[32,33] The nozzle zone and metering zones of the injection molding machine were set at 200 ^oC. The mold temperature was maintained at 40 ^oC. Two infrared temperature sensors and two pressure sensors were independently deployed in the mold cavity to measure the polymer temperatures and pressures at different locations in the cavity: one location was close to the inlet, and the other was at the flow end, as shown in Figure 3.1. By averaging the temperatures and pressures at two points of three injection cycles, the temperature and the pressure profiles during a cycle of injection molding were calculated and plotted against the processing time, as shown in Figure 3.18 in the Supporting Information of Chapter 3. The infrared temperature sensors were used to measure the polymer temperature at approximately 0.4 mm inside from the mold-polymer interface in the thickness direction. The cooling rate of the polymer in the holding process was estimated from the recorded temperature profiles to be -35 $^oC/s$ on average.

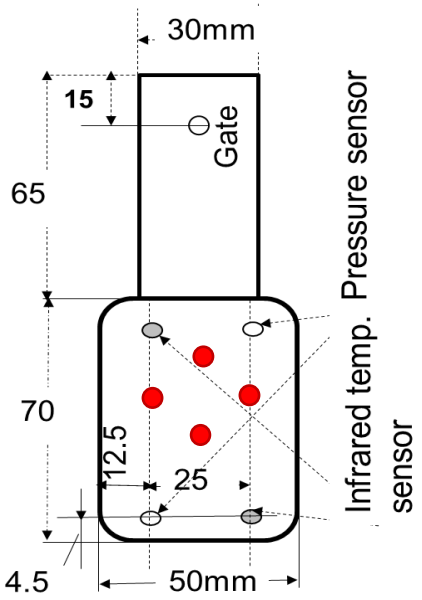

Figure 3.1 Geometry of injection-molded sample, sensor locations, and roughness measuring points.

FIM with core-back (precise mold opening) operation was applied to produce foams. The difference between core-back and conventional FIM lies in an additional mold-opening operation. In the core-back FIM process, a part of the mold is quickly opened to expand cavity volume. This mold opening operation initiates bubble nucleation and growth by the rapid pressure drop and produces a cellular structure. In the experiments, the mold part was opened at a rate of 20 mm/s. The expansion ratio of foams was set to five by setting the core-back (mold opening) distance to 4 mm from a 1-mm initial cavity thickness (total 5 mm in foam thickness). The processing parameters are summarized in Table 3.2.

Table 3.2 Processing parameters of foam injection molding with core-back operation.

Parameters	**Values**
Polymer temperature [^{o}C]	200
Mold temperature [^{o}C]	40
Injection speed [mm/s]	80
Screw back pressure [MPa]	15
Packing (holding) pressure [MPa]	40
Cooling time [s]	30
Core-back distance [mm]	4
Core-back speed [mm/s]	20
Metering distance [mm]	35
N_2 content [%]	0.11

3.2.3 Rheological Characterization

Strain-controlled dynamic frequency sweep and temperature sweep rheological measurements were conducted using a rheometer (ARES, TA Instruments, Inc., New Castle, DE, USA) with a 25-mm parallel-plate device. Before the measurement, specimens 25 mm in diameter and 2 mm in thickness were prepared using a hot compressing machine at a temperature of 200 ^{o}C and compression pressure of 20 MPa. Frequency sweep tests for HPP, HPP/SIBS and HPP/LMPP blends were carried out by changing the shear rate frequency from 100 to 0.1 rad/s with 1% strain at a temperature of 200 ^{o}C. This was kept at 200 ^{o}C for 3 min to erase the thermal history. To

further clarify the effect of MD in the frequency sweep test, the experimental temperature was also set at 170 °C for HPP, HPP/30%LMPP, HPP/0.3%MD, and HPP/30%LMPP/0.3%MD. Prior to the experiment, the temperature was increased to 230 °C and kept for 3 min to erase the effect of PP crystallization and completely dissolve MD into PP. The temperature sweep measurements were conducted at 100–200 °C with a 1% strain amplitude and a frequency of 0.63 rad/s. The damping rate was set at 5 °C/min.

Torsion tests were also conducted to analyze the viscosity of HPP-based blends at low temperature, with a 1% strain amplitude and a frequency of 0.63 rad/s. The damping rate was also set at 5 °C/min.

3.2.4 Measurement of Thermal Properties

Isothermal and nonisothermal measurements were conducted using a Flash DSC1 (Mettler-Toledo, LLC, USA) under N_2 purging. For isothermal measurement, the temperature was first heated to 230 °C, held for 1 s, reduced at a cooling rate of 4000 °C/s, and held at a designated isothermal crystallization temperature. The heat generation or crystallization enthalpy was measured for the isothermal temperature designated in the range of 0 to 110 °C. The isothermal crystallization rate and the half crystallization time were estimated by fitting Eqs. (3-1) and (3-2)[34] to the DSC data.

$$\log\{-\ln[1 - X(t)]\} = \log k + n \log t \qquad (3\text{-}1)$$

$$t_{1/2} = (\frac{\ln 2}{k})^{1/n} \qquad (3\text{-}2)$$

where $X(t)$ represents the relative crystallinity, k is the crystallization rate, and t is the time. n is the Avrami index, and $t_{1/2}$ is the half crystallization time.

Since the cooling rate of the injected polymer in the mold cavity was estimated to be -35 °C/s on average, as illustrated in Figure 3.18, nonisothermal measurement was conducted by cooling the polymer samples at -35 °C/s after heating to 230 °C at 1000 °C/s. Then, the effect of SIBS and LMPP on the crystallization temperature was observed from the heating curve.

Besides, normal DSC (DSC7020, Hitachi, Tokyo, Japan) at low cooling rate was employed to examine not only the effect on crystallization temperature but also the crystallization amount

for the HPP/SIBS blends, where normal DSC is more suitable than Flash DSC due to very small sample amount used in Flash DSC. The cooling rate in the measurements was -10 °C/min. The sample amount was fixed at around 5.62 mg with an error less than 1%. The crystallinity of HPP was then obtained using Eq. (3-3):

$$X_c(\%) = \frac{\Delta H_m}{\Delta H_m^0} \times HPP\ blend\ ratio \times 100 \qquad (3\text{-}3)$$

where ΔH_m is the enthalpy of melting peak, and ΔH_m^0 represents the fusion enthalpy of a fully crystalline PP, which was 207 J/g here.[35]

3.2.5 Surface Roughness Analysis

The surface roughness of the foams was quantitatively measured using a laser microscope (LEXT OLS4100, Olympus, Japan). The cutoff values of the high-pass filter λ_c and low-pass filter λ_s were set to 2500 and 0 μm, respectively. The cutoff values of the two filters were tuned to reduce the influence of undulation and observe the silver stream or bubble footprint clearly. The magnification of the microscope was 5x. Four points on every three injection molded samples were selected for each foam injection molding condition to measure the roughness. The four points measuring the surface roughness are indicated in Figure 3.1.

The surface roughness was calculated with the arithmetical mean height (*Sa*) value, Eq. (3-4): A lower *Sa* indicates fewer defects and a smoother surface area.

$$Sa = \frac{1}{A} \iint_A |Z(x,y)|\, dxdy \qquad (3\text{-}4)$$

where *A* is the measuring area, and *Z* (*x*, *y*) indicates the height of the surface at locations *x* and *y*.

In addition to the *Sa* value, 2D and 3D images of foam surfaces were taken by laser microscopy to clearly verify the effect of LMPP and MD on surface quality. The cutoff values of high-pass and low-pass filters were set to 2500 and 30 μm for 3D laser images to reduce the influence of noise.

The surface visual appearance was observed by employing a digital camera. Carbon black was added to all polymers to clearly observe the silver streaks or the swirl marks on the surface of the injection molded samples.

3.2.6 Observation of Solid and Cell Morphology

For solid morphology observation, all specimens were cut out from the middle parts of the nonfoamed injection-molded products after cryogenically fracturing in liquid nitrogen. Then specimens were immersed in 10 mL Acetone to extract the SIBS for over 20 hours with a stirring speed of 100 rpm and temperature of 30 ^{o}C. Prior to observation by a scanning electron microscope (JCM-7000 NeoScope, JEOL Ltd., Japan), treated specimens were dried in vacuo for at least 6 hours and subsequently coated by a carbon coater (SC-701CT, Sanyu Electron Co., Ltd., Japan).

For cell morphology observation, a small sliced specimen was cut from the foam injection-molded product after cryogenically solidified in liquid nitrogen. The observation was made by a scanning electron microscope (SEM: Tiny-SEM, Technex, Japan) in both perpendicular and parallel directions to the core-back direction, i.e., the thickness direction of the foam, as prepared in previous work.[32]

3.3 Results and Discussion

3.3.1 Rheological Properties of HPP with SIBS Addition

The effect of SIBS on rheological properties was also studied by temperature and frequency sweep tests. As clearly seen in torsion test data of Figure 3.2a, the viscosity of HPP/SIBS blends was decrease with increasing content of SIBS in the low-temperature region, which is favorable to bubble dissolution at polymer/mold interface. When HPP crystals melt at higher than 120 ^{o}C, shown in Figure 3.2b, higher SIBS content led to higher viscosity. Figure 3.19 illustrates the frequency sweep data of HPP/SIBS blends, where complex viscosities show difference with different blend ratios in the low-frequency range. As SIBS content increased, the complex viscosity was increased. When increasing SIBS content to 30%, the complex viscosity showed shear thinning behavior, indicating the significant chain entanglement in the presence of high content of SIBS.

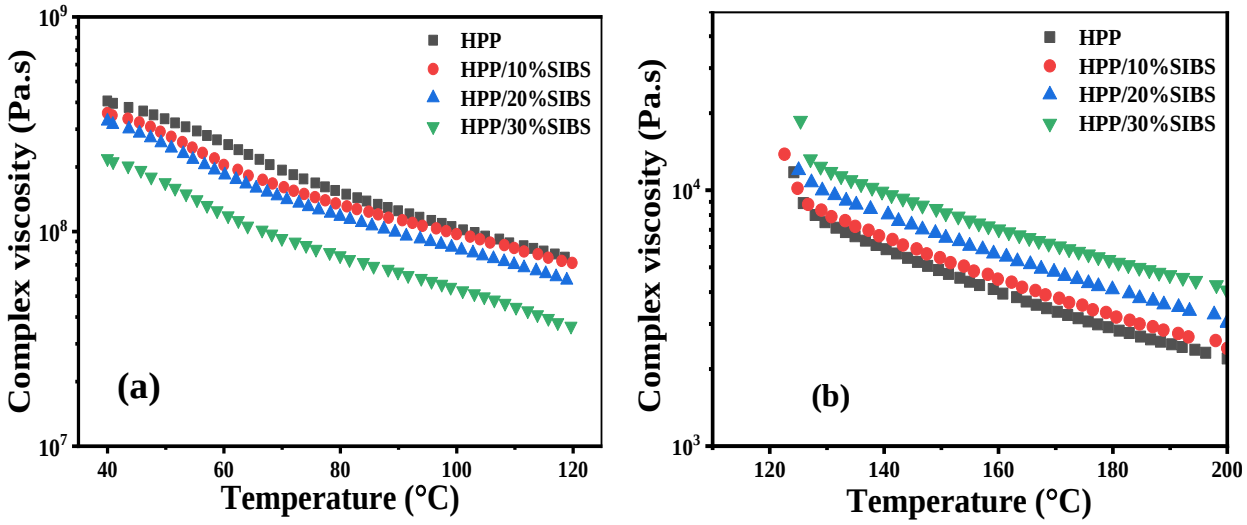

Figure 3.2 Complex viscosity of HPP and HPP/SIBS blends against temperature: (a) Temperature lower than 120 °C; (b) Temperature higher than 120 °C.

3.3.2 Rheological Properties of HPP with LMPP and MD Addition

Figure 3.3 shows the temperature-sweep measurements of the complex viscosities of four materials (HPP, HPP/20%LMPP, HPP/40%LMPP, and HPP/60%LMPP) measured at a cooling rate of -5 °C/min. The viscosities of these four materials increased as the temperature decreased. Blending LMPP reduced the viscosity to a lower value than that of the neat HPP. Figure 3.3a shows the viscosities of all blends lower than 120 °C. The decrease in viscosity could be seen with increased LMPP content, which can be beneficial for bubble dissolution at the polymer/mold interface. As shown in Figure 3.3b, all materials showed a drastic change in viscosity in the range of 120-130 °C. This change indicates the occurrence of crystallization, and the corresponding turning point temperature can be regarded as the crystallization temperature at a cooling rate of -5 °C/min. The crystallization onset temperature of neat HPP was 125.86 °C, while those of PP/20%, 40%, and 60% LMPP were 124.12 °C, 121.35 °C, and 119.19 °C, respectively. The crystallization onset temperature shifted to a lower temperature with increased LMPP content. The decreased crystallization temperature indicates that LMPP acts as a crystallization retarding agent in the blend. Figure 3.20 shows the viscosities of HPP and HPP/LMPP blends as a function of frequency. As the LMPP content increased, the viscosity decreased over the entire frequency range. It is also noticeable that the viscosities of all materials decreased in the high-frequency region.

The influence of MD on the viscosity of HPP was investigated by temperature and frequency sweep tests. As reported previously,[32,36,37] adding MD to PP increases the viscosity and the melt strength. Because the formation of the nanofibril network of MD occurs as a phase separation phenomenon of MD from the molten polymer,[32] the complex viscosity increased at temperatures below 170 °C, as shown in Figure 3.4. This viscosity increase widens the foaming temperature window for suppressing bubble growth and keeping the bubble size on the micrometer scale.[36-37] Figure 3.21 shows the frequency-sweep complex viscosity of HPP and HPP/LMPP with 0.3% MD addition. The temperatures of measurement were 200 °C and 170 °C. Figure 3.21a shows the complex viscosities of these materials at 200 °C. It is clear that HPP/0.3%MD had the highest viscosity among these materials across the entire frequency range. Moreover, viscosity decreased with LMPP addition. Figure 3.21b shows the complex viscosities of these materials at 170 °C. The viscosities of HPP/0.3%MD and HPP/30%LMPP/0.3%MD were higher than those of HPP and the HPP/LMPP blend, respectively, due to reinforcement of MD. The presence of in situ formation of the MD nanofibril network in the molten polymer[32] increases the viscosity of HPP and HPP/LMPP in the low-frequency (strain rate) range. These changes in the rheology of PP possibly provide the benefit of reducing the bubble size not only for bubbles generated in the foam core part but also those generated at the flow front of the injected polymer.

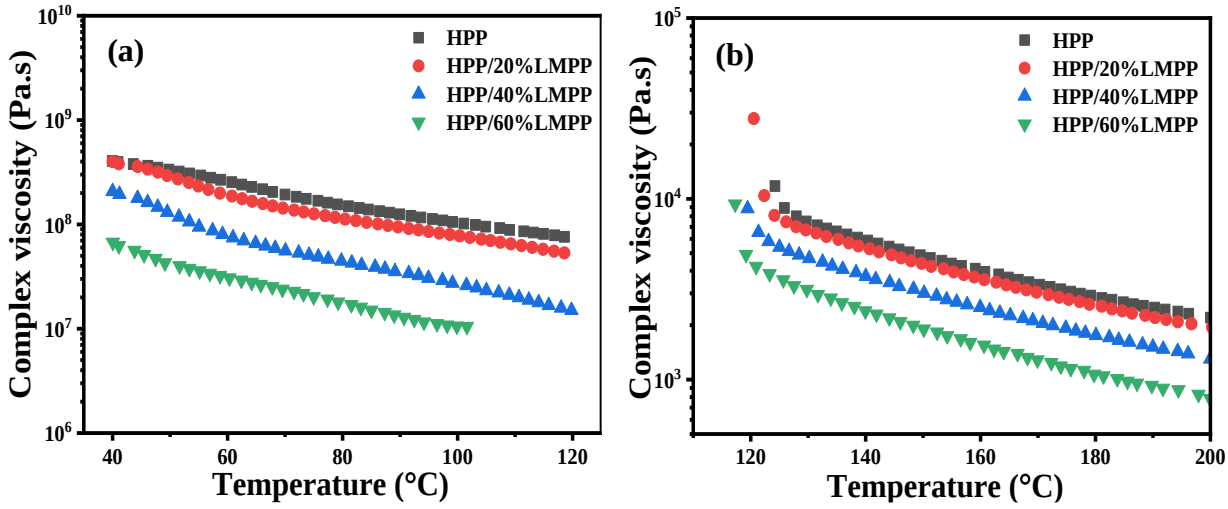

Figure 3.3 Complex viscosity of neat HPP and HPP/LMPP blends with 20, 40, and 60 wt.% LMPP content as a function of temperature.

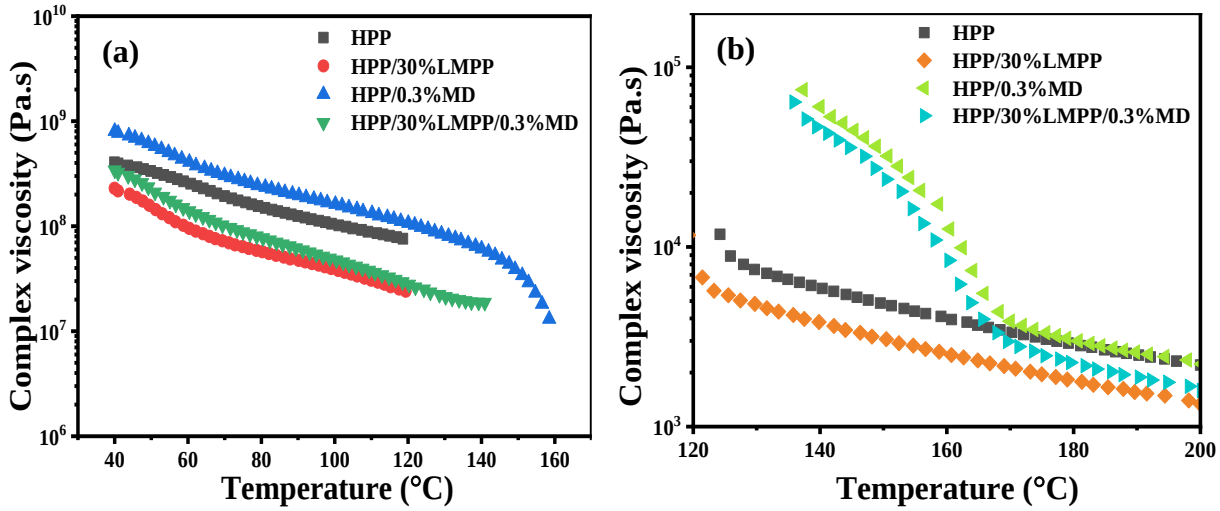

Figure 3.4 Complex viscosity of HPP, HPP/30%LMPP, HPP/0.3%MD, and HPP/30%LMPP/ 0.3%MD against temperature.

3.3.3 Crystallization Kinetics at High Cooling Rate of HPP/SIBS Blends

Figure 3.5 show results of the crystallization rate *k* and half crystallization time $t_{1/2}$ of HPP and HPP/SIBS blends for isothermal crystallization conditions. In Figure 3.5a, the crystallization rates of all materials didn't significantly change. In Figure 3.5b, the half crystallization times shows similar trend even with increased SIBS content. In addition, Figure 3.6 shows nonisothermal data with a cooling rate of -35 °C/s, where no obvious shift of crystallization peaks was observed. These data indicate that there is no significant crystallization retarding effect of SIBS on HPP crystallization. This conclusion can be also drawn in terms of rheological data in Figure 3.2.

Flash DSC is only suitable for measurement of effect of cooling rate on crystallization behavior, while normal DSC can be employed to measure the effect of crystallization amount. Figure 3.22 shows exothermic peaks of the nonisothermal condition at a cooling rate of -10 °C/min for HPP/SIBS blends. Table 3.4 lists the crystallinity of HPP in different SIBS blends. Both of them signify the reduction in crystallization amount with SIBS addition which can be the reason for decrease in mechanical properties in Figures 3.25 and 3.26.

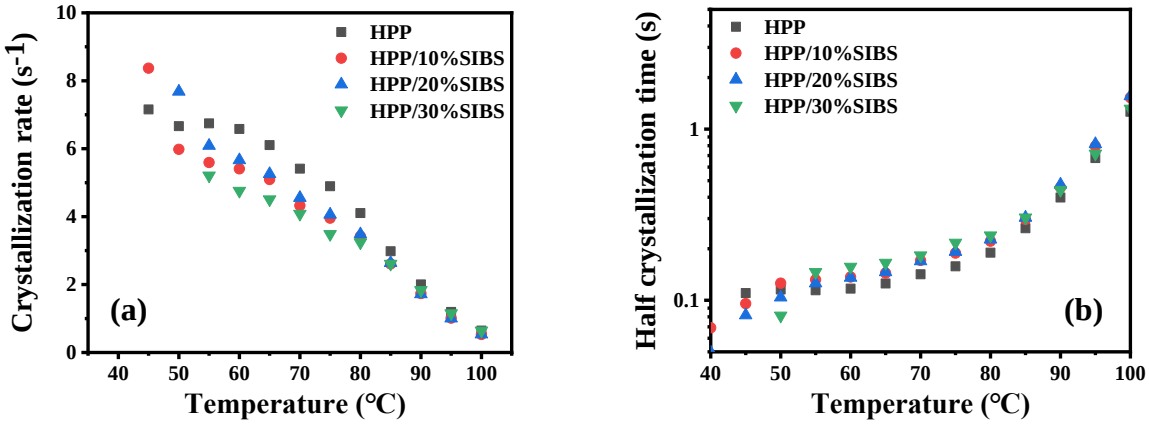

Figure 3.5 Crystallization rate and half crystallization time of HPP and HPP/SIBS blends.

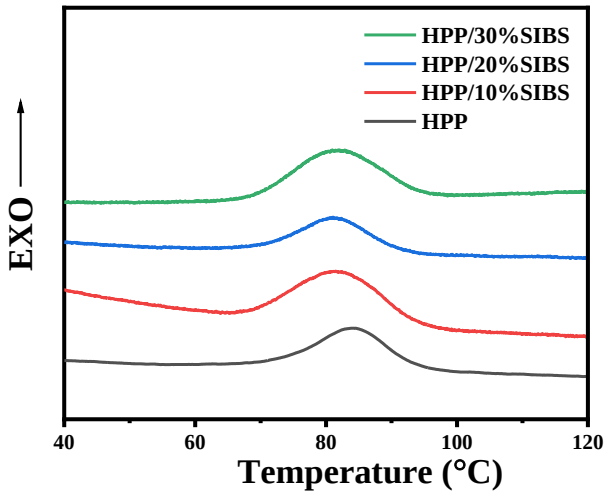

Figure 3.6 Cooling curves of HPP and HPP/SIBS blends measured at a cooling rate of -35 °C/s.

3.3.4 Crystallization Kinetics at High Cooling Rate of HPP/LMPP Blends

Flash DSC measurements were conducted to clarify the crystallization retarding effect of the LMPP for both isothermal crystallization and faster cooling (nonisothermal) conditions. Figure 3.7 shows the results of the crystallization rate k and half crystallization time $t_{1/2}$ of HPP and HPP/LMPP blends for isothermal crystallization conditions. In Figure 3.7a, the crystallization rate of HPP was highest at all temperatures. With an increase in LMPP content, the crystallization rate was reduced. The crystallization rate of HPP/60%LMPP could be lower than 1 s^{-1} at 40 °C, which corresponds to the molding temperature. As the LMPP content increased, the half crystallization

time became considerably longer, as shown in Figure 3.7b. Both results in Figure 3.7 indicate that LMPP delays the crystallization of HPP.

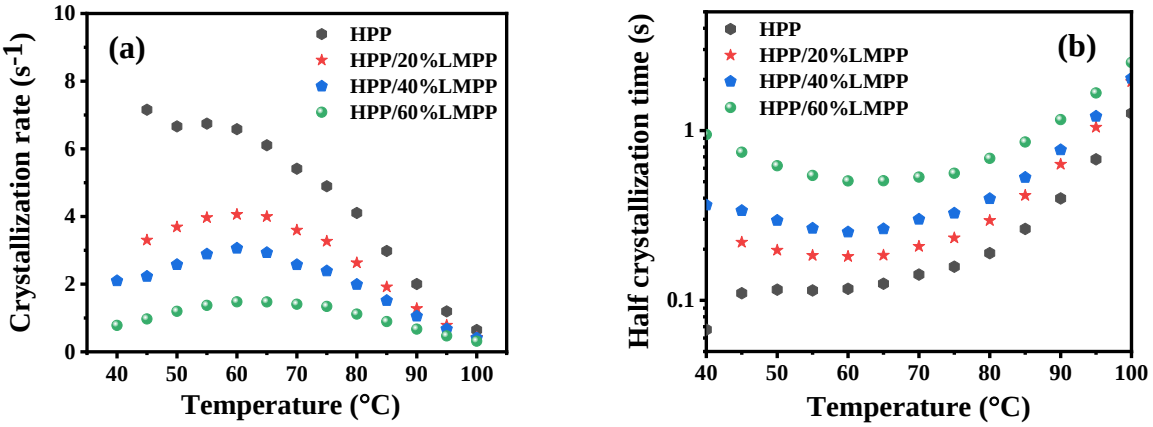

Figure 3.7 Crystallization rate and half crystallization time of HPP and HPP/LMPP blends.

Figure 3.8 shows the heat generation curves of the nonisothermal condition at a cooling rate of -35 °C/s for HPP/LMPP blends. The temperature at which the curves peaked was regarded as the crystallization temperature. The crystallization temperature results are listed in Table 3.3 for each sample. The crystallization temperature decreased as the LMPP content increased. No crystallization peak was observed when the LMPP was increased to 60%. These results indicate that LMPP delays HPP crystallization even for fast-cooling conditions such as the cooling rate in mold cavity.

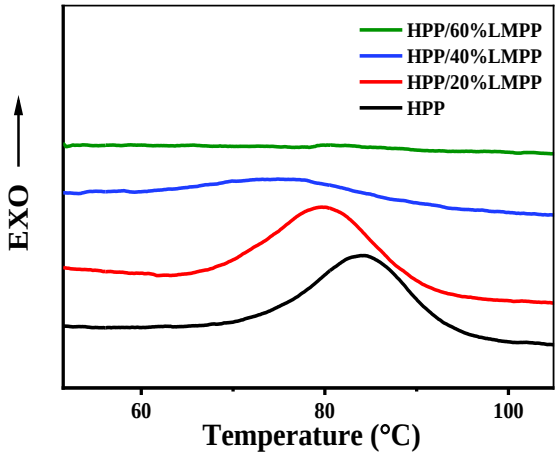

Figure 3.8 Cooling curves of HPP and HPP/LMPP blends measured at a cooling rate of -35 °C/s.

Table 3.3 Crystallization peaks of HPP and HPP/LMPP blends at a cooling rate of -35 ^{o}C/s.

Parameters	HPP	HPP/20% LMPP	HPP/40% LMPP	HPP/60% LMPP
Peak Temperature [^{o}C]	85.59	81.49	76.89	-

3.3.5 Surface Roughness Evaluation of HPP Foams with SIBS Addition

Figure 3.9 shows the *Sa* of foam injection-molded parts prepared from HPP and HPP/SIBS with different blend ratios. Interestingly, the *Sa* was reduced with introduction of SIBS when comparing the *Sa* result of HPP foam in Figure 3.9. Although there was no significant crystallization retarding effect of SIBS on HPP crystallization according to Figures 3.5 and 3.6, the viscosities lower than crystallization temperature for HPP/SIBS blends were lower than that of HPP. This indicates that low viscosity is beneficial for bubble dissolution at polymer/mold interface. However, effect of SIBS is limited compared with LMPP because SIBS can reduce the viscosity but it does not delay the crystallization. HPP can be crystallized as it is even if SIBS exists. When SIBS content was increased to 30%, the *Sa* was increased. This result can be attributed to denser and larger SIBS domains for HPP/30%SIBS shown in Figure 3.10, where grey area was HPP matrix, while white particles were dispersed SIBS domains. SIBS domains of HPP/10%SIBS were much smaller (highlighted by red circles) than those of HPP/30%SIBS. Large and dense domains in HPP/30%SIBS blend could induce the formation of large bubbles and ease of bubble coalescence at flow front, resulting in increase in *Sa*.

Figure 3.11 shows the 2D and 3D images of the surfaces of injection-molded HPP/SIBS blend foams. The observation areas of both the 2D and 3D images were fixed at 2548×2559 μm^2. Clearly, serrations and ripples of HPP/SIBS blends foams were reduced compared with HPP foam. With increased content of SIBS, surface roughness of foam increased.

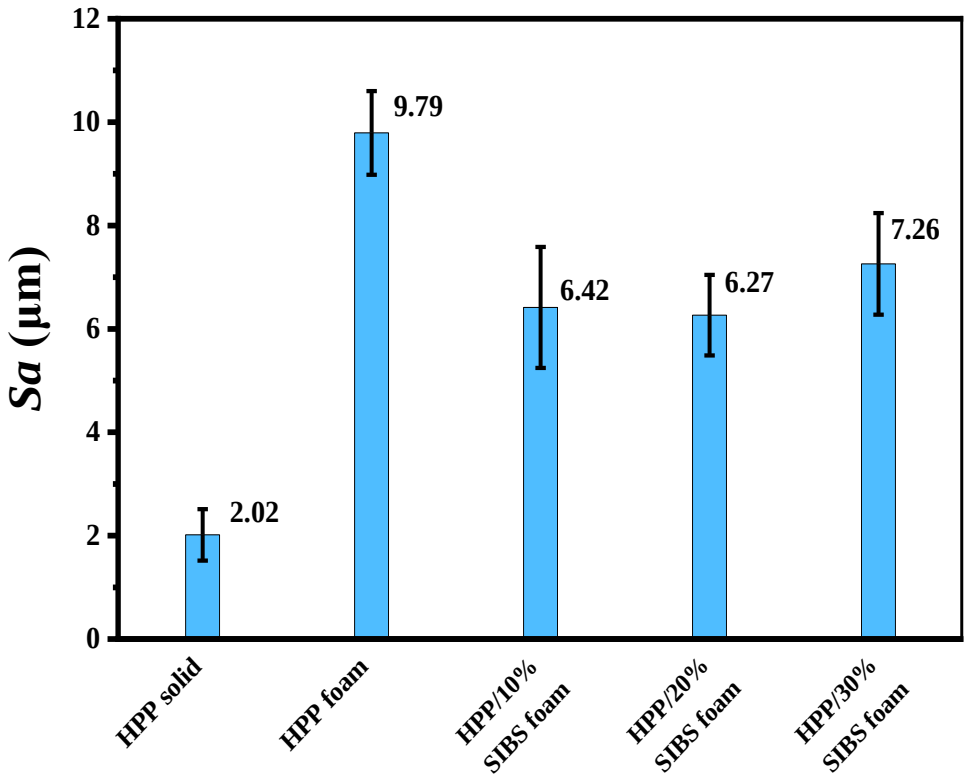

Figure 3.9 Surface roughness (*Sa*) of HPP solid, HPP foam, HPP/SIBS blend foams.

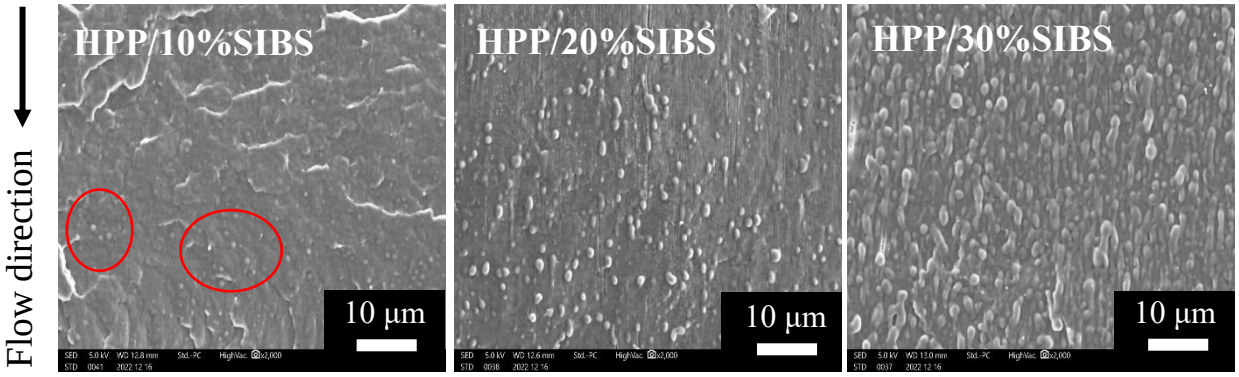

Figure 3.10 Solid morphologies of HPP/SIBS blends: grey area is HPP matrix and dispersed particles are SIBS domains.

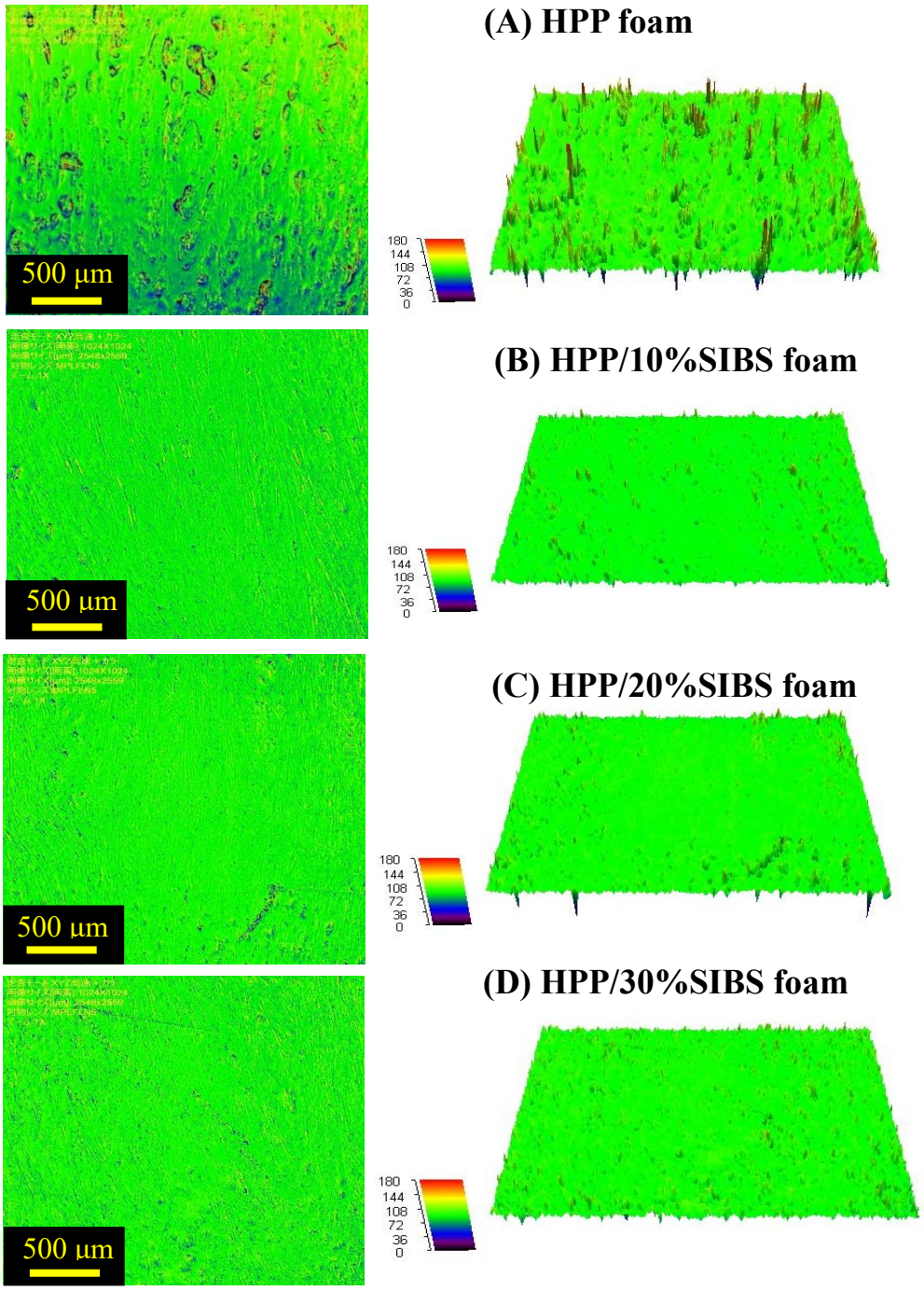

Figure 3.11 Two-dimensional (2D) and Three-dimensional (3D) laser microscope images of injection molded parts: (A) HPP foam; (B) HPP/10%SIBS foam; (C) HPP/20%SIBS foam; (D) HPP/30%SIBS foam. For 2D (λ_c = 2500 µm and λ_s = 0 µm) and 3D (λ_c = 2500 µm and λ_s = 30 µm).

3.3.6 Surface Roughness Evaluation of HPP Foams with LMPP and MD Addition

Figure 3.12 shows the *Sa* of foam injection-molded parts prepared from HPP and HPP/LMPP with different blend ratios. The HPP solid (nonfoamed) sample had the lowest *Sa* at ca. 2.02 μm. When polymers were foamed with N_2, *Sa* of HPP foam samples increased to ca. 9.79 μm, indicating an increase in surface roughness. The *Sa* of the foam-injection-molded part decreased with increasing LMPP content. The values of *Sa* for foams of HPP/20%, 30%, 40%, and 60% LMPP were 9.10, 9.02, 6.08 and 4.03 μm, respectively. When LMPP was blended at 60%, the surface of the foams became almost equivalent to that of HPP solid by naked eye and laser microscope images of λ_s = 30 μm.

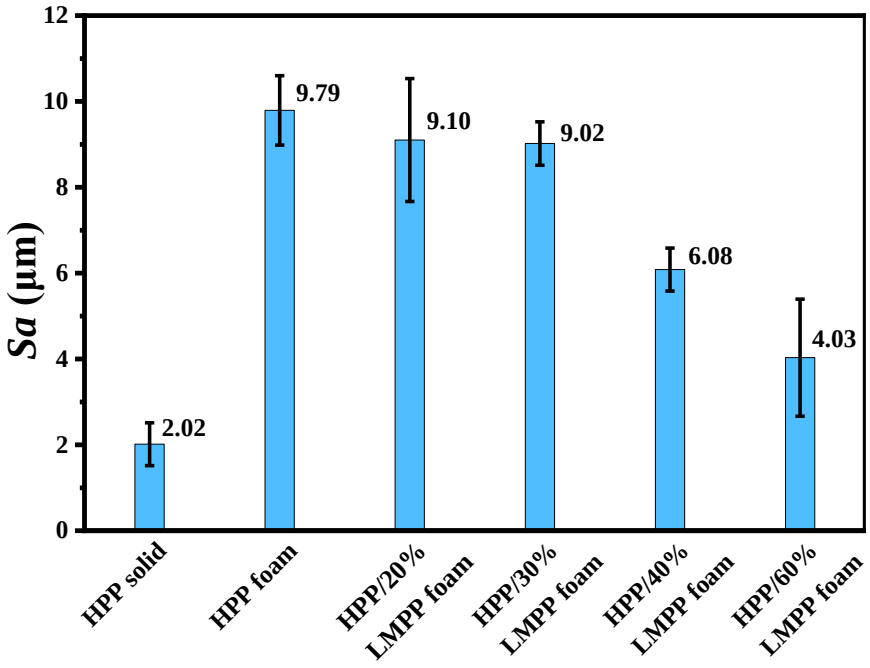

Figure 3.12 Surface roughness (*Sa*) of HPP solid, HPP foam and HPP/LMPP foams with different blend ratios.

In the Supporting Information (Section S3), Figure 3.23 shows the *Sa* of the foamed injection molded HPP with two different amounts of MD: 0.3 and 0.5 wt.%. As we expected, adding MD can improve the surface quality. Figure 3.13 shows the *Sa* values of foam-injection-molded parts prepared from HPP (solid), foamed HPP, HPP/0.3%MD, and HPP/30%LMPP with 0.3%MD. As shown in Figure 3.13, when MD (0.3%) was used together with 30%LMPP, the

surface roughness was lower than that of HPP/40%LMPP (Figure 3.12) and became closer to that of the HPP solid injection molded parts. This indicates that a synergetic effect of MD and LMPP occurs to improve the surface quality.

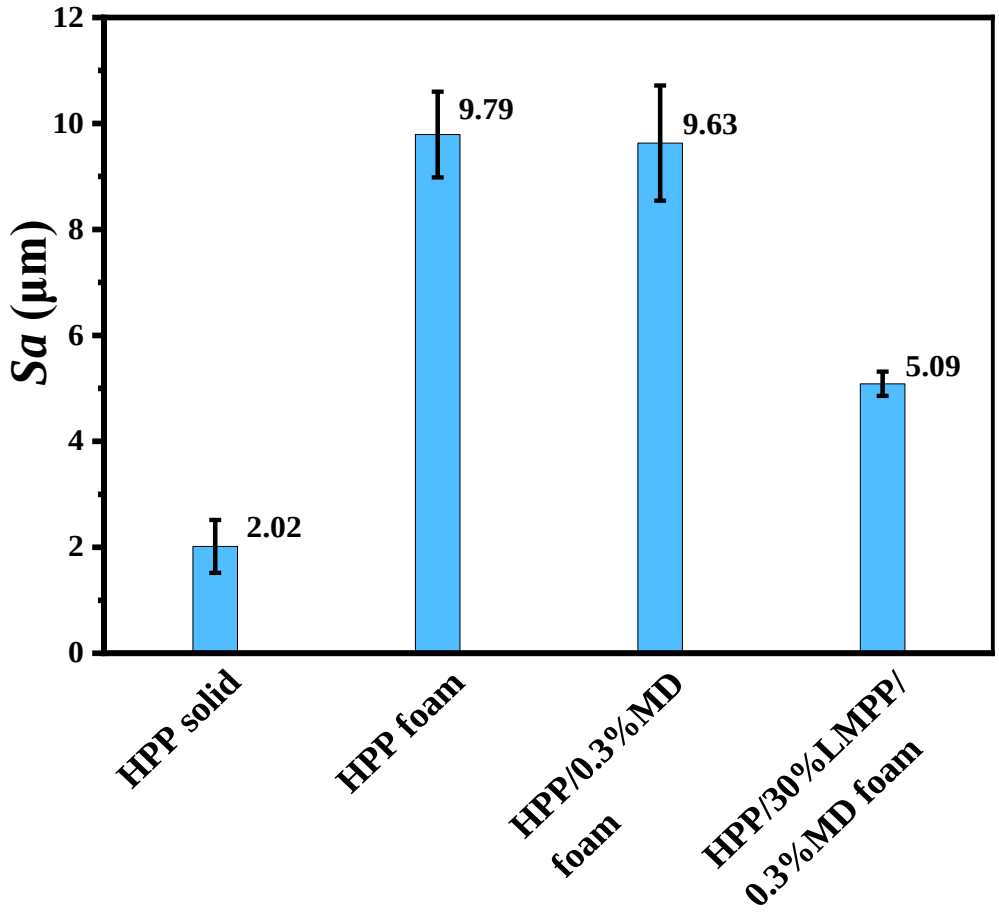

Figure 3.13 Surface roughness (*Sa*) of HPP solid, HPP foam, HPP/0.3%MD foam, and HPP/30%LMPP/0.3%MD foam.

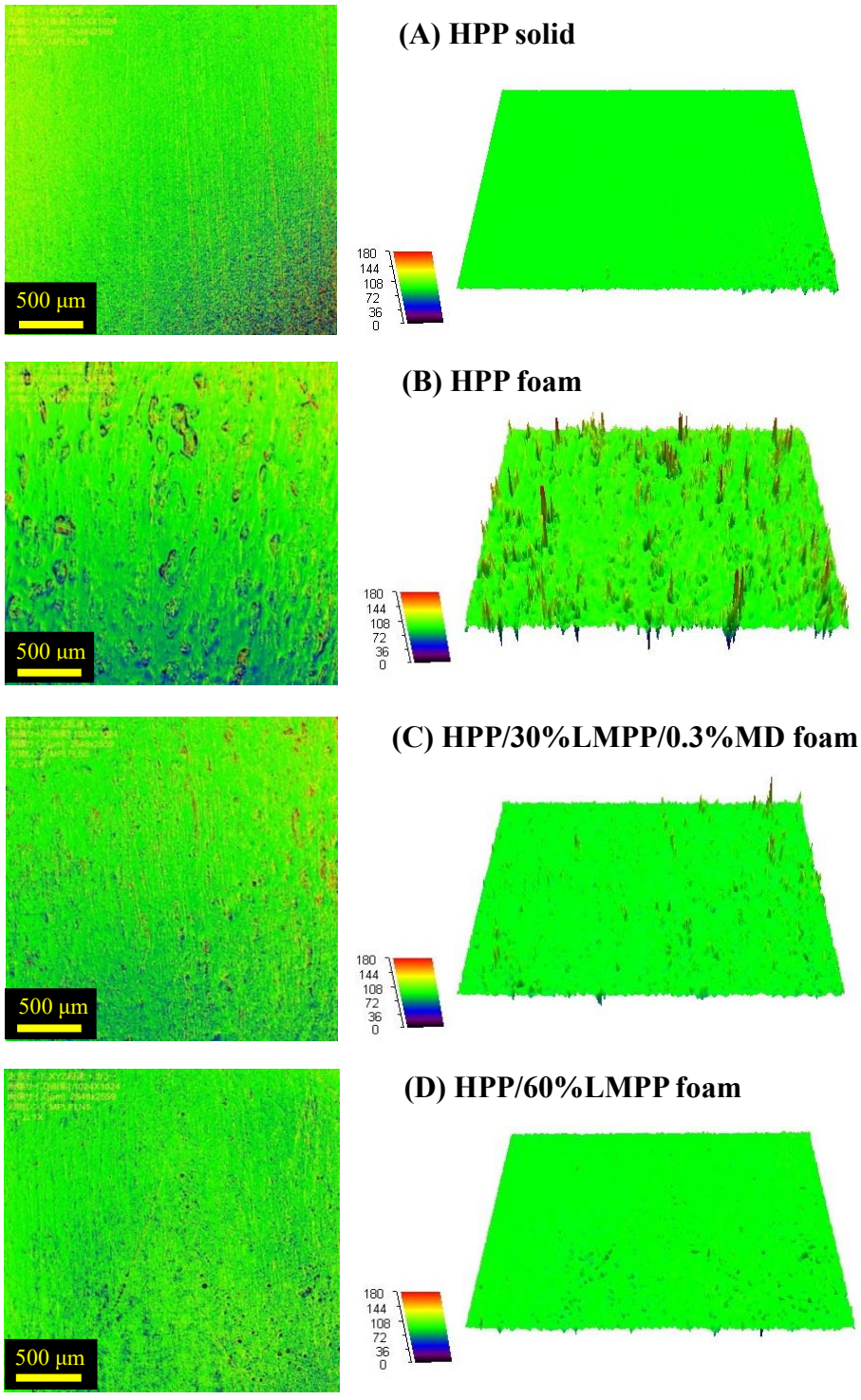

Figure 3.14 Two-dimensional (2D) and Three-dimensional (3D) laser microscope images of injection molded parts: (A) HPP solid, (B) HPP foam, (C) HPP/30%LMPP/0.3%MD foam, and (D) HPP/60%LMPP foam. For 2D (λ_c = 2500 µm and λ_s = 0 µm) and 3D (λ_c = 2500 µm and λ_s = 30 µm).

Figure 3.14 shows the 2D and 3D images of the surfaces of injection-molded solid HPP, HPP foam, HPP/30%LMPP/0.3%MD foam, and HPP/60%LMPP foam. The observation areas of both the 2D and 3D images were fixed at $2548 \times 2559\ \mu m^2$. When foam injection molding was conducted, serrations or ripples were observed in the 2D and 3D laser microscope images of the HPP foam, corresponding to the footprints of the bubbles on the surface. For HPP/60%LMPP, there are few serrations and ripples, and the image is very close to that of HPP solid. When compare the image of HPP/30%LMPP/0.3%MD foam with HPP/30%LMPP shown in Figure 3.24a in the Supporting Information (Section S3), the efficacy of MD on the surface roughness can be seen.

Figure 3.15 shows digital camera images of the injection-molded parts. A carbon black (CB) color batch pellet made of 60 wt.% polyethylene (MFR = 15) and 40 wt.% CB was added to each investigated polymer to observe the silver streak and bubbles on the foam surface easily by the naked eye. The upper right figure is a magnified image of each sample. HPP/30%LMPP/0.3%MD foam showed low surface roughness, but footprints of silver streaks remained. These surface imperfections vanished when the HPP was increased to 60 wt.%. The surface quality of the foam was equivalent to that of HPP solid.

The surface quality improvement can be correlated to the crystallization-delaying effect of LMPP and the viscosity effect of MD. The trapped bubbles are known to cause surface roughness during the solidification of foam skin. With the addition of MD, the size of the bubbles generated at the flow front became small and easily squeezed in a short time by the holding pressure. Furthermore, blending LMPP with HPP delays the crystallization of HPP and provides a time to squeeze or erase the bubbles and silver streaks by the holding pressure before the solidification of the injected polymer is completed. The 60%LMPP blend prevents the injected polymer from crystallizing at a fast cooling rate; the surface of the HPP/60%LMPP blend foam becomes equivalent to that of the HPP solid.

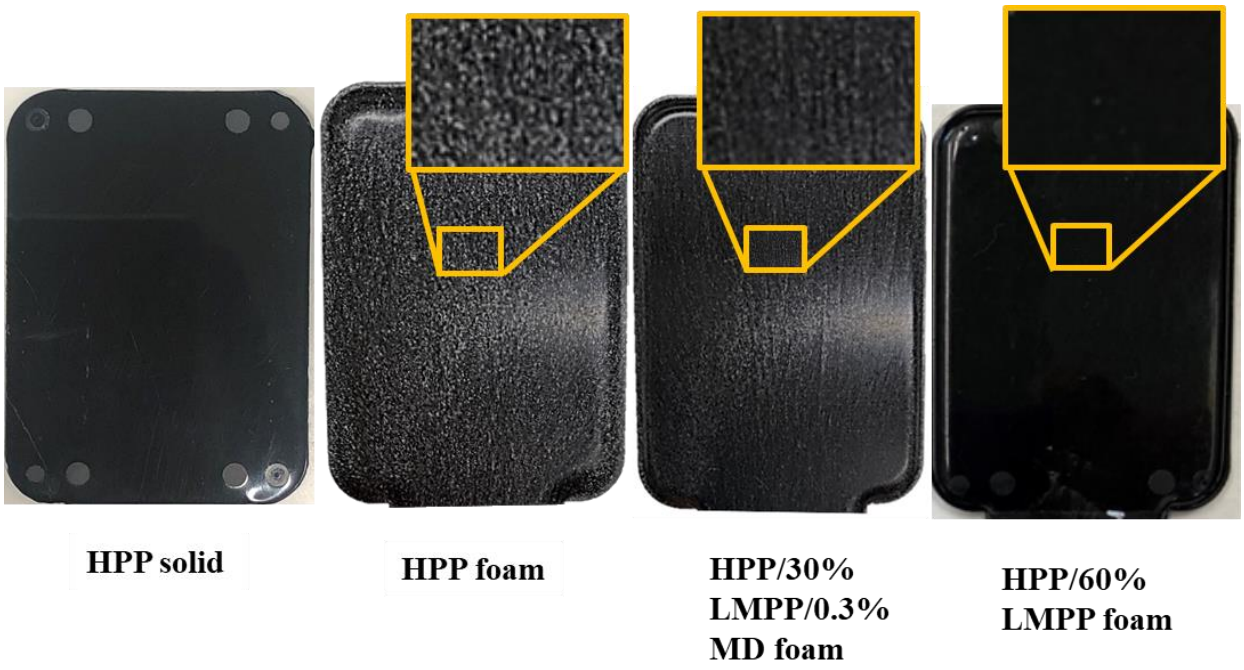

Figure 3.15 Digital camera images of nonfoamed HPP, HPP foam, HPP/30%LMPP/0.3%MD foam, and HPP/60%LMPP foam.

3.3.7 Effect of SIBS on Cell Morphology

The cell morphology of HPP/SIBS blend foams indicates the enhanced cell nucleation with SIBS. As seen in Figure 3.16, HPP/20%SIBS foam had smaller cell size amongst these three kinds of foam. This is reasonable because HPP/20%SIBS foam had higher heterogeneity compared with that of HPP/10%SIBS foam, while had lower foaming temperature than that of HPP/30%SIBS foam. The higher foaming temperature of HPP/30%SIBS foam can be the reason to formation of larger cell and higher *Sa* in Figure 3.9.

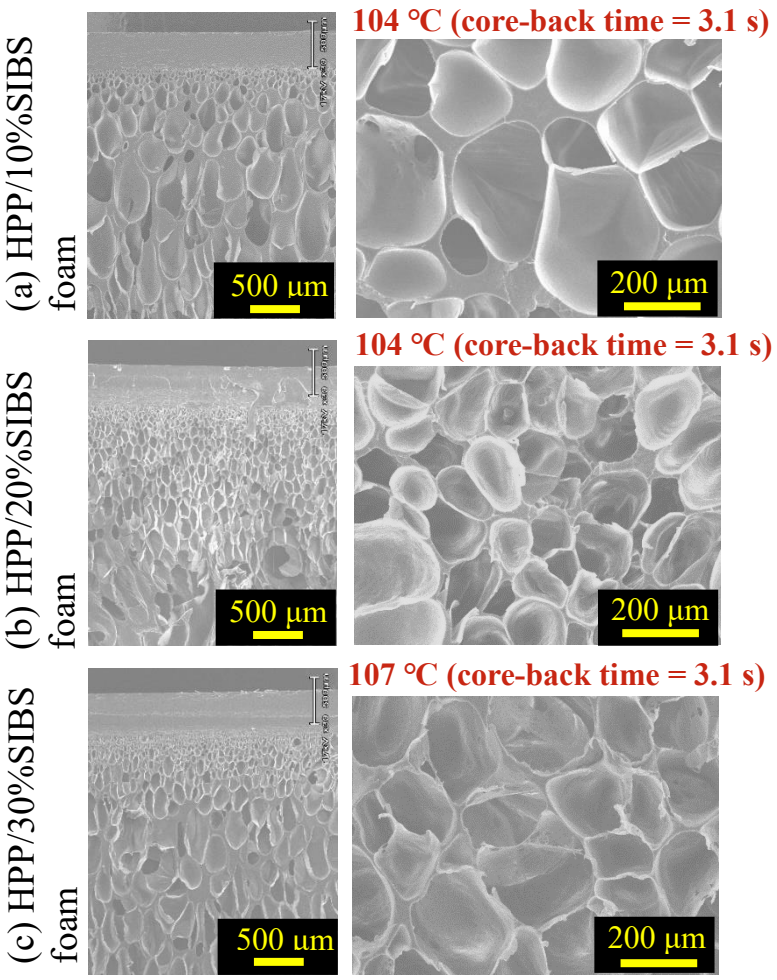

Figure 3.16 SEM images of cell morphology: (a) HPP/10%SIBS foam; (b) HPP/20%SIBS foam; (c) HPP/30%SIBS foam at five-fold expansion. Left: a cross-sectional image taken parallel to the core-back direction (thickness direction); Right: a cross-sectional image taken perpendicular to the core-back direction.

3.3.8 Effect of LMPP and MD on Cell Morphology

Figures 3.17 and 3.31 illustrate the SEM images of the cell morphology of the five-fold expanded foams with LMPP and MD. Each figure's left-side image was a cross-sectional area near a skin layer of the foam, taken from a view parallel to the core-back direction, i.e., foam thickness direction. The right-side image was a cross-sectional area of the foam core, taken from a view

perpendicular to the core-back direction. The dotted circle indicates the presence of elongated bubbles on the surface. As seen in Figure 3.17, elongated bubbles on the surface of the HPP/60%LMPP and HPP/30%LMPP/0.3%MD are rarely seen while they could be observed on the surface of HPP foam.

All polymers could be foamed to be five-fold by manipulating the foaming temperature. The cell morphology was dependent on the core-back time, i.e., foaming temperature. The foaming temperature was the temperature at the point where the core-back operation was conducted, as shown in Figure 3.18. The longer the core-back time is, the lower the foaming temperature becomes.

With the increased LMPP content, the cell size became larger, as observed in SEM cell morphology images of HPP (Figure 3.17a), HPP/20%LMPP (Figure 3.31a), and HPP/30%LMPP (Figure 3.31b) prepared at the foaming temperature around 100 ºC. When LMPP was increased by over 60%, the cell size became too large unless the foaming temperature was lowered. By prolonging the core-back time and decreasing the foaming temperature from 100 ºC to 80 ºC, the five-fold expansion foams could be prepared from HPP/60%LMPP with smaller cell sizes than those of HPP and HPP/20%LMPP foams (Figure 3.31a), as shown in Figure 3.17c.

Interestingly, with the increase in LMPP content, the thickness of the skin layer became thinner owing to viscosity reduction and slow crystallization rate. On the other hand, adding MD made the skin layer thicker when the foams were prepared at the same foaming temperature. However, MD decreased the cell size and improved the cell morphology drastically even when the foams were prepared at a higher temperature. This is because MD reduces the crystal nuclei's size and provides more bubble nucleation sites to the polymer when foaming.[32,37]

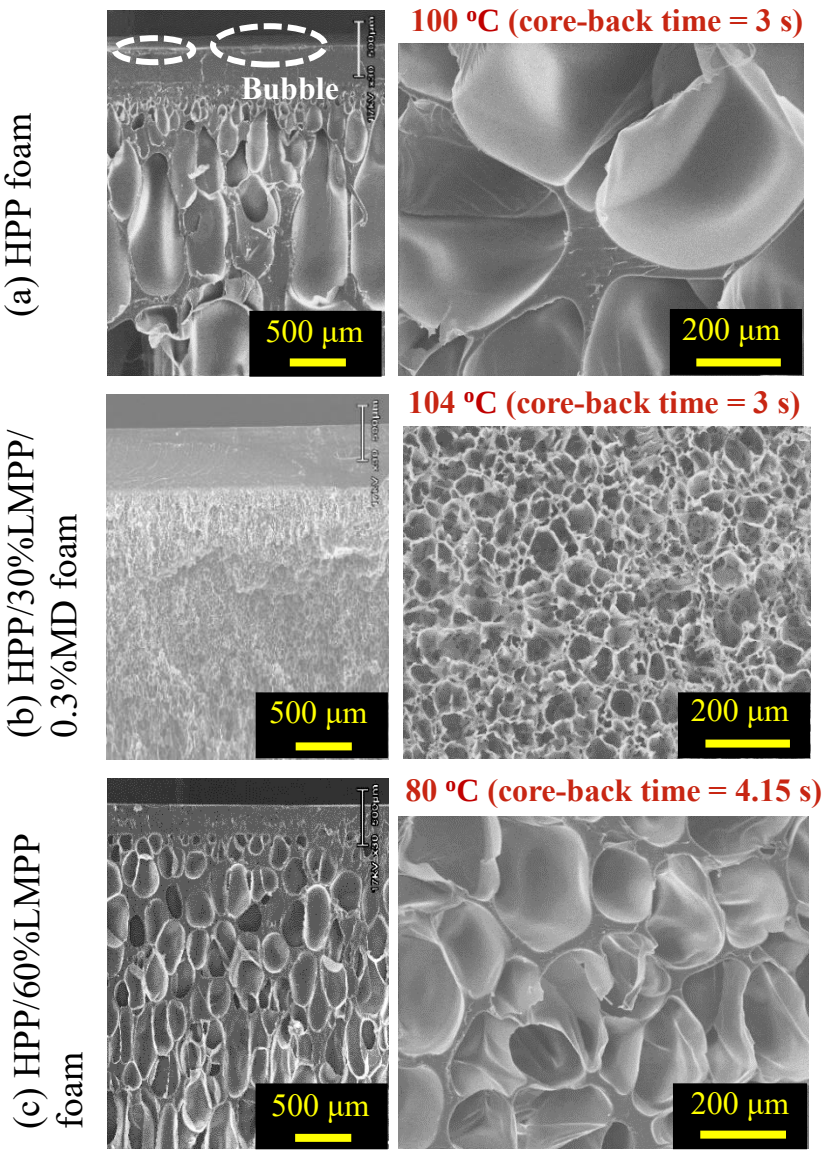

Figure 3.17 SEM images of cell morphology: (a) HPP; (b) HPP/30%LMPP/0.3%MD; (c) HPP/60%LMPP foams at five-fold expansion. Left: a cross-sectional image taken parallel to the core-back direction (thickness direction); Right: a cross-sectional image taken perpendicular to the core-back direction.

3.4 Conclusion

Adding crystal nucleating agent, MD, increases the viscosity with a gelling effect and can reduce the size of bubbles generated at the flow front of injected polymers. Blending a low-

modulus polypropylene delays or prevents the crystallization of the injected polymer at the mold interface. The retardation effect on crystallization provides time to squeeze and erase broken bubbles or silver streaks at the skin layers during the holding pressure stage. Blending 60%LMPP with HPP results in silver-streak-free microcellular PP foams. Adding MD and using LMPP can provide synergetic effects on surface quality improvement.

With introduction of SIBS, the *Sa* of HPP/SIBS blend foam was reduced. The introduction of SIBS can enhance the heterogeneity and control the viscosity. Since there was no significant crystallization retarding effect of SIBS, the improvement of surface quality was not as effective as LMPP. When SIBS content was increased to 30%, the *Sa* was also increased, which is attributed to large nucleated bubbles at flow front. The nucleation of those large bubbles is probably caused by large SIBS domains in HPP/30%SIBS blend.

With the increase of LMPP content, mechanical properties such as Young’s modulus and yield stress were lowered, and the polymers' softness was increased, as shown in Figures 3.27 and 3.28. However, the foams' mechanical properties depend on the cell morphology. The cell morphology could be controlled by manipulating the core-back time and the degree of expansion ratio.

MD was used to reduce the size of bubbles push to the interface between the mold and polymer. The amount of physical blowing agent (PBA) might be also a key parameter in determining the bubbles' size. When the concentration of the PBA exceeds a certain level where the PBA cannot be entirely dissolved in polymer, or it produces so many bubbles to easily coalesce each other, large size bubbles and swirl mark will appear on the skin layer, which indeed deteriorates the surface appearance. Thus, it can be said that increasing PBA concentration can improve the surface quality as far as the cell size is reduced.

This study demonstrated the feasibility of a surface quality improvement method proposed from the viewpoint of polymer properties, especially with regard to crystallization and viscosity behaviors. Surface imperfections are considered an unavoidable drawback of the microcellular injection molding process. However, this study showed that the problem can be solved by controlling the bubble size and crystallization behavior. The proposed method can be further enhanced by increasing mold temperature or combining the heating and cooling method.

References

[1] Banerjee, R.; Ray, S. S. Foamability and Special Applications of Microcellular Thermoplastic Polymers: A Review on Recent Advances and Future Direction. Macromolecular Materials and Engineering. *Macromol. Mater*. Eng. 2020, 305, 2000366.

[2] Kumar, V.; Suh, N. P. A Process for Making Microcellular Thermoplastic Parts. *Polym. Eng. Sci*. 1990, 30, 1323–1329.

[3] Jiang J.; Li, Z.; Yang, H.; Wang, X.; Li, Q.; Turng, L.-S. Microcellular Injection Molding of Polymers: a Review of Process Know-How, Emerging Technologies, and Future Directions. *Curr. Opin. Chem. Eng.* 2021, 33, 100694.

[4] Ding, Y.; Hassan, M. H.; Bakker, O.; Hinduja, S.; Bártolo, P. A Review on Microcellular Injection Moulding. *Materials* 2021, 14, 4209.

[5] Klempner, D.; Frisch, K. C. *Handbook of Polymeric Foams and Foam Technology*; Hanser Publishers: Munich, 1991.

[6] Lee, S. T.; Ramesh, N. S. *Polymeric foams: Mechanical and Materials*; CRC Press: Boca Raton, 2004.

[7] Wang, Y.; Hu, G. H. Research Progress of Improving Surface Quality of Microcellular Foam Injection Parts. *Appl. Mech. Mater.* 2011, 66–68, 2010–2016.

[8] Hu, G.; Hu, B. Surface Morphology Analysis of Microcellular Foam Injection Parts Molded Using the PP/N_2 System. *Madridge J. Nanotechnol Nanosci*. 2016, 1, 14–21.

[9] Wang, G.; Zhao, G.; Wang, J.; Zhang, L. Research on Formation Mechanisms and Control of External and Inner Bubble Morphology in Microcellular Injection Molding. *Polym. Eng. Sci.* 2015, 55, 807–835.

[10] Lee, J.; Turng, L.-S.; Dougherty, E.; Gorton, P. A Novel Method for Improving the Surface Quality of Microcellular Injection Molded Parts. *Polymer* 2011, 52, 1436–1446.

[11] Pierick, D. E.; Anderson, J. R.; Cha, S. W.; Chen, L. Stevenson, J. F.; Laing, D. E. US Patent, 6884823, 2005.

[12] Sato, Y.; Yamaki, M.; Nunome, M.; Imakawa, A.; Takamura, M.; Shido, K. Ono-Sangyo, Mitsui Chemical, JP Patent, 3977565, 2007.

[13] Xiao, C.-L.; Huang, H.-X.; Yang, X. Development and Application of Rapid Thermal Cycling Molding with Electric Heating for Improving Surface Quality of Microcellular Injection Molded Parts. *Appl. Therm. Eng*. 2016, 100, 478–489.

[14] Wang, G.; Zhao, G.; Guan, Y. Thermal Response of an Electric Heating Rapid Heat Cycle Molding Mold and Its Effect on Surface Appearance and Tensile Strength of the Molded Part. *J. Appl. Polym. Sci.* 2013, 128, 1339–1352.

[15] Zhang, A.; Zhao, G.; Guan, Y. Effects of Mold Cavity Temperature on Surface Quality and Mechanical Properties of Nanoparticle-Filled Polymer in Rapid Heat Cycle Molding. *J. Appl. Polym. Sci*. 2015, 132, 41420.

[16] Yoon, J. D.; Hong, S. K.; Kim, J. H.; Cha, S. W. A Mold Surface Treatment for Improving Surface Finish of Injection Molded Microcellular Parts. *Cell. Polym.* 2004, 23, 39–48.

[17] Lee, J.; Turng, L.-S. Improving Surface Quality of Microcellular Injection Molded Parts through Mold Surface Temperature Manipulation with Thin Film Insulation. *Polym. Eng. Sci.* 2010, 50, 1281–1289.

[18] Bledzki, A. K.; Kirschling, H.; Steinbichler, G.; Egger, P. Polycarbonate Microfoams with a Smooth Surface and Higher Notched Impact Strength. *J. Cell. Plast.* 2004, 40, 489–496.

[19] Chen, S.-C.; Hsu, P.-S.; Hwang, S.-S. The Effects of Gas Counter Pressure and Mold Temperature Variation on the Surface Quality and Morphology of the Microcellular Polystyrene Foams. *J. Appl. Polym. Sci*. 2013, 127, 4769–4776.

[20] Ren, J.; Lin, L.; Jiang, J.; Li, Q.; Hwang, S.-S. Effect of Gas Counter Pressure on the Surface Roughness, Morphology, and Tensile Strength between Microcellular and Conventional Injection-Molded PP Parts. *Polymers* 2022, 14, 1078.

[21] Hou, J.; Zhao, G.; Wang, G.; Dong, G.; Xu, J. A Novel Gas-Assisted Microcellular Injection Molding Method for Preparing Lightweight Foams with Superior Surface Appearance and Enhanced Mechanical Performance. *Mater. Des.* 2017, 127, 115–125.

[22] Turng, L.-S.; Kharbas, H. Development of a Hybrid Solid-Microcellular Co-Injection Molding Process. *Int. Polym. Process.* 2004, 19, 77–86.

[23] Suhartono, E.; Chen, S.-C.; Chang, Y.-H.; Chang, J.-A.; Lee, K. H. Improvement on the Surface Quality of Microcellular Injection Molded Parts Using Microcellular Co-Injection Molding with the Material Combinations of PP and PP-GF. *Int, J. Plast. Technol.* 2017, 21, 239–251.

[24] Guo, W.; Yang, Q.; Mao, H.; Meng, Z.; Hua, L.; He, B. A Combined In-Mold Decoration and Microcellular Injection Molding Method for Preparing Foamed Products with Improved Surface Appearance. *Polymers* 2019, 11, 778.

[25] Lee, J.; Turng, L.-S.; Peng, J.; Dougherty, E.; Gorton, P. The Effect of Polymer Additives on Surface Quality of Microcellular Injection Molded Parts. *Int. Polym. Process*. 2011, 26, 429–436.

[26] Wang, G.; Zhao, G.; Zhang, L.; Mu, Y.; Park, C. B. Lightweight and Tough Nanocellular PP/PTFE Nanocomposite Foams with Defect-Free Surfaces Obtained Using in Situ Nanofibrillation and Nanocellular Injection Molding. *Chem. Eng. J.* 2018, 350, 1–11.

[27] Mendoza-Cedeno, S.; Kweon, M. S.; Newby, S.; Shivokhin, M.; Pehlert, G.; Lee, P. C. Improved Cell Morphology and Surface Roughness in High-Temperature Foam Injection Molding Using a Long-Chain Branched Polypropylene. *Polymers* 2021, 13, 2404.

[28] Sugimoto, M. Control of Strain Hardening of Polymer Melts under Elongational Flow. *J. Soc. Rheol.* 2008, 36, 219–228.

[29] Weingart, N.; Raps, D.; Lu, M.; Endner, L.; Altstädt, V. Comparison of the Foamability of Linear and Long-Chain Branched Polypropylene—the Legend of Strain-Hardening as a Requirement for Good Foamability. *Polymers* 2020, 12, 725.

[30] Hou, J.; Zhao, G.; Wang, G. Polypropylene/Talc Foams with High Weight-Reduction and Improved Surface Quality Fabricated by Mold-Opening Microcellular Injection Molding. *J. Mater. Res. Technol.* 2021, 12, 74–86.

[31] Wang, L.; Hikima, Y.; Ishihara, S.; Ohshima, M. Fabrication of High Expansion Microcellular Injection-Molded Polypropylene Foams by Adding Long-Chain Branches. *Ind. Eng. Chem. Res*. 2016, 55, 11970–11982.

[32] Miyamoto, R.; Yasuhara, S.; Shikuma, H.; Ohshima, M. Preparation of Micro/Nanocellular Polypropylene Foam with Crystal Nucleating Agents. *Polym. Eng. Sci.* 2014, 54, 2075–2085.

[33] Wang, L.; Hikima, Y.; Ohshima, M.; Sekiguchi, T.; Yano, H. Evolution of Cellular Morphologies and Crystalline Structures in High-Expansion Isotactic Polypropylene/Cellulose Nanofiber Nanocomposite Foams. *RSC Adv.* 2018, 8, 15405–15416.

[34] Tseng, C.-H.; Tsai, P.-S. The Isothermal and Nonisothermal Crystallization Kinetics and Morphology of Solvent-Precipitated Nylon 66. *Polymers* 2022, 14, 442.

[35] Bu, H.; Cheng, S. Z. D.; Wunderlich, B. Addendum to the Thermal Properties of Polypropylene. *Makrornol. Chern., Rapid Comrnun*. 1988, 9, 75–77.

[36] Kobayashi, T.; Hashimoto, T. Development of Self-Assembling Nucleators for Highly Transparent Semi-Crystalline Polypropylene. *Bull. Chem. Soc. Jpn.* 2005, 78, 218–235.

[37] Ren, Q.; Wu, M.; Weng, Z.; Wang, L.; Zheng, W.; Hikima, Y.; Ohshima, M. Lightweight and Strong Gelling Agent-Reinforced Injection-Molded Polypropylene Composite Foams Fabricated Using Low-Pressure CO2 as the Foaming Agent. *J. CO_2 Util.* 2021, 48, 101530.

S3 Supporting Information

S3.1 Pressure and Temperature Profiles of the Injection Molded Polymer in the Mold Cavity

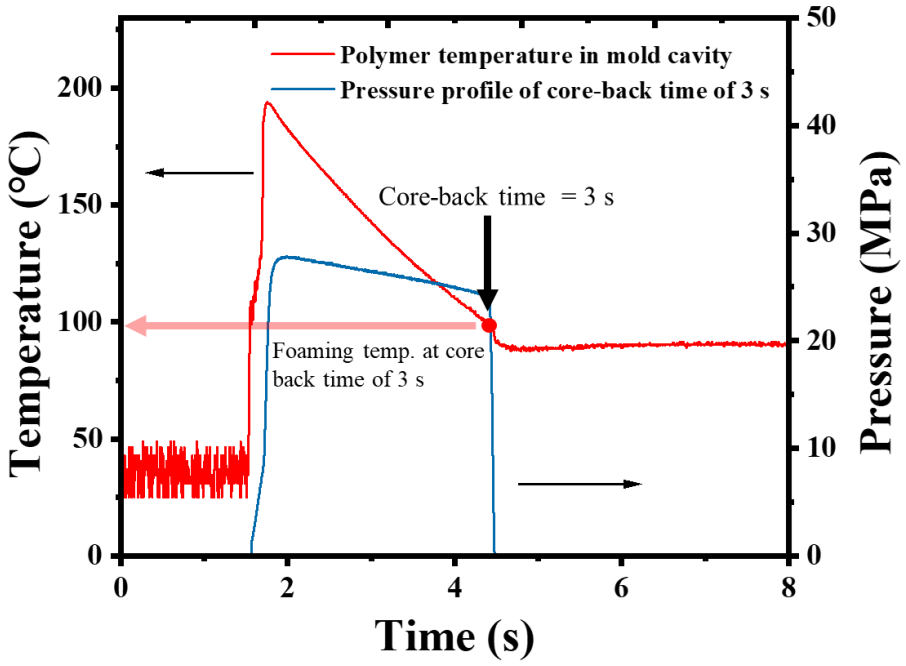

Figure 3.18 Pressure and temperature profiles of injection-molded polymer in mold cavity (FIM with core-back operation).

Two infrared temperature sensors and two pressure sensors were independently deployed in the rectangular-shaped mold cavity to measure the temperatures and pressures of the injection-molded polymer. The sensing locations in the mold cavity were: one close to the gate, and the other close to the cavity end, as shown in Figure 3.1. The profiles were recorded using a data acquisition device (Mold Marshaling system EPD-001, Futaba, Japan). By averaging the temperatures and pressures at two points of three injection cycles, the temperature and pressure profiles during an injection molding cycle were calculated and plotted against the processing time, as shown in Figure 3.18**.** As shown in Figure 3.18, the temperature exponentially decreases while the pressure increases and remains almost constant under holding (dwelling) operation. When the core-back operation is conducted at the end of the holding operation, the pressure of the polymer drastically decreases to atmospheric pressure. The core-back timing is equivalent to when the mold

part is opened at the end of the holding operation. The temperature at which the core-back operation is conducted is defined as the foaming temperature. The cooling rate of the injected polymer in the mold cavity was estimated to be -35 ^{o}C/s on average from Figure 3.18.

S3.2 Rheological Data

Figure 3.19 illustrates the strain-controlled dynamic frequency sweep measurements of complex viscosities and compares HPP, HPP/10%SIBS, HPP/20%SIBS, and HPP/30%SIBS. The experiments were conducted at 200 ^{o}C with 1% strain.

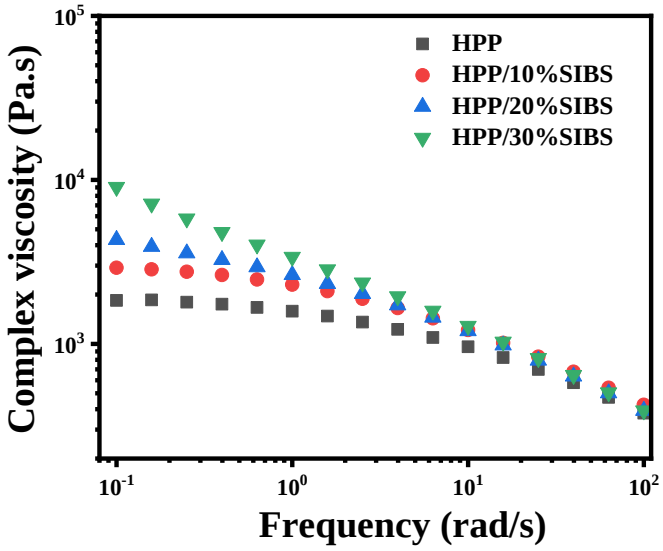

Figure 3.19 Frequency-sweep complex viscosity of HPP and HPP/SIBS blends.

Figure 3.20 shows the strain-controlled dynamic frequency sweep measurements of complex viscosities of four materials (HPP, HPP/20%LMPP, HPP/40%LMPP, and HPP/60%LMPP). A frequency sweep test was carried out by changing the shear rate frequency from 100 to 0.1 rad/s with 1% strain at a temperature of 200 ^{o}C.

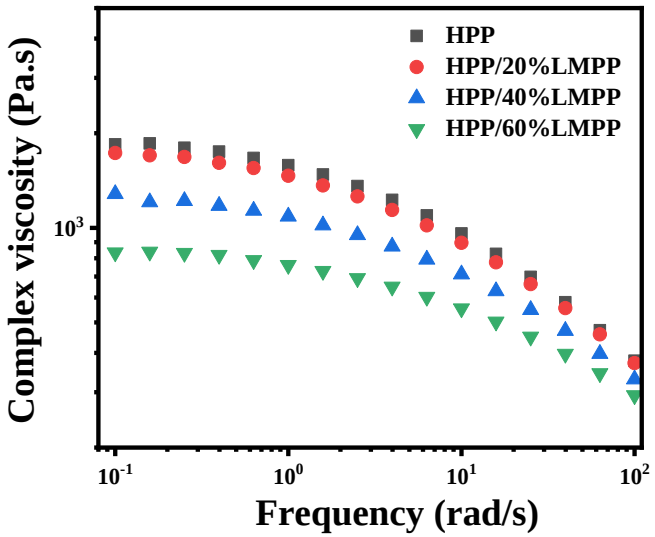

Figure 3.20 Frequency-sweep complex viscosity of HPP and HPP/LMPP blends.

Figure 3.21 depicts the strain-controlled dynamic frequency sweep measurements of complex viscosities and compares HPP, HPP/30%LMPP, HPP/0.3%MD, and HPP/30%LMPP/0.3%MD. The experiments were conducted at 200 ^{o}C and 170 ^{o}C with 1% strain.

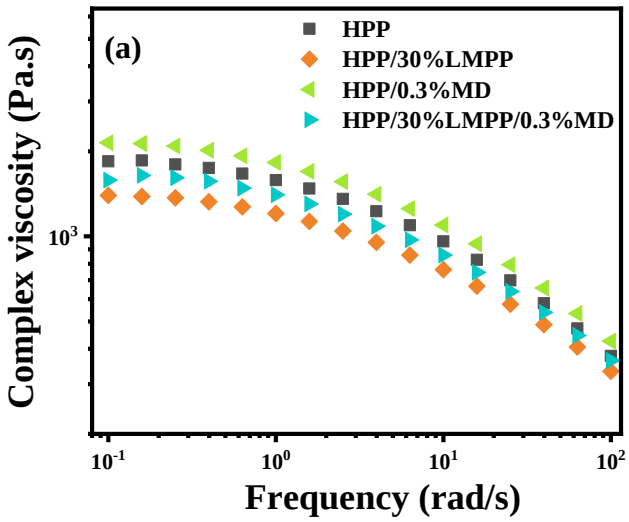

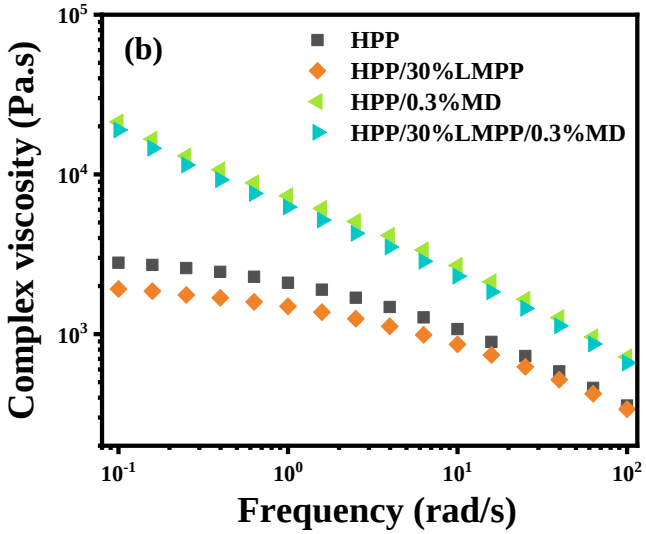

Figure 3.21 Frequency-sweep complex viscosity of HPP, HPP/MD and HPP/LMPP/MD blends at (a) 200 °C and (b) 170 °C.

S3.3 Crystallization Kinetics of HPP/SIBS Blends at Low Cooling Rate

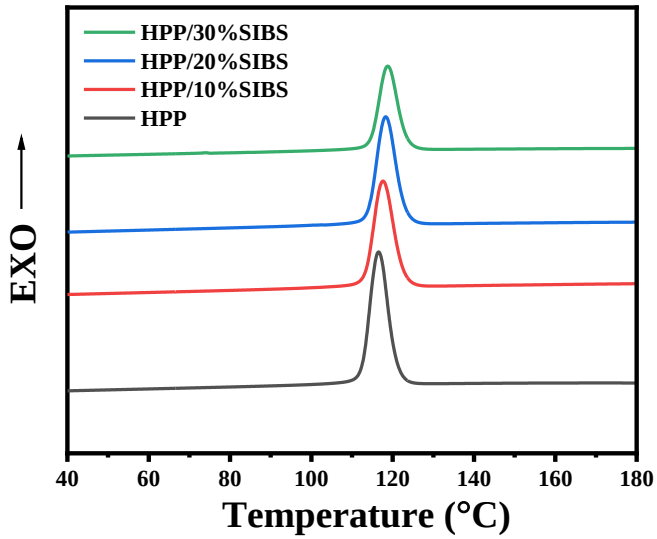

Figure 3.22 Cooling curves of HPP and HPP/LMPP blends measured at a cooling rate of -10 °C/min.

Table 3.4 Crystallinity of HPP in different HPP/SIBS blends at a cooling rate of -10 ºC/min

Parameters	HPP	HPP/10% SIBS	HPP/20% SIBS	HPP/30% SIBS
Crystallinity [%]	45.41	35.43	30.11	19.51

S3.4 Effect of MD on the Surface Roughness

Figure 3.23 shows the *Sa* of the foamed injection molded HPP with two different contents of MD. Adding MD could improve surface quality.

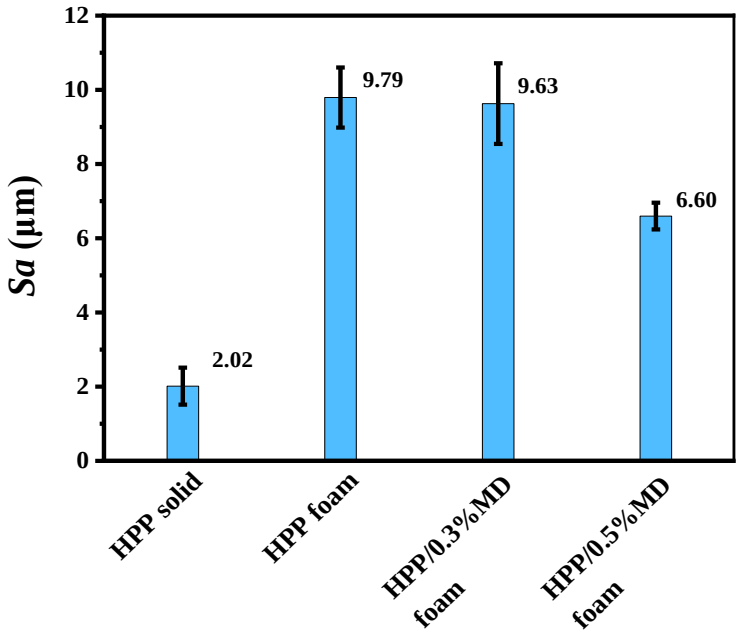

Figure 3.23 Surface roughness (*Sa*) of HPP solid, HPP foam, HPP/MD (0.3 wt.%) foam and HPP/MD (0.5wt.%) foam.

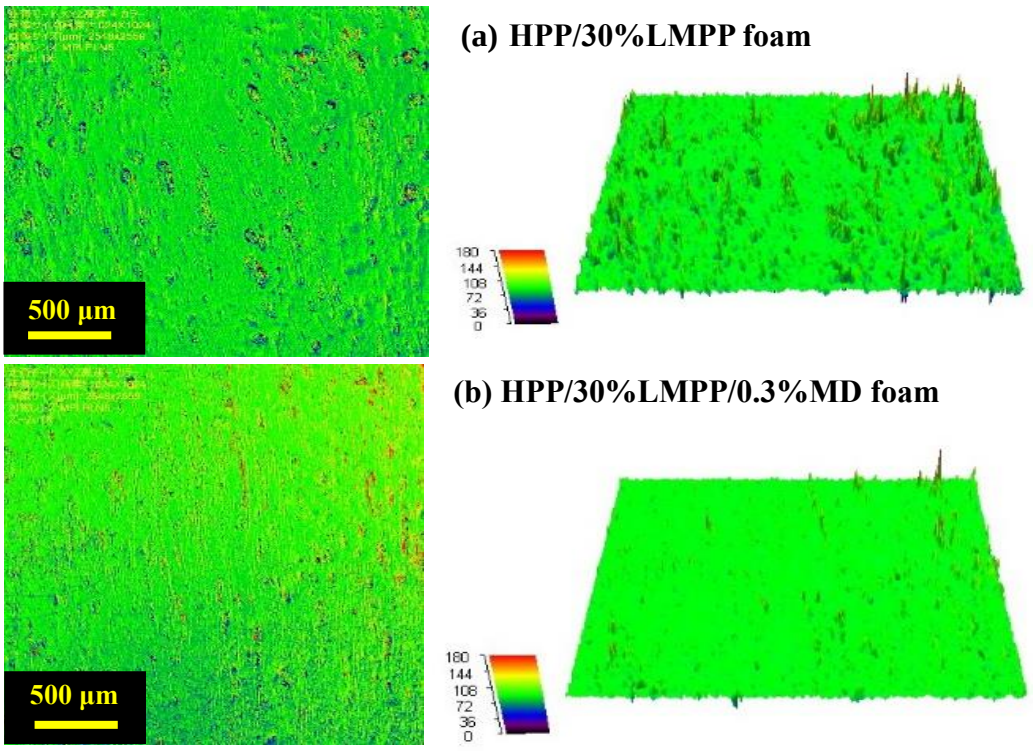

Figure 3.24 Two-dimensional(2D) and Three-dimensional (3D) laser microscope images of injection-molded parts: (a) HPP/30% LMPP foam, (b) HPP/30% LMPP/0.3%MD foam (2D: λ_c = 2500 µm and λ_s = 0 µm) and (3D: λ_c = 2500 µm and λ_s = 30 µm).

Figure 3.24 shows the 2D and 3D microscope images of HPP/30 %LMPP and HPP/30% LMPP/0.3% MD foams. When comparing the image of both foams, the efficacy of MD on the surface roughness can be clarified.

S3.5 Effect of SIBS on Mechanical Property of Blends (Solid)

Figure 3.25 shows the tensile test data of non-foamed samples of HPP, HPP/SIBS blends. The tensile test was conducted at a 10 mm/min stretching rate. The dumbbell-shaped specimens with a gauge length of 20 mm and 1mm in thickness were prepared by cutting out the non-foamed injection molded products using the SD Level Sample Cutting Machine (SDL-100, Dumbbell Co., Ltd., Japan).

Figure 3.26 shows the Young's modulus and yield stress calculated from the strain-stress curves in Figure 3.25. The Young's modulus and yield stress were decreased with the increased SIBS content. Although the complex viscosity was increased with increased blend ratio of SIBS, the reduction in the Young's modulus and yield stress softness could contributed to decrease in crystallinity of PP, according to Figure 3.22.

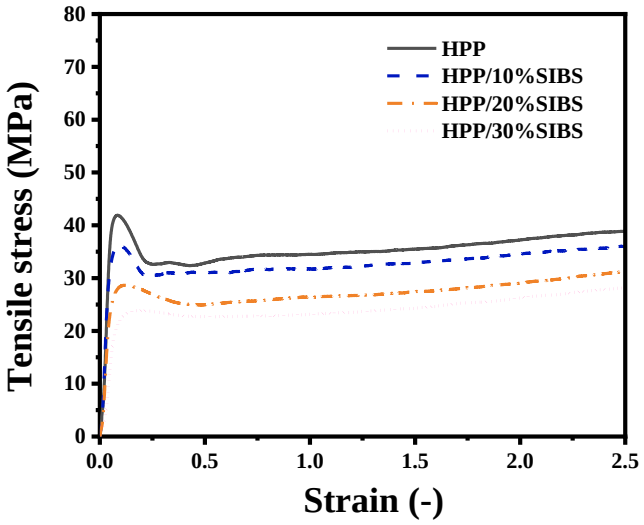

Figure 3.25 Tensile test data of HPP, HPP/SIBS with different blend ratios (non-foamed samples).

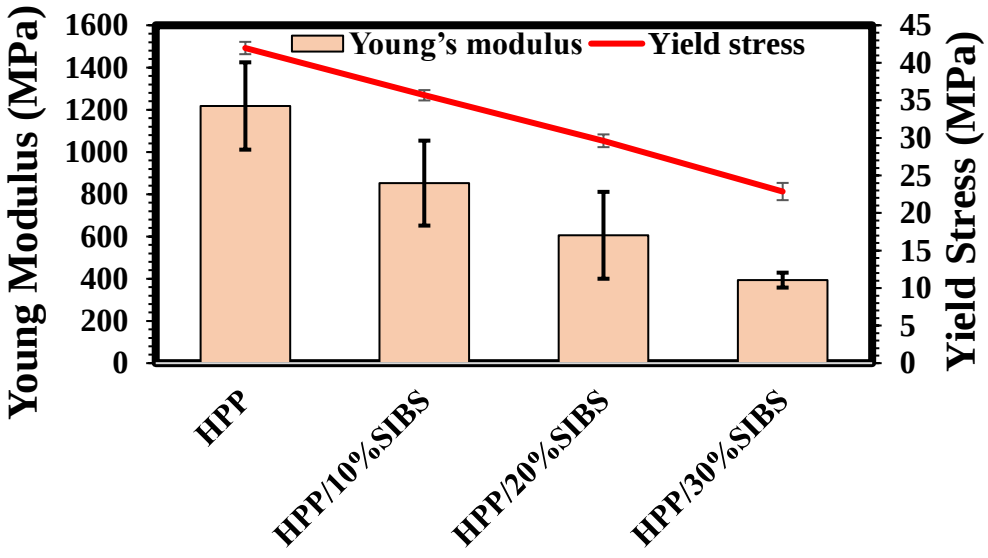

Figure 3.26 Young's modulus and yield stress of HPP, HPP/SIBS with different blend ratios, (non-foamed samples).

S3.6 Effect of LMPP and MD on Mechanical Property of Blends (Solid)

Figure 3.27 shows the tensile test data of HPP, HPP/LMPP with different blend ratios, HPP/0.3%MD, HPP/30%LMPP/0.3% MD. The tensile test was conducted using a tensile tester (Autograph AGS-1kN, Shimazu, Japan) at a 10 mm/min stretching rate. The dumbbell-shaped specimens with a gauge length of 20 mm and 1mm in thickness were also prepared by cutting out the non-foamed injection molded products using the SD Level Sample Cutting Machine (SDL-100, Dumbbell Co., Ltd., Japan).

Figure 3.28 shows the Young's modulus and yield stress calculated from the strain-stress curves in Figure 3.27. As predicted from the complex viscosity data in Figure 3.3, the Young's modulus and yield stress were decreased with the increased LMPP content, which can be predicted by crystallization retarding effect of LMPP. The softness caused by LMPP can contribute to the reduction of surface roughness, but it will lead the bubbles to grow faster and produce large-size cells in their foam unless the foaming temperature is lowered.

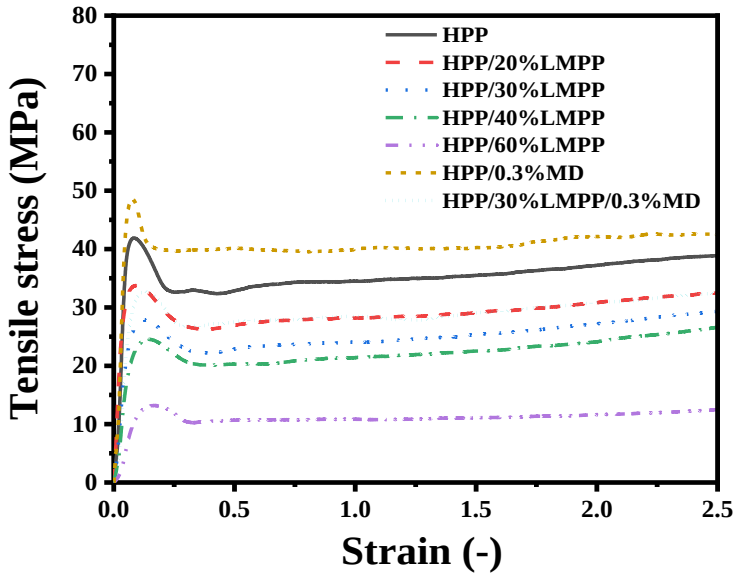

Figure 3.27 Tensile test data of HPP, HPP/LMPP with different blend ratios, HPP/0.3%MD, HPP/30%LMPP/0.3% MD (non-foamed samples).

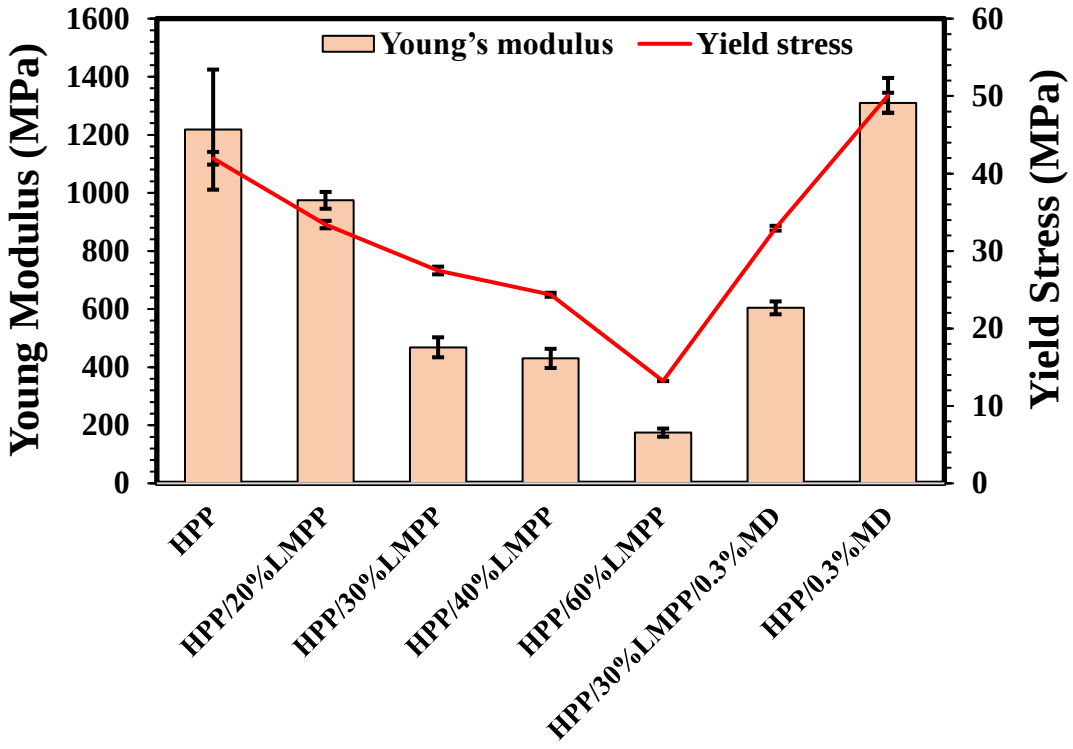

Figure 3.28 Young's modulus and yield stress of HPP, HPP/LMPP with different blend ratios, HPP/0.3%MD, HPP/30%LMPP/0.3% MD (non-foamed samples).

S3.7 Effect of SIBS on Mechanical Property of Foams

The compression tests of HPP/SIBS blends were also conducted with the same autograph to evaluate the mechanical property of the foams. For the compression tests, rectangular samples were prepared from the foams and the compression speed was set to 1 mm/min. The results are shown in Figure 3.29. The compressive modulus of the HPP foams had similar value to that of HPP/10%SIBS. As SIBS content increased, the compressive modulus became lower.

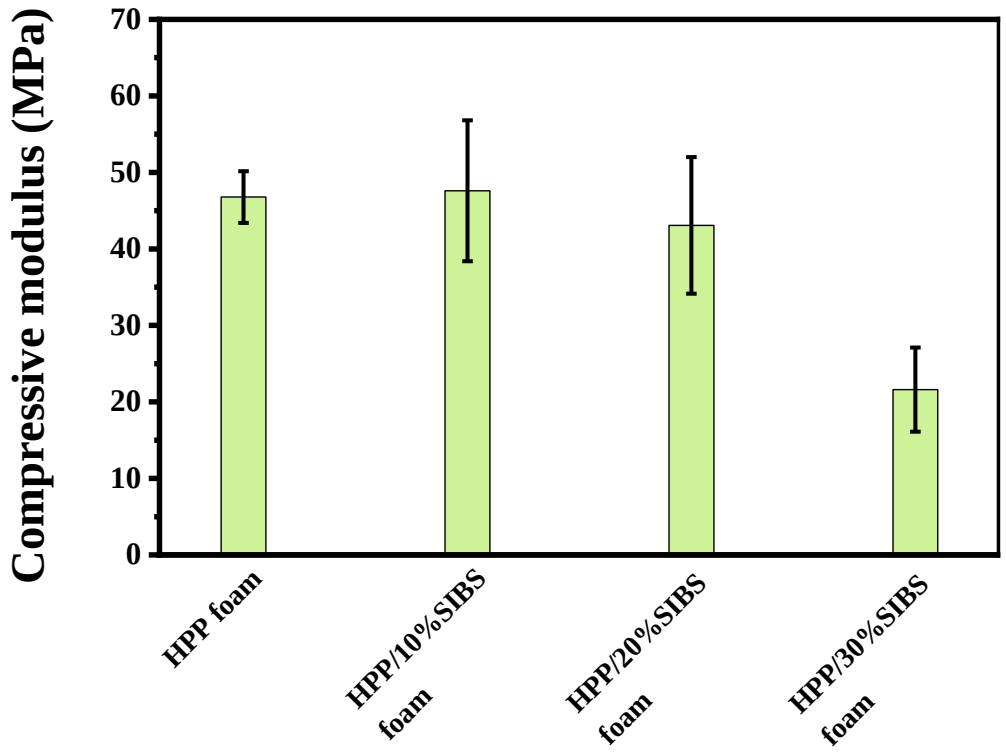

Figure 3.29 Compression modulus of the HPP foam, HPP/SIBS blends' foams.

S3.8 Effect of LMPP and MD on Mechanical Property of Foams

The compression test was conducted with the same autograph to evaluate the mechanical property of the foams. For the compression tests, rectangular samples were prepared from the foams and the compression speed was set to 1 mm/min. The results are shown in Figure 3.30. The compressive modulus of the foams was decreased with the increase in LMPP content up to 40%. However, the foams' mechanical properties depend on the cell morphology. The cell morphology could be controlled by manipulating the core-back time and the degree of expansion ratio. By delaying core-back time, the foaming temperature in the core part of the injected polymer was lowered, and the viscosity of the polymer was increased. As a result, the cell size became smaller, and the compression modulus increased. HPP/60%LMPP was inflated like a balloon at a temperature of about 100 ^{o}C (i.e., core-back time = 3 s). Nevertheless, microcellular foam could be prepared by lowering the foaming temperature from about 100 to 80 ^{o}C. Since the cell size of the HPP/60% LMPP foam was decreased, the compressive modulus of the HPP/60%LMPP became higher than that of HPP/40%LMPP.

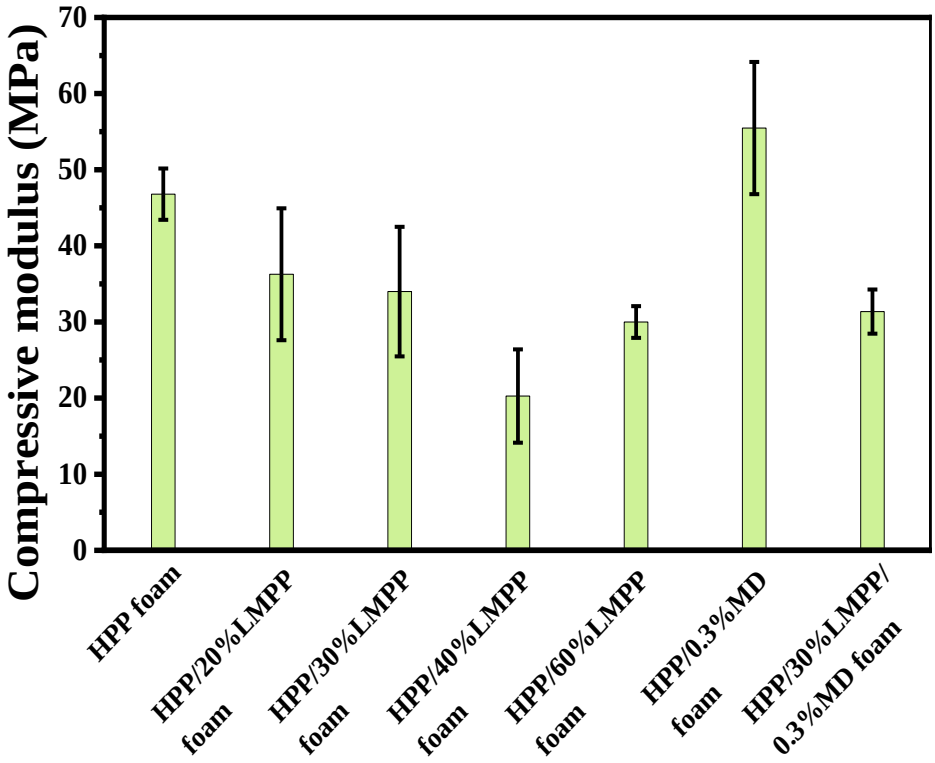

Figure 3.30 Compression modulus of the HPP foam, HPP/LMPP blends' foams, HPP/LMPP with MD foam.

S3.9 Effect of LMPP on Cell Morphology

Figure 3.31 illustrates the SEM images of the cell morphology of the five-hold expanded foams. Each figure's left-side image was a cross-sectional area near a skin layer of the foam, taken from a view parallel to the core-back direction, i.e., foam thickness direction. The right-side image was a cross-sectional area of the foam core, taken from a view perpendicular to the core-back direction. The dotted circle indicates the presence of elongated bubbles on the surface.

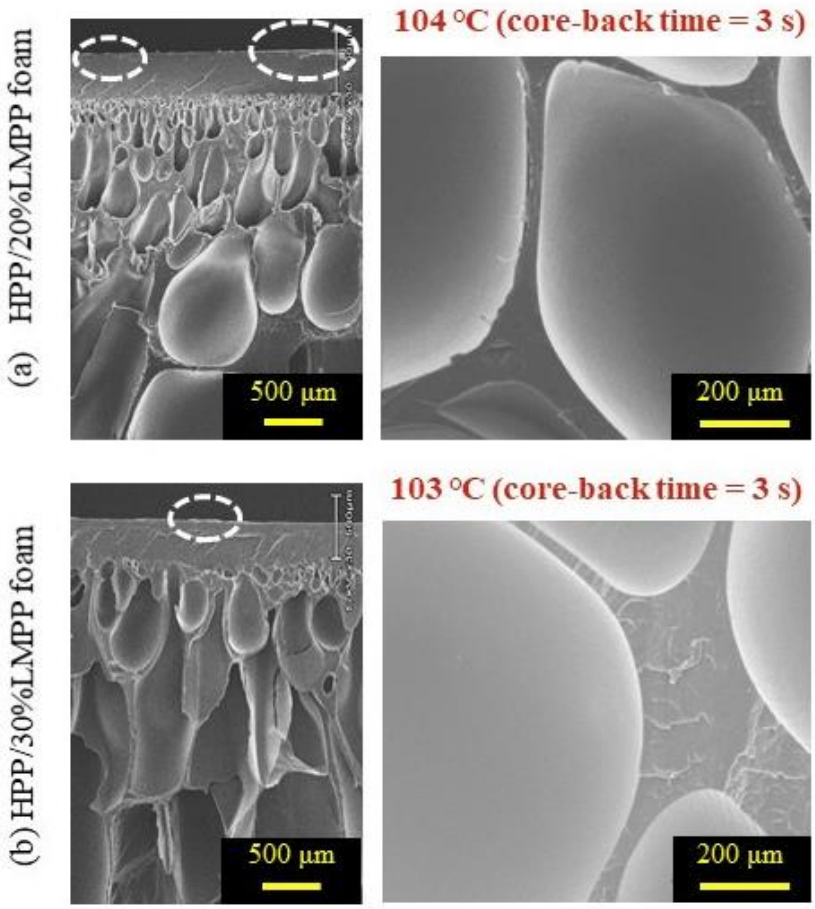

Figure 3.31 SEM images of cell morphology: (a) HPP/20%LMPP foams and (b) HPP/30%LMPP foams of five-fold expansion. Left: a cross-sectional image taken parallel to the core-back direction (thickness direction); Right: a cross-sectional image taken perpendicular to the core-back direction.

S3.10 Effect of the Concentration of Physical Blowing Agent (PBA)

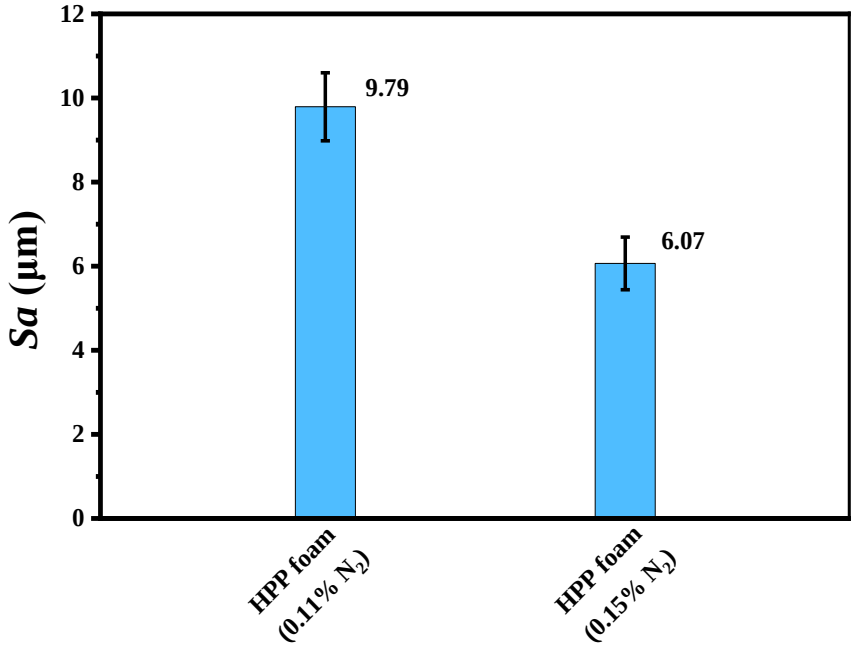

Figure 3.32 Surface roughness (*Sa*) of HPP foam with N_2 concentration of 0.11 % and 0.15 %.

Figure 3.32 shows HPP foam's surface roughness (*Sa*) with different N_2 concentrations. We conducted the foaming experiments with a higher N_2 concentration, 0.15%. *Sa* of the resulting foams was better than that of the foam produced with 0.11% N_2. When the physical blowing agent (PBA) increased, the bubble nucleation was enhanced, the number of bubbles increased, and the cell size decreased. Then, the surface quality was improved by increasing the concentration of PBA.

However, when the concentration of the PBA exceeds a certain level where the PBA cannot be dissolved entirely in polymer, or it produces so many bubbles to easily coalesce with each other, large-size bubbles and swirl mark would appear on the skin layer, which deteriorates the surface appearance. Thus, it can be said that increasing PBA concentration can improve the surface quality as far as the cell size is reduced.

Chapter 4 Stretching-Induced Foaming of Gas-Laden Thermoplastic Elastomers (TPEs)

4.1 Introduction

Based on the description in Chapter 2, SIBS-based microcellular foams have been successfully prepared by incorporating foam injection molding and core-back operation with high pressure N_2. However, to the author's knowledge, SIBS foaming with low pressure of blowing agent is difficult. In order to prepare SIBS foam with low pressure of gas (e.g. CO_2), a method of stretching-induced foaming has been proposed. By using foam injection molding, gas-laden SIBS parts with low pressure of CO_2 were prepared, and stretching-induced foaming of gas-laden SIBS was successfully conducted. Different pressures, stretching rates (strain rates) and strains were studied. Here, we introduced stretching rate-dependent elastic strain energy to the theory of bubble nucleation. Based on both theoretical background and experimental data, stretched SIBS foam of higher bubble density and smaller bubble size were obtained with higher pressure, higher stretching rate and higher strain. In addition, the theory described in this paper clarified the difference in bubble nucleation barrier between two kinds of SIBS.

Generally speaking, microcellular polymer foaming technology can be divided into chemical and physical foaming in practice, to achieve desired foam performances. Whereas sustainable development and environmental-friendly life has been the mainstreams in today's society, physical foaming with green and harmless blowing agent has been drawing more attentions academically and industrially than chemical foaming. Although there are a variety of approaches to prepare polymer foams, the procedure can be simply concluded: formation of polymer/gas mixture, bubble nucleation caused by thermodynamic instability (pressure drop or temperature increase), subsequent bubble growth and foam structure stabilization.

It is well known that critical phenomena of physical foaming include bubble nucleation and growth, which significantly affect the cell (bubble) structure (bubble density and bubble diameter) of the foams. Several models simulating bubble nucleation and growth phenomena were proposed based on classic nucleation theory (CNT).[1-2] However, the classic nucleation theory alone describes a thermodynamic process, which does not reflect the polymer nature, such as

viscoelasticity and fluidity. It has not been sufficient to explain bubble nucleation in polymers, which creates a significant challenge for foaming researchers to consolidate and advance polymer-foaming technology. Considering the effect of shear stress, Han and Han studied bubble nucleation in a shear flow field.[3] They pointed out that bubble nucleation could be promoted by shear flow under unsaturation conditions with a physical blowing agent or flow of the material. Lee reported a modified cavity model to understand the enhancement effect of shear on bubble nucleation.[4-5] He mentioned that shear was not only the dominant factor and that the melt temperature of the polymer also had a substantial impact on bubble nucleation. Based on the energy transformation from mechanical shear energy to surface energy, Chen and co-workers[6] explained that the shear stress promotes bubble nucleation. Guo and Peng[7] investigated the shear nucleation theory in microcellular foam extrusion processes. They elucidated that shear effects acted as a main driving force for bubble nucleation compared with the supersaturation in the microcellular foam extrusion. To further investigate the influence of shear or extensional stress, many efforts have been done by Wong et al.,[8-11] and a visualization system has been employed for observation of batch foaming process in a view cell under shear or extensional stress. They concluded that shear or extensional stress played an essential role in enhancing bubble nucleation, and the reduction in local pressure induced by tensile stress could benefit bubble nucleation. In contrast, the increase in local pressure induced by compressive stress could hinder bubble nucleation. Wang et. al.[12] identified the effect of elastic strain energy on bubble nucleation and successfully prepared submicrocellular TPU microfilms by stretching and compressing the samples before foaming. Their results showed that both compression and stretching were beneficial for enhancing bubble nucleation, but compression alone was not as effective as stretching because the energy barrier increased under compression. They proposed a bubble nucleation model in their supporting information, which augmented the elastic strain energy in the bubble nucleation rate equation to qualitatively explain the strain's effect on cell density. The effect of extensional stress on the bubble nucleation rate is needed to investigate the pressure or temperature quenching effect independently. Our previous work also introduced an elastic strain energy function to the Gibbs free energy of the classical nucleation rate equation to reflect the elastic nature of the polymer.[13] The modified equation can apply to nanocellular foam and engineering plastic foam, where the elasticity of the polymer is high. However, it still has an ambiguity in the definition of the initial size of the bubble embryo and difficulty in dealing with the shear or strain rates.

This work used a kind of thermoplastic elastomer (TPE), styrene-isobutylene-styrene block copolymer (SIBS), as a base polymer. The elastic nature of SIBS provides uniform elongational deformation when it is stretched. Nonfoamed CO_2-laden SIBS was prepared by a foam injection molding machine with low gas delivery pressure and subsequently stretched by a tensile tester. Changing the strain and stretching rate of the tensile tester, the gas-laden SIBS was stretched, and the effects of stretching degree and rate, i.e., elastic strain energy and stretching rate, on bubble nucleation rate were investigated to separate the effects of pressure and temperature quenching. A bubble nucleation model including the elastic energy and stretching rate is proposed from the stretching-induced foaming cell structure.

4.2 Experimental Section

4.2.1 Materials

Two grades of styrene-isobutylene-styrene block copolymer (SIBS073T and SIBS062M, Kaneka, Osaka, Japan) were used as is. The melt flow rate, the number-average molecular weight, $\bar{M}_n$, and the weight-average molecular weight, $\bar{M}_W$, of SIBS073T are 6.0 g/10 min (230 ℃/2.16 kg), 58,000 and 81,000, respectively. Those of SIBS062M are 20.0 g/10 min (230 ℃/2.16 kg), 39,000 and 65,000, respectively. Carbon dioxide (CO_2) of 99% purity (Izumi Sanyo, Tokyo, Japan) was utilized as a physical blowing agent (PBA).

4.2.2 Sample Preparation and Foaming Process

A foam injection molding (FIM) machine that does not need a high-pressure pumping system was employed to prepare the gas-laden TPE without foaming the product. Further details of the FIM can be found in our previous works.[14-15] The FIM machine is a 35-ton clamping force electric injection molding machine, whose screw was 22 mm in diameter (J35AD-AD30H, Japan Steel Work, Ltd. Japan). The mold has a rectangular cavity with dimensions of 40 mm × 10 mm × 2 mm. The cylinder temperatures were set as 40, 120, 180, 200, 200, 200, 200, and 200 ℃ from the feeding zone to the nozzle zone. The experimental conditions are summarized in Table 1 below.

Table 4.1 Experimental conditions for the low-pressure injection molding machine.

Parameters	Values
Blowing agent	CO_2
Gas pressure (MPa)	2, 3, 4, 5
Cylinder temperature (℃)	40, 120, 180, 200, 200, 200, 200,200
Mold temperature (℃)	30
Holding pressure (MPa)	30
Injection speed (mm/s)	20
Dwelling time (s)	6

Gas delivery pressure was kept below 5 MPa, to prevent the gas-laden samples from foaming in the injection molding process. After ejection of a nonfoamed but gas-laden molded sample, the sample was fixed to and stretched by a universal testing machine (Autograph AGS-1kN, Shimazu, Japan). Before fixing the sample to the tensile tester, the weight of the sample was measured, and its spur was cut out. Uniaxial stretching was conducted at different stretching rates of 50, 100, 200, and 400 mm/min. The final strain was also changed to three levels, 100, 200 and 300%.

4.2.3 Foam Structure Characterization

The cell structure, e.g. bubble density and bubble size, of the stretching-induced foams was evaluated using a scanning electron microscope (Tiny-SEM Mighty-8, Technex, Tokyo, Japan). A small slice specimen was cut from the center of the stretching-induced foam and cryogenically fractured in liquid nitrogen. The cross-sectional area was gold-coated using a quick coater (VPS-020, ULVAC KIKO, Ltd., Japan). Then, SEM images were analyzed using ImageJ (National Institutes of Health, USA). The number-average bubble diameter was calculated by Eq. (4-1):[16-17]

$$d = \frac{\Sigma d_i n_i}{\Sigma n_i} \qquad (4\text{-}1)$$

where n_i is the number of bubbles with a diameter of d_i. The bubble shape is assumed to be spherical. The bubble density (N_0) was calculated by Eq. (4-2):[15,17]

$$N_0 = \left(\frac{n}{A}\right)^{\frac{3}{2}} \qquad (4\text{-}2)$$

where n represents the total number of bubbles in the chosen area of the SEM image and A is the selected area.

4.3 Stretching Rate-Dependent Energy Barrier of Bubble Nucleation

4.3.1 Model

According to classical nucleation theory described in Section 1.2 of Chapter 1, bubble nucleation in polymer foaming was expressed by Eq. (4-3), comprising of the volume energy difference and surface energy difference energy[1-2]:

$$\Delta G = -\frac{4\pi}{3}R^3\left(P_{bubble} - P_{sys}\right) + 4\pi R^2\gamma \qquad (4\text{-}3)$$

where P_{bubble} and P_{sys} are the pressures in the bubble nucleus and in the system respectively. γ is the surface tension between gas and liquid.

However, the classical nucleation theory cannot be fully accepted in the polymer foaming process due to the polymer's viscoelastic nature. Referring to a theory of stretching-induced craze formation of the polymer, Wang et al.[12] introduced elastic strain energy barrier densities, Δg_{eb} and Δg_{st}, into the Gibbs free energy:

$$\Delta G = -\frac{4\pi}{3}R^3\left[\left(P_{bubble} - P_{sys}\right) - \Delta g_{eb} + \Delta g_{st}\right] + 4\pi R^2\gamma \qquad (4\text{-}4)$$

$$\Delta g_{st} = \Delta g_h + \Delta g_d \qquad (4\text{-}5)$$

Δg_{eb} denotes the critical distortion energy density and Δg_{st} is the total elastic strain energy density, which is further divided into the dilatational energy density, Δg_h, and distortional energy density, Δg_d, The continuum mechanism[18-19] and the von Mises theory[20-27] give those energy densities as a function of Poisson's ratio, v, the elastic modulus, E, the dilatational stress, σ_h, von

Mises stress, σ_{vm}, the stress at yield, σ_e, yield stress, σ_y and dimensionless constant, μ. The details of those functions are given by Eqs. (4-21) – (4-24) in the Supporting Information.

The homogenous bubble nucleation activation energy barrier for tensile stress was given by Eq. (4-6):

$$\Delta G_{hom}^{*} = \frac{16\pi\gamma^3}{3\left[\left(P_{bubble} - P_{\text{sys}}\right) + \Delta g_{st} - \Delta g_{eb}\right]^2} \tag{4-6}$$

If considering the presence of the nucleating agent, the heterogenous bubble nucleation activation energy barrier ΔG_{het}^{*} can be formulated by adding a term $F(\theta, \beta)$, which can be found in similar form as Eq. (1-4) in Chapter 1.

The homogenous bubble nucleation energy barrier became a function of Δg_{st} and Δg_{eb} in addition to the degree of supersaturation, $P_{bubble} - P_{\text{sys}}$, and surface tension, γ. Based on these Eqs. (4-4) – (4-6), Wang et al. qualitatively explained why stretching or compressing the polymers before batch physical foaming could enhance bubble nucleation. However, they did not consider the effect of the stretching rate (strain rate) on the dilatational and distortional energy densities.

In this chapter, we considered the strain rate (in s^{-1}) dependency when formulating both energy densities, Δg_{st} and Δg_{eb}, based on the yield criterion that Yu et al. proposed.[28-29] They developed a strain rate-dependent yield criterion, starting the following constitutive equation of a linear elastic stage of orthotropic materials. Using rectangular Cartesian coordinates with principal stress (σ_1, σ_2, σ_3) and strain (ε_1, ε_2, ε_3), they described the strain rate-dependent yield criterion. When considering the uniaxial loading (stretching or compressing) direction (axis-1), they derived the distortional strain energy density, u_d, and the total strain energy density, u_ϵ, with strain, ε_1 and strain rate, $\dot{\varepsilon}_1$, as follows:

$$u_d = A_1\varepsilon_1^2 + A_2\varepsilon_1\dot{\varepsilon}_1^n \tag{4-7}$$

$$u_\epsilon = \frac{1}{2}B_1\varepsilon_1^2 + \frac{1}{2}B_2\varepsilon_1\dot{\varepsilon}_1^n \tag{4-8}$$

where A_1, A_2, B_1, and B_2 are defined by:

$$A_1 = \frac{1}{2}(k_{11} - v_{21}k_{12} - v_{31}k_{13}) - \frac{1}{18}\sum_{i,j=1}^{3} k_{ij}\,(1 - v_{21} - v_{31})^2 \quad (4\text{-}9)$$

$$A_2 = \frac{1}{2}(f_{11} + (-v_{21})^n f_{12} + (-v_{31})^n f_{13}) - \frac{1}{2}\cdot\frac{1}{3^{n+1}}\sum_{i,j=1}^{3} f_{ij}\,(1 - v_{21} - v_{31})^{n+1} \quad (4\text{-}10)$$

$$B_1 = k_{11} - v_{21}k_{12} - v_{31}k_{13} \quad (4\text{-}11)$$

$$B_2 = f_{11} + (-v_{21})^n f_{12} + (-v_{31})^n f_{13} \quad (4\text{-}12)$$

where v_{ij} are Poisson's ratios. k_{ij} are the elastic stiffness coefficients in the constitutive equation, relating between strain and stress by Hooke's law.[28-29] f_{ij} are the coefficients, expressing the relationship between the stress and strain rate. The constitutive equation is denoted by Eq. (4-25) in the Supporting Information, and the matrices are shown in Eq. (4-26).

Then, they gave a yield criterion as a relationship between the critical distortional energy density, u_{ds}, and the distortional energy density, u_d.

$$u_d \le u_{ds} = \frac{1+v}{3E}\sigma_y^2 \quad (4\text{-}13)$$

Assuming the critical distortional energy density governs the yield, the relationship among the critical distortional energy density, u_{ds}, yield stress, σ_y and yield strain, $\varepsilon_{y,}$ was derived using Eqs. (4-14) – (4-15) as:

$$u_{ds} = A_1\varepsilon_y^2 + A_2\varepsilon_y\dot{\varepsilon}_1^n \quad (4\text{-}14)$$

$$\sigma_y = B_1\varepsilon_y + B_2\dot{\varepsilon}_1^n \quad (4\text{-}15)$$

We used their critical distortional energy density, u_{ds}, (Eq. (4-14)) as Δg_{eb} and their total strain energy desnity, u_ϵ (Eq. (4-8)) as Δg_{st} in the Gibbs free energy of the bubble nucleation (Eq. (4-6)), i.e.

$$\Delta g_{eb} = A_1\varepsilon_y^2 + A_2\varepsilon_y\dot{\varepsilon}_1^n \quad (4\text{-}16)$$

$$\Delta g_{st} = \frac{1}{2}B_1\varepsilon_1^2 + \frac{1}{2}B_2\varepsilon_1\dot{\varepsilon}_1^n \quad (4\text{-}17)$$

Substituting Eqs. (4-16) and (4-17) into Eq. (4-6) gives the homogenous nucleation energy barrier under tensile stress in combination with the strain rate:

$$\Delta G^*_{hom} = \frac{16\pi\gamma^3}{3\left[\left(P_{bubble} - P_{\mathrm{sys}}\right) + \frac{1}{2}B_1\varepsilon_1^2 + \frac{1}{2}B_2\varepsilon_1\dot{\varepsilon}_1^n - \left(A_1\varepsilon_y^2 + A_2\varepsilon_y\dot{\varepsilon}_1^n\right)\right]^2} \quad (4\text{-}18)$$

To use Eq. (4-18), A_1, A_2, B_1, B_2 and n must be identified. In this study, Poisson's ratio ν_{ij} is assumed to be strain rate-independent[30] and equal in value for all directions, i.e., $\nu_{ij} = \nu$ (constant). It was assumed to be 0.49 (SIBS is a type of elastomer whose Poisson's ratio is generally close to 0.5). To determine these parameter values, one-directional stretching tests with various stretching rates (in mm/min) were needed.

4.3.2 Tensile Test for Determining Energy Density Parameters

Tensile tests with various stretching rates were performed, including one quasi-static test (1 mm/min) and four dynamic tests (50, 100, 200, and 400 mm/min). First, a yield point $(\varepsilon_y, \sigma_y)$ was determined from the one quasi-static test result. The critical distortional energy density, u_{ds}, was determined by Eq. (4-13) with the obtained σ_y and E. Then, A_1 was calculated using Eq. (4-14) with ε_y, assuming that the strain rate, $\dot{\varepsilon}_1$, was regarded as zero for the quasi-static test data. Then, A_2 was determined by transforming Eq. (4-14) into Eq. (4-19) using other dynamic test data with the calculated A_1 value.

$$\log\left(\frac{u_{ds}}{\varepsilon_y} - A_1\varepsilon_y\right) = \log(A_2\dot{\varepsilon}_1^n) = \log(A_2) + n\log(\dot{\varepsilon}_1) \quad (4\text{-}19)$$

Similarly, B_1, was determined by Eq. (4-15) using ε_y and σ_y of quasi-static test data. Then, B_2, was determined by transforming Eq. (4-15) into Eq. (4-20) and using more than four sets of data of ε_y, σ_y and constant strain rate, $\dot{\varepsilon}_1$.

$$\log(\sigma_y - B_1\varepsilon_y) = \log(B_2\dot{\varepsilon}_1^n) = \log(B_2) + n\log(\dot{\varepsilon}_1) \quad (4\text{-}20)$$

Another method of determining A_1 and B_1 values with Poisson's ratio and the elastic modulus, E, which Yu et al.[28] proposed, was summarized and performed in the Supporting Information.

4.4 Results and Discussion

4.4.1 Tensile Test Data and Parameter Values

Figure 4.1 shows strain–stress curves of quasi-static and dynamic tests of solid samples of SIBS073T and SIBS062M, respectively. These results demonstrated an increase in the yield stress with increasing stretching rate.

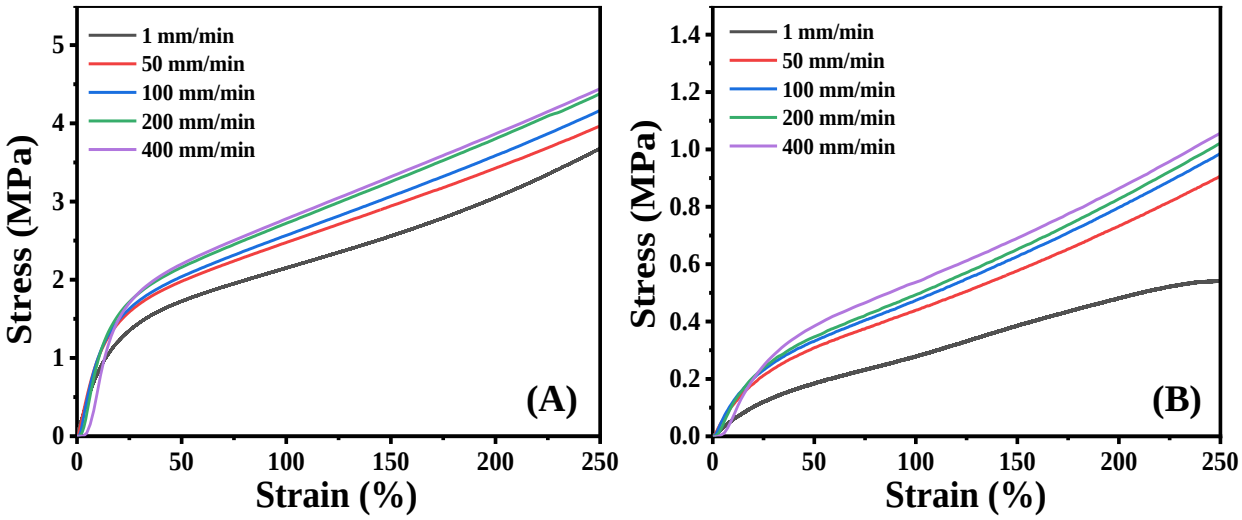

Figure 4.1 Strain–stress curves of quasi-static and dynamic tests of solid samples (A) SIBS073T and (B) SIBS062M.

Figure 4.2 shows how to obtain ε_y and σ_y from a strain–stress (S–S) curve of the tensile test. The black dashed line was drawn as a slope of the linear part of the strain–stress curve. Then, the dashed line was shifted to a 0.2% strain offset called the 0.2% offset method,[31-32] and intersected with the S-S curve. The crossover point is regarded as the yield point. As a consequence, ε_y and σ_y were obtained. The 0.2% strain offset method is generally used to determine the yield point when elastic region and plastic region of polymer are difficult to distinguish. The reason for choosing 0.2% of strain is that, it is easily and simply measurable while exact enough for most engineering purposes. The parameter values of A_1, A_2, B_1, B_2 and n were determined by following the procedure described in the previous section as listed in Table 4.2.

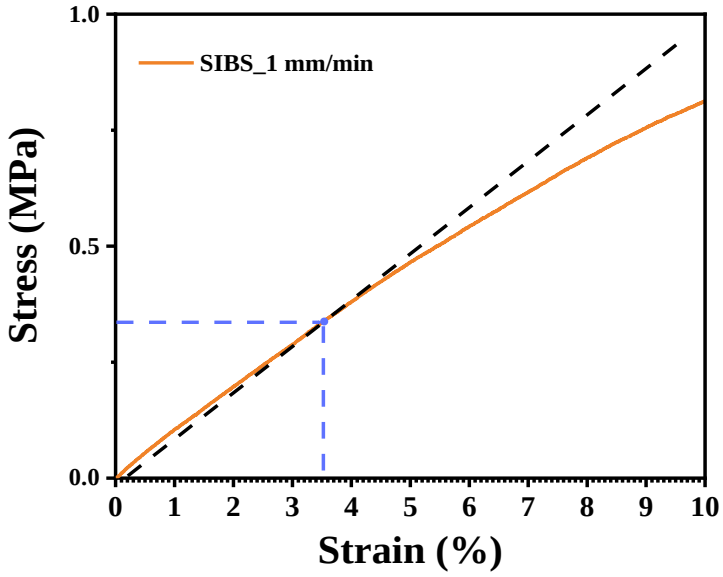

Figure 4.2 Scheme of determining ε_y and σ_y from S–S curve.

Table 4.2 Estimated parameters based on quasi-static and dynamic tensile tests of different grades of SIBS.

Parameters	SIBS073T	SIBS062M
A_1 (MPa)	4.76	0.37
A_2 (MPa·s^n)	-4.34×10^{-1}	-6.59×10^{-2}
B_1 (MPa)	9.56	0.74
B_2 (MPa·s^n)	5.50×10^{-1}	1.39×10^{-1}
Δg_{eb} in quasi-static test (MPa)	6.17×10^{-3}	1.70×10^{-4}
n	0.47	0.57
Poisson's ratio (assumed)	0.49	0.49

4.4.2 Stretching-Induced Foaming

Figure 4.3 shows a series of snapshots of stretching-induced foaming of 5 MPa sample at a stretching rate of 50 mm/min and a strain of 300%. The gas-laden SIBS samples were prepared by reducing the delivery pressure enough to 5 MPa suppress the bubble nucleation caused by supersaturation, $P_{bubble} - P_{\mathrm{sys}}$.

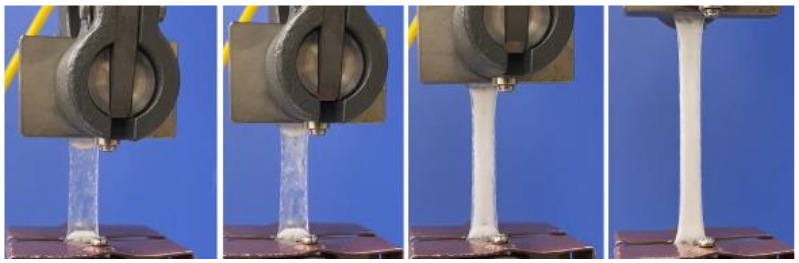

Figure 4.3 A series of snapshots of stretching-induced foaming at 50 mm/min stretching rate with 300% final strain (gas delivery pressure: 5 MPa).

The sample became white due to the occurrence of bubble nucleation in the polymer, and the whiteness increased as the strain increased. The digital camera images of SIBS samples before and after being stretched to 300% linear strain are given in Figures 4.9 and 4.10 in the Supporting Information.

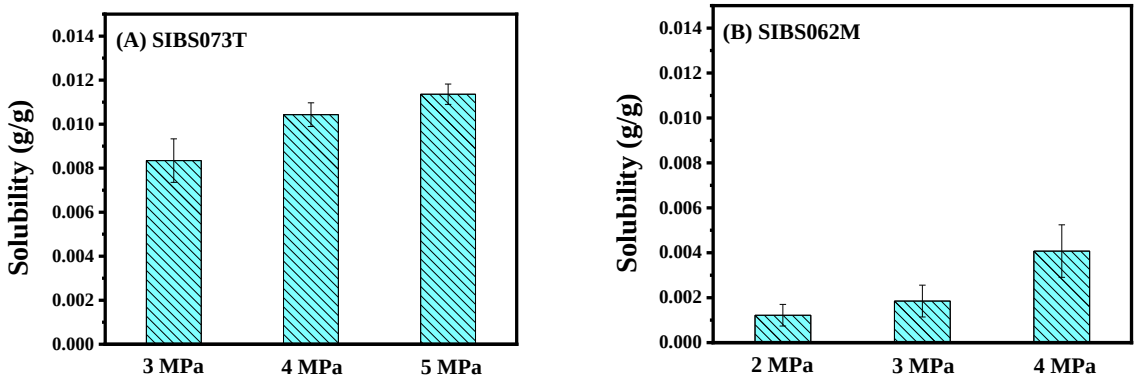

Figure 4.4 CO_2 contents in SIBS before stretching at room temperature.

Figure 4.4 shows the gas content of the gas-laden SIBS just after removing the samples from the injection molding process. The contents were calculated from the weight gain of the sample prepared under the designated gas delivery from one with no gas delivery. Because gas diffusion exists during weighing, the gas contents were not equivalent to the equilibrium solubility of CO_2 in SIBS. On the other hand, the weight gain reflected the gas contents before stretching. The important point that Figure 4.4 indicates is that the CO_2 content in SIBS increased with increasing delivery pressure at FIM.

To clarify the effects of gas contents, elastic modulus, and stretching rates on cell structure, stretching-induced foaming experiments were carried out by changing the gas delivery pressure of the injection molding process at three levels and the stretching rate of the tensile test for two grades of SIBS (073T and 062M) with different elastic moduli. The maximum strain was set to 300%, and the stretching rate was changed at four levels (50, 100, 200, and 400 mm/min).

4.4.3 Effect of Pressure on Cell Structure

Figure 4.5 shows the effect of CO_2 content on the cell structure of stretching-induced foams of SIBS073T prepared by stretching at the maximum stretching rate of 400 mm/min to 300% strain. When delivering CO_2 to SIBS062M at 5 MPa, it was not easy to prevent foaming caused by supersaturation. While delivering CO_2 to SIBS073T at 2 MPa, no foaming occurred during the stretching process. In addition, the bubble density increased as the CO_2 content increased for both polymers. SIBS062M foams showed a larger bubble size than SIBS073T because SIBS062M has a lower CO_2 content, as shown in Figure 4.4.

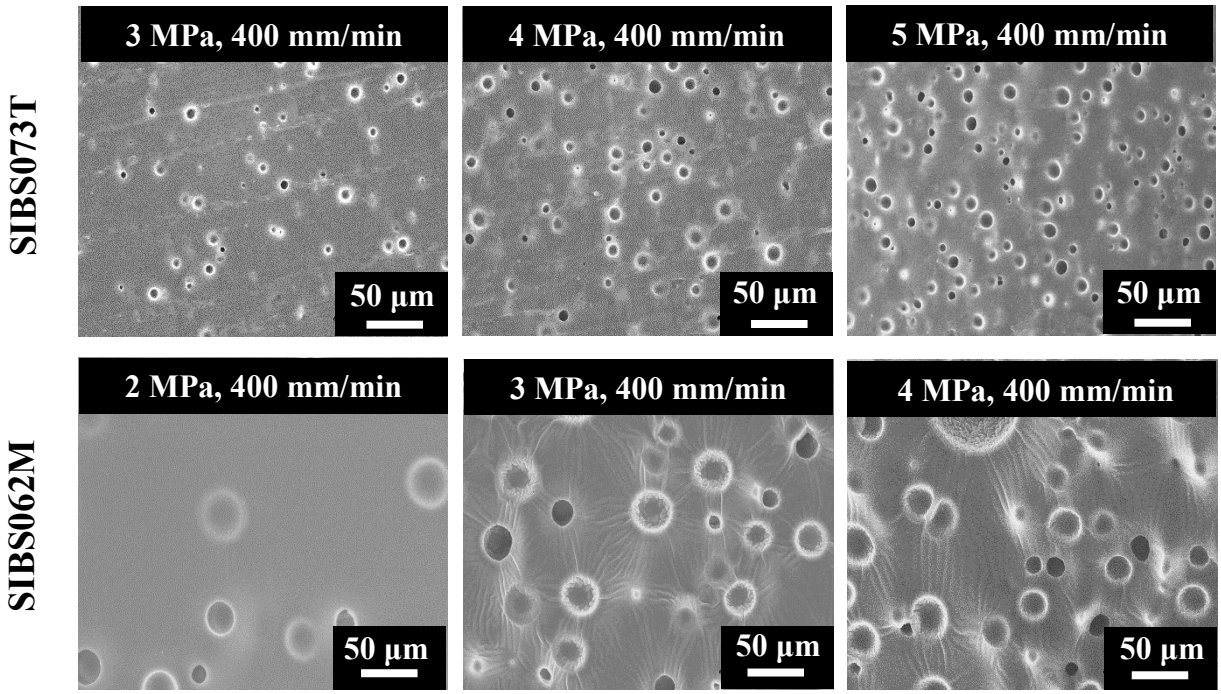

Figure 4.5 SEM images of the stretching-induced foams of SIBS073T and 062M with various pressures.

4.4.4 Effect of Stretching Rate on Cell Structure

Figure 4.6 shows the SEM images of the cell structure of the stretching-induced foam of SIBS073T prepared at different stretching rates, 50, 200, and 400 mm/min with 300 % strain under 5 MPa delivery pressure. The SEM images of unstretched CO_2-laden SIBS073T and SIBS062M, prepared at different delivery pressures, were given in Figures 4.14 and 4.15 in Supporting Information, showing a few larger bubbles were observed than the stretching-induced foaming samples.

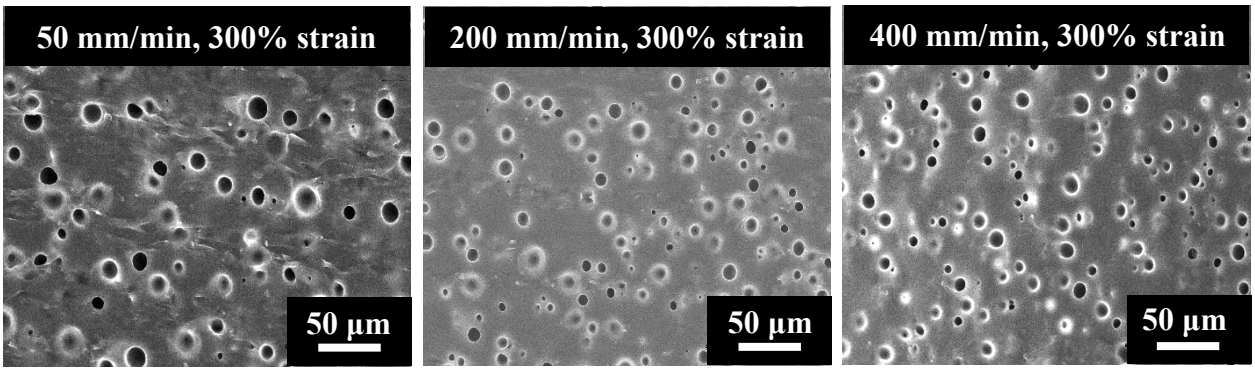

Figure 4.6 SEM images of the cell structure of stretching-induced foams of SIBS073T at different stretching rates (50, 200 and 400 mm/min) with strains of 300% and 5 MPa delivery pressure.

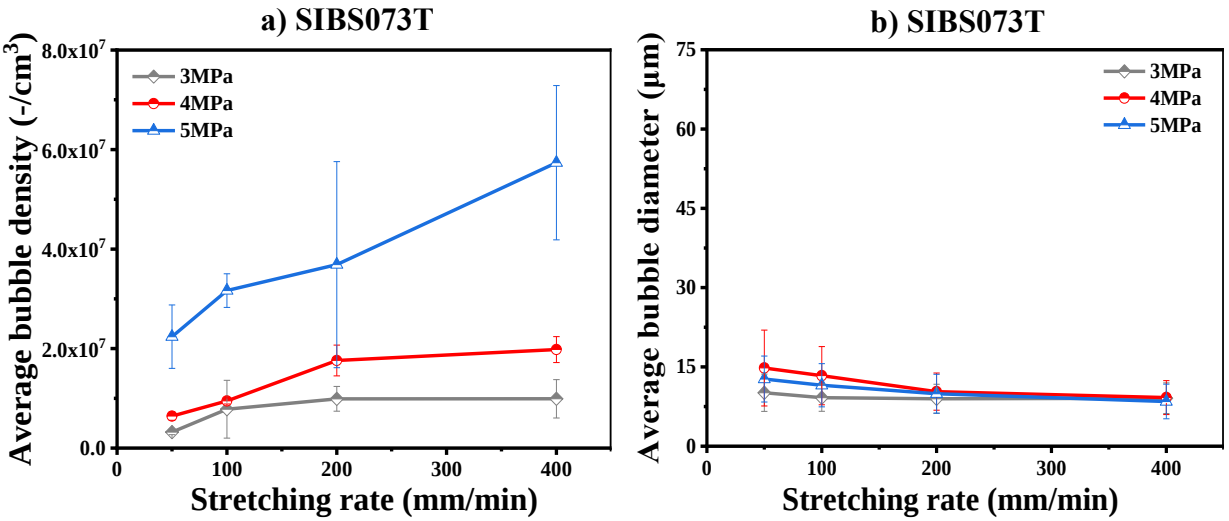

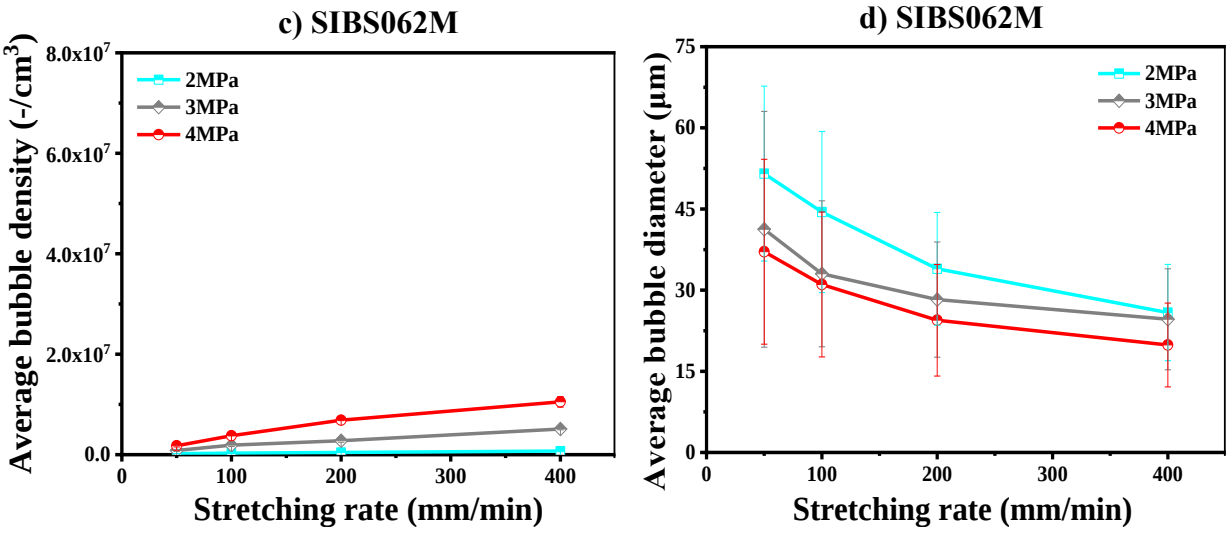

Figure 4.7 Bubble densities and diameters of stretching-induced SIBS073T (a, b) and SIBS062M (c, d) foams prepared at different stretching rates with 300% strain.

As the stretching rate increased, the bubble density increased, and the bubble size decreased. These trends can be clearly observed in Figure 4.7. Figure 4.7 shows the bubble density and diameter of the stretching-induced foams of SIBS073T and SIBS062M prepared at different stretching rates with 300% strain.

When the stretching rate and strain were set to 400 mm/min and 300% respectively, with 5 MPa CO_2 delivery pressure, the bubble density was approximately 5.74 $\times 10^7$ bubbles/cm^3, which was approximately 2.6 times greater than that prepared at 50 mm/min with 5 MPa CO_2 delivery pressure (Figure 4.7a). The sensitivity of the bubble density to the stretching rate increased as the CO_2 content increased. When comparing Figures. 4.7a with 4.7c, it can be said that the higher elastic SIBS073T bubble nucleation is more sensitive to the stretching rate.

These trends can be explained using Gibbs free energy equation, Eq. (4-18), with the estimated A_2 and B_2 values. Because A_2 is negative and B_2 is positive, with the increased stretching rate, the denominator of Eq. (4-18) increases, and the energy barrier, ΔG_{hom}, is lower. As a consequence, bubble nucleation is promoted by an increased stretching rate. Comparing these values of SIBS073T with those of SIBS062M, the values of SIBS073T are larger. As a result, the

sensitivity of bubble density to the stretching rate becomes greater with SIBS073T than with SIBS062M.

Furthermore, the gas content in the polymer before stretching was increased when the gas delivery pressure was increased. Thus, the degree of supersaturation term in Eq. (4-18), $\left(P_{bubble} - P_{\mathrm{sys}}\right)$, should become more significant as the gas content increases. Since the bubble nucleation rate, J, is an exponential function of ΔG_{hom}, i.e., $J \propto exp(-\frac{\Delta G_{hom}}{kT})$, the sensitivity of bubble nucleation to the stretching rate is greater at higher gas contents.

4.4.5 Effect of Strain on Cell Structure

Figure 4.8 summarizes the bubble densities and diameters of the stretching-induced foams of SIBS073T and SIBS062M with different strains. Figures 4.12 and 4.13 show the SEM images with various strains. Stretching was performed at a 400 mm/min stretching rate with three different final strains, 100, 200, and 300%, just after removing the polymer from the FIM, where the gas delivery pressure was changed at three levels. As the strain increased, the bubble density increased, and the bubble size decreased. The sensitivity of the bubble density of SIBS073T to the final strain was greater than that of SIBS062M, and the bubble nucleation barrier difference for SIBS073T and SIBS062M could be a key factor that affected the foam morphology. The sensitivity increased with the gas delivery pressure.

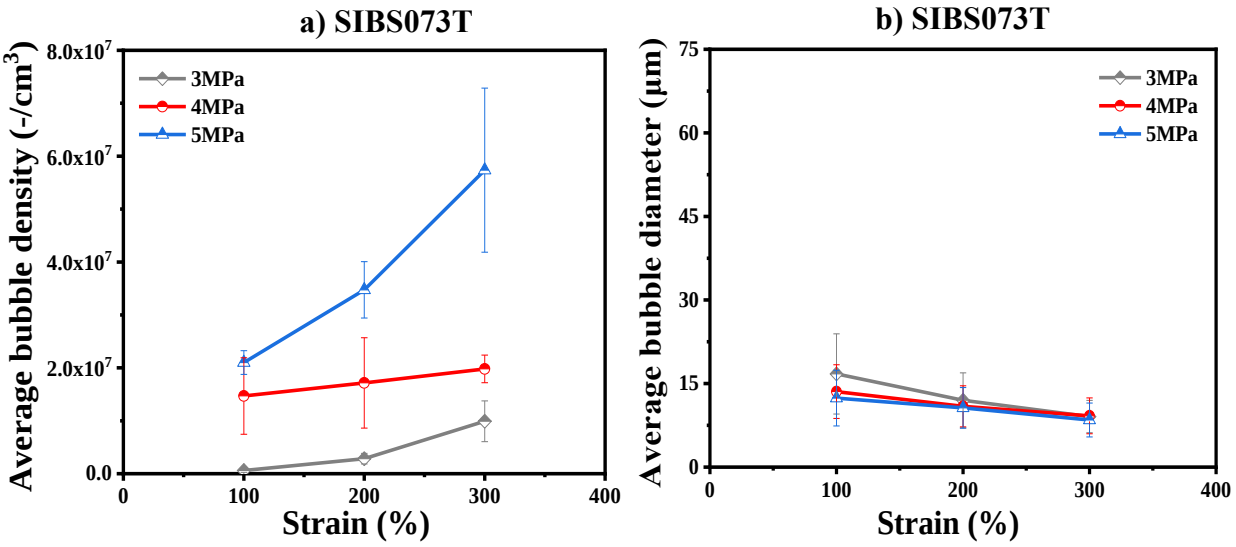

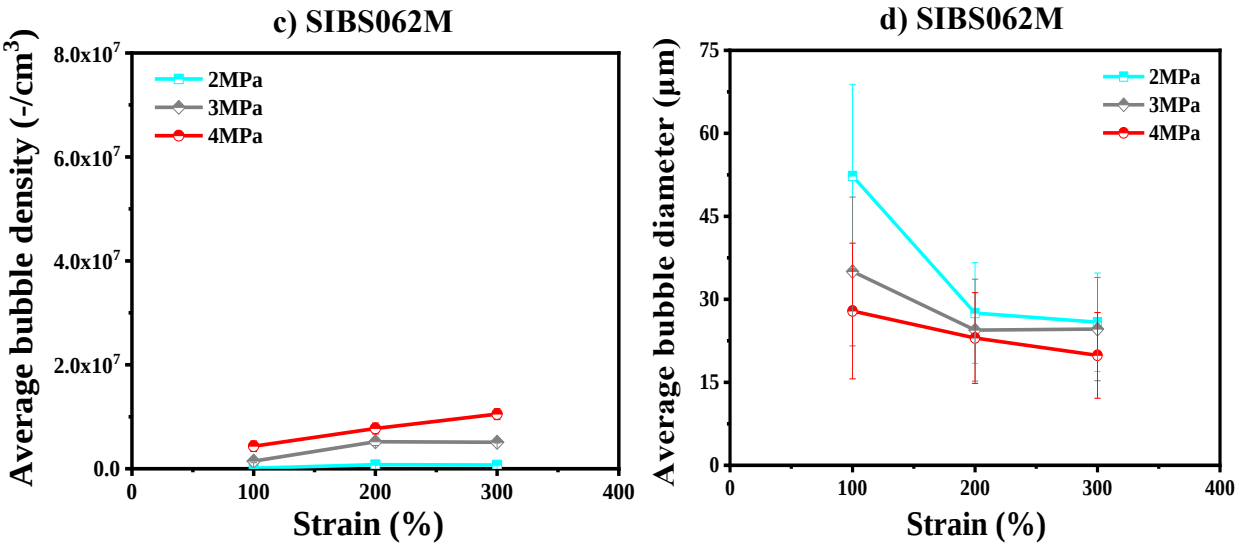

Figure 4.8 Bubble density and diameter of stretching-induced foams of SIBS073T (a, b) and SIBS062M (c, d) at three different strains with a 400 mm/min stretching rate.

These experimental results can also be explained using Eq. (4-14) with the estimated B_1 and B_2 values. Both values are positive, and ΔG_{hom}, was decreased by increasing the strain, ε_1. Then, bubble nucleation was enhanced. Comparing the B_1 and B_2 values of SIBS073T with those of SIBS062M, the values of SIBS073T are larger than those of SIBS062M. As a result, the sensitivity of bubble density to the strain becomes greater with SIBS073T than with SIBS062M. The effect of the gas delivery pressure on the sensitivity can be explained in the same way as the effect of the stretching rate on the bubble nucleation at different gas delivery pressures.

4.5 Conclusion

In this chapter, we conducted the stretching-induced foaming of a TPE, SIBS, using a tensile tester and foam injection molding machine. Two grades of SIBS with different elastic moduli were used. We fabricated foams with different bubble densities and sizes by changing the gas content of the gas-laden TPE, stretching rate, and final strain. We found that the larger the gas content was, the more significant the stretching rate and stretching amount (final strain) promoted bubble nucleation. Furthermore, the higher the elastic modulus TPE was stretched, the more

significant the stretching rate and amount (final strain) promoting the bubble nucleation. These experimental results suggested that the distortion energy and the elastic strain energy are essential factors of the thermoplastic elastomer foaming process and effectively enhance bubble nucleation. We could explain these experimental results by employing the Gibbs free energy of the classical nucleation theory for bubble nucleation with the critical distortion, and the total elastic strain energy density terms described as functions of stretching rate and strain. The increase in stretching rate and stretching amount reduces the energy barrier of bubble nucleation and provides an extra driving force of bubble nucleation.

The proposed bubble nucleation rate model is not precise enough to simulate the cell morphology, i.e., bubble density and size of the stretching-induced foam. When CO_2-laden elastomers are prepared, the plasticization effect may occur and change the rheological property, which affects the value of parameters A_1, A_2, B_1, and B_2 of the proposed model because these parameter values are determined from the rheological property. To precisely simulate the cell morphology of stretching-induced foaming, the plasticization effect on the elastic modulus, surface tension, and viscosity should be considered with the combination of the nucleation model with bubble growth and total mass balance models.

The knowledge obtained through this study can be utilized for practical foam processing of TPE, where it has been considered that TPE's physical foaming is difficult to be perform. One directional or biaxial stretching just after foam extrusion dies would enhance bubble nucleation and produce microcellular TPE by a physical foaming agent.

References

[1] Colton, J. S.; Suh, N. P. The Nucleation of Microcellular Thermoplastic Foam with Additives: Part I: Theoretical Considerations., *Polym. Eng. Sci.* 1987, 27, 485–492.

[2] Mokhtari Motameni Shirvan, M.; Famili, M. H. N.; Golbang, A. A Review on the Application of Nucleation Theories in Thermoplastic Foams. *Plast. Polym. Technol.* 2016, 4, 11–32.

[3] Han, J. H.; Han, C. D. A Study of Bubble Nucleation in a Mixture of Molten Polymer and Volatile Liquid in a Shear Flow Field. *Polym. Eng. Sci.* 1988, 28, 1616–1627.

[4] Lee, S.-T. Shear Effects on Thermoplastic Foam Nucleation. *Polym. Eng. Sci.* 1993, 33, 418–422.

[5] Lee, S.-T. More Experiments on Thermoplastic Foam Nucleation. *J. Cell. Plast.* 1994, 30, 444–453.

[6] Chen, L.; Wang, X.; Straff, R.; Blizard, K. Shear Stress Nucleation in Microcellular Foaming Process. *Polym. Eng. Sci.* 2002, 42, 1151–1158.

[7] Guo, M. C.; Peng, Y. C. Study of Shear Nucleation Theory in Continuous Microcellular Foam Extrusion. *Polym. Test.* 2003, 22, 705–709.

[8] Wong, A.; Chu, R. K. M.; Leung, S. N.; Park, C. B.; Zong, J. H. A Batch Foaming Visualization System with Extensional Stress-Inducing Ability. *Chem. Eng. Sci*. 2011, 66, 55–63.

[9] Wong, A.; Park, C. B. The Effects of Extensional Stresses on the Foamability of Polystyrene–Talc Composites Blown with Carbon Dioxide. *Chem. Eng. Sci.* 2012, 75, 49–62.

[10] Wong, A.; Park, C. B. A Visualization System for Observing Plastic Foaming Processes under Shear Stress. *Polym. Test.* 2012, 31, 417–424.

[11] Wong, A.; Guo, Y.; Park, C. B. Fundamental Mechanisms of Cell Nucleation in Polypropylene Foaming with Supercritical Carbon Dioxide—Effects of Extensional Stresses and Crystals. *J. Supercrit. Fluids* 2013, 79, 142–151.

[12] Wang, G.; Zhao, J.; Yu, K.; Mark, L. H.; Wang, G.; Gong, P.; Park, C. B.; Zhao, G. Role of Elastic Strain Energy in Cell Nucleation of Polymer Foaming and Its Application for Fabricating Sub-Microcellular TPU Microfilms. *Polymer* 2017, 119, 28–39.

[13] Gong, P.; Taniguchi, T.; Ohshima, M. Nanoporous Structure of the Cell Walls of Polycarbonate Foams. *J. Mater. Sci.* 2014, 49, 2605–2617.

[14] Wang, L.; Hikima, Y.; Ohshima, M.; Yusa, A.; Yamamoto, S.; Goto, H. Development of a Simplified Foam Injection Molding Technique and Its Application to the Production of High Void Fraction Polypropylene Foams. *Ind. Eng. Chem. Res.* 2017, 56, 13734–13742.

[15] Wang, L., Wakatsuki, Y., Hikima, Y., Ohshima, M., Yusa, A., Uezono, H. Naitou, A. Preparation of Microcellular Injection-Molded Foams Using Different Types of Low-Pressure

Gases via a New Foam Injection Molding Technology, *Ind. Eng. Chem. Res.* 2019, 58, 17824−17832.

[16] Kong, H. J.; Lee, S. H.; Kim, D. G.; Kim, H. J.; Park, G. W.; Hyun, K. Investigation of Thermoplastic Elastomer (TPE) Foaming Process Using Blowing Agent by Rheological and Morphological Methods. *J. Appl. Polym. Sci*. 2019, 136, 47358.

[17] Kumar, V.; Suh, N. P. A Process for Making Microcellular Thermoplastic Parts. *Polym. Eng. Sci.* 1990, 30, 1323–1329.

[18] Kim, N. H.; Sankar, B. V.; Kumar, A. V. *Introduction to Finite Element Analysis and Design, 2nd Edition*, John Wiley &Sons Ltd.: New Jersey, 2018.

[19] Irgens, F. Continuum mechanics. Springer: Berlin, 2008.

[20] Rottler, J.; Robbins, M. O. Yield Conditions for Deformation of Amorphous Polymer Glasses. *Phys. Rev. E.* 2001, 64, 051801-1−051801-8.

[21] Ward, I. M. Review: The Yield Behaviour of Polymers. *J. Mater. Sci*. 1971, 6, 1397–1417.

[22] Lazzeri, A.; Bucknall, C. B. Applications of a Dilatational Yielding Model to Rubber-Toughened Polymers. *Polymer* 1995, 36, 2895–2902.

[23] Whitney, W.; Andrews, R. D. Yielding of Glassy Polymers: Volume Effects. *J. Polym. Sci., Part C: Polym. Symp*. 1967, 16, 2981–2990.

[24] Bowden, P. B.; Jukes, J. A. The Plastic Flow of Isotropic Polymers. *J. Mater. Sci*. 1972, 7, 52–63.

[25] Verbeeten, W. M. H.; Sánchez-Soto, M.; Maspoch, M. L. Hydrostatic Pressure Dependence in Tensile and Compressive Behavior of an Acrylonitrile–Butadiene–Styrene Copolymer. *J. Appl. Polym*. Sci. 2022, 139, 52295.

[26] Bucknall, C. B. New Criterion for Craze Initiation. *Polymer* 2007, 48, 1030–1041.

[27] Duckett, R. A.; Rabinowitz, S.; Ward, I. M. The Strain-Rate, Temperature and Pressure Dependence of Yield of Isotropic Poly(Methylmethacrylate) and Poly(Ethylene Terephthalate). *J. Mater. Sci*. 1970, 5, 909–915.

[28] Yu, J.; Fei, Q.; Zhang, P.; Li, Y.; Zhang, D.; Guo, F. An Innovative Yield Criterion Considering Strain Rates Based on von Mises Stress. *J. Press. Vessel Technol.* 2019, 142, 014501-1–014501-6.

[29] Du, X.; Zhang, Q.; Wan, Z. A Nonlinear Constitutive Model for Rayon-Rubber Composite in the Medium Strain Rate Range. *J. Elastomers Plast.* 1995, 27, 91–99.

[30] Okoli, O. I.; Smith, G. F. The Effect of Strain Rate and Fibre Content on the Poisson's Ratio of Glass/Epoxy Composites. *Compos. Struct.* 2000, 48, 157–161.

[31] Offset Yield Strength. INSTRON®, Illinois Tool Works Inc. https://www.instron.com/en-us/resources/glossary/o/offset-yield-strength?region=North%20America&lang=en-US (accessed 2022/11/04)

[32] Henry, C.; Rupel, K.; Park, C.; Costanzo, J.; Kaczowka, C.; Malik, K.; Ghose, S. Evaluation of an Alternate Method for Determining Yield Strength Offset Values for Selective Laser Sintered Polymeric Materials, *SAMPE 2019 Charlotte, N*C, 2019, 20200002670.

S4 Supporting Information

S4.1 Some More Details of Gibbs Free Energy that Prof Park's Group Proposed

Wang et al.[1] introduced an elastic strain energy barrier, ΔG_{eb}, and ΔG_{st}, and their densities into the Gibbs free energy:

$$\Delta G = -\frac{4\pi}{3}R^3\left(P_{bubble} - P_{sys}\right) + 4\pi R^2\gamma + \Delta G_{eb} + \Delta G_{st}$$

$$\Delta G_{eb} + \Delta G_{st} = \Delta G_{eb} + \Delta G_h + \Delta G_d = -\frac{4\pi R^3}{3}(-\Delta g_{eb} + \Delta g_h + \Delta g_d) \qquad (4\text{-}21)$$

$$\Delta g_h = \frac{3}{2}\frac{(1-2v)}{E}\sigma_{\mathrm{h}}^2 \qquad (4\text{-}22)$$

$$\Delta g_d = \frac{1+v}{3E}\sigma_{\mathrm{vm}}^2 \qquad (4\text{-}23)$$

$$\Delta g_{eb} = \frac{1+v}{3E}\sigma_e^2 = \frac{1+v}{3E}(\sigma_y - \mu\sigma_h)^2 \qquad (4\text{-}24)$$

In their notation, ΔG_{st} represents the elastic strain energy stored at the nucleation sites right before bubble nucleation. It is further divided into dilatational energy, ΔG_h, and distortional energy, ΔG_d. Introducing the energy density (energies per unit volume) Δg_{eb}, Δg_h, and Δg_d, Gibbs free energy is described with the dilatational and distortional energies when a bubble with radius R is born. The continuum mechanism[2] and the von Mises theory[3] give Eq. (4-21) with Poison's ratio, v, and the elastic modulus, E, the dilatational stress, σ_h, von Mises stress, σ_{vm}, the stress at yield, σ_e, yield stress, σ_y and dimensionless constant, μ.

S4.2 Constitutive Equations with Elastic Stiffness Coefficients

Yu et al.[4] developed a yield criterion as a function of strain rate, starting from the following constitutive equation:[4-5]

$$\boldsymbol{\sigma} = \boldsymbol{C\varepsilon} + \boldsymbol{F\dot{\varepsilon}}^n \qquad (4\text{-}25)$$

where $\boldsymbol{\varepsilon}$ and $\boldsymbol{\dot{\varepsilon}}$ are total strain and strain rate tensors. n is a material constant describing the strain rate sensitivity of stress. C is elastic stiffness matrix relating between strain and stress by Hooke's law. F is the coefficient matrix concerning the stress and strain rate relationship, which is assumed to have similar structure in form with elastic stiffness matrix C. These two matrices are expressed by:

$$C = \begin{bmatrix} k_{11} & k_{12} & k_{13} & & & \\ k_{21} & k_{22} & k_{23} & & & \\ k_{31} & k_{32} & k_{33} & & & \\ & & & k_{44} & & \\ & & & & k_{55} & \\ & & & & & k_{66} \end{bmatrix}, F = \begin{bmatrix} f_{11} & f_{12} & f_{13} & & & \\ f_{21} & f_{22} & f_{23} & & & \\ f_{31} & f_{32} & f_{33} & & & \\ & & & f_{44} & & \\ & & & & f_{55} & \\ & & & & & f_{66} \end{bmatrix} \quad (4\text{-}26)$$

S4.3 How to Calculate A_1 and B_1 From the Elastic Stiffness Matrix and Poisson's Ratio

From the literature,[6] we can know the elastic stiffness matrix of an isotropic material (Eq. (4-27)).[6] If we regard SIBS as an isotropic material, A_1 can be calculated with k_{11}, k_{12} and k_{13} (seen in Eq. (4-28)).

$$\begin{bmatrix} \sigma_{11} \\ \sigma_{22} \\ \sigma_{33} \\ \sigma_{23} \\ \sigma_{13} \\ \sigma_{12} \end{bmatrix} = \frac{E}{(1+\nu)(1-2\nu)} \begin{bmatrix} 1-\nu & \nu & \nu & 0 & 0 & 0 \\ \nu & 1-\nu & \nu & 0 & 0 & 0 \\ \nu & \nu & 1-\nu & 0 & 0 & 0 \\ 0 & 0 & 0 & \frac{(1-2\nu)}{2} & 0 & 0 \\ 0 & 0 & 0 & 0 & \frac{(1-2\nu)}{2} & 0 \\ 0 & 0 & 0 & 0 & 0 & \frac{(1-2\nu)}{2} \end{bmatrix} \begin{bmatrix} \varepsilon_{11} \\ \varepsilon_{22} \\ \varepsilon_{33} \\ 2\varepsilon_{23} \\ 2\varepsilon_{13} \\ 2\varepsilon_{12} \end{bmatrix} - \frac{E\alpha\Delta T}{1-2\nu} \begin{bmatrix} 1 \\ 1 \\ 1 \\ 0 \\ 0 \\ 0 \end{bmatrix} \quad (4\text{-}27)$$

Using Eqs. (4-26) and (4-27) to get k_{ij} (i = 1,2,3, j = 1,2,3) (Poisson's ratio is assumed to be 0.49 and E can be obtained from S-S curve). The A_1 and B_1 can be obtained by using Eq. (4-29) and Eq. (4-30) respectively.

$$\begin{cases} k_{11} = \frac{E}{(1+v)(1-2v)} \times (1-v) \\ k_{12} = \frac{E}{(1+v)(1-2v)} \times (1-v) \\ k_{13} = \frac{E}{(1+v)(1-2v)} \times v \end{cases} \quad (4\text{-}28)$$

$$A_1 = \frac{1}{2}(k_{11} - v_{21}k_{12} - v_{31}k_{13}) - \frac{1}{18}\sum_{i,j=1}^{3} k_{ij}\,(1 - v_{21} - v_{31})^2 \quad (4\text{-}29)$$

$$B_1 = k_{11} - v_{21}k_{12} - v_{31}k_{13} \quad (4\text{-}30)$$

where Poisson's ratio v is equal in value for all directions. i.e., $v_{ij} = v$ (constant).

S4.4 Digital Camera Image of the Stretching-Induced Foaming

Figures 4.9 and 4.10 show the digital camera picture of unstretched and stretched gas-laden SIBS073T (3, 4, 5 MPa) and SIBS062M (2, 3, 4 MPa) after a few hours after injection molding. The first samples on the left were unstretched. The pictures of stretched samples were taken after stretched to linear strain of 300%. The numbers indicate the stretching rate, where 1, 2, 3 and 4 represent 50, 100, 200 and 400 mm/min respectively. Stretched samples of all conditions turned white due to foaming, which could be seen in all these pictures.

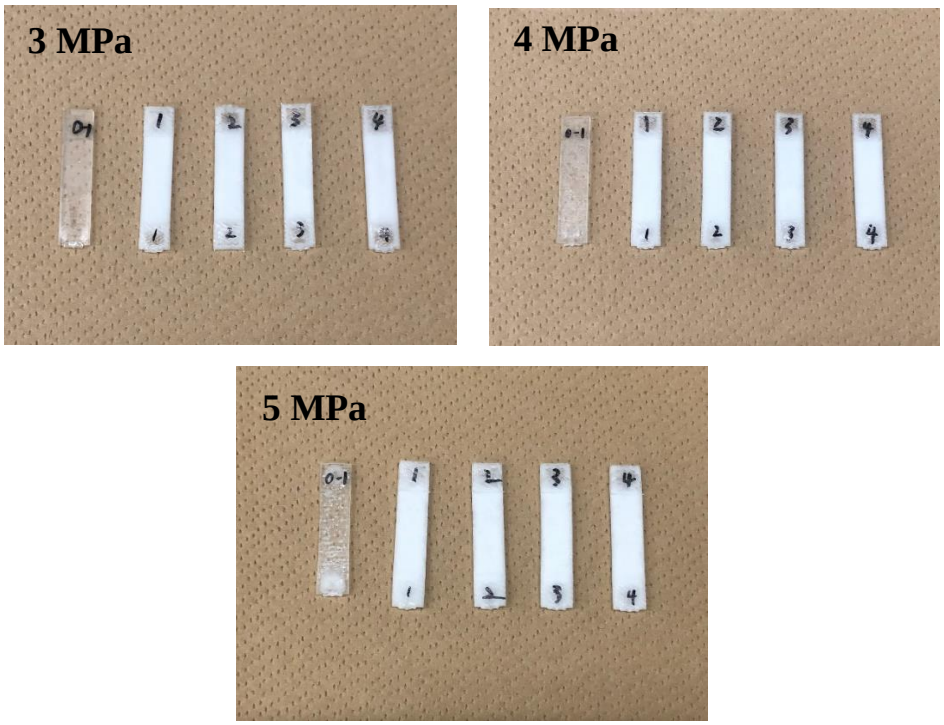

Figure 4.9 Digital camera picture of unstretched and stretched gas-laden SIBS073T with various pressures.

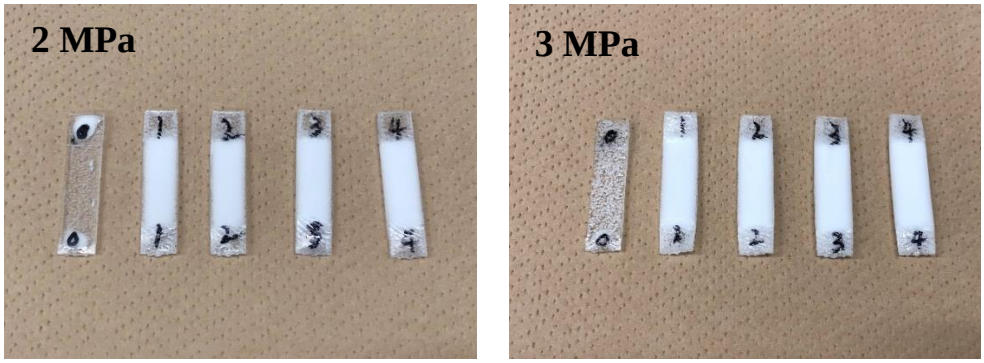

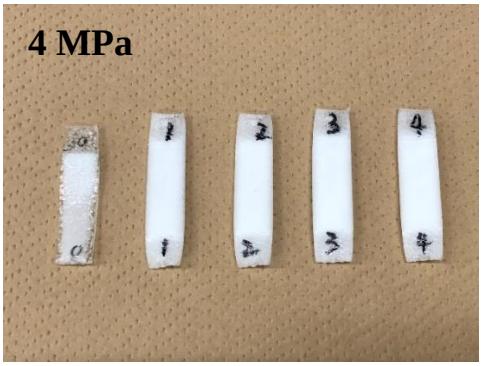

Figure 4.10 Digital camera picture of unstretched and stretched gas-laden SIBS062M with various pressures.

S4.5 SEM Images of SIBS062M at Various Stretching Rates with 300% Stain and 4 MPa Delivery Pressure

Figure 4.11 show SEM images of SIBS062M stretching-induced foams at different stretching rates with a strain of 300% and a delivery pressure of 4 MPa, indicating that higher stretching rate (400 mm/min) is more beneficial for increasing the bubble density, compared with lower stretching rate (50 mm/min).

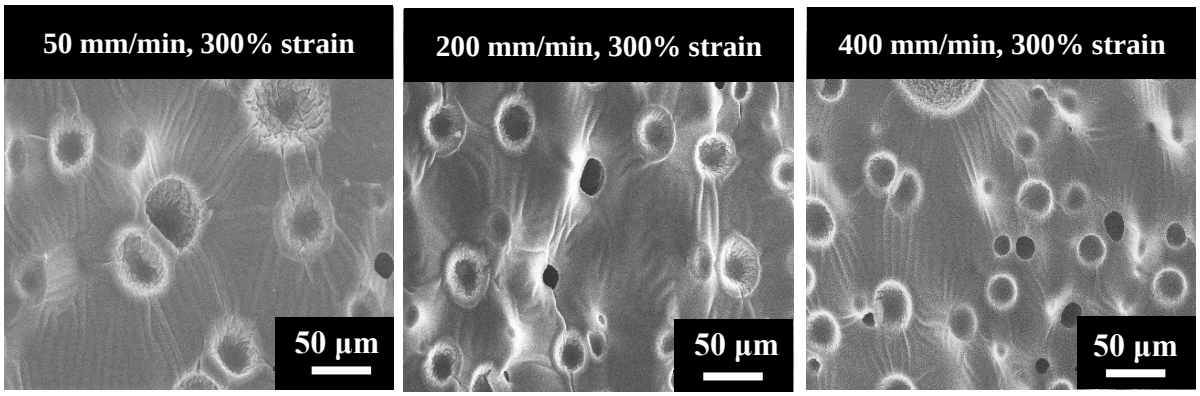

Figure 4.11 SEM images of the cell structure of stretching-induced foams of SIBS062M at different stretching rates (50, 200 and 400 mm/min) with strains of 300% and 4 MPa delivery pressure.

S4.6 SEM Images of SIBS073T and 062M Stretching-Induced Foam at Various Strains with Stretching Rate of 400 mm/min

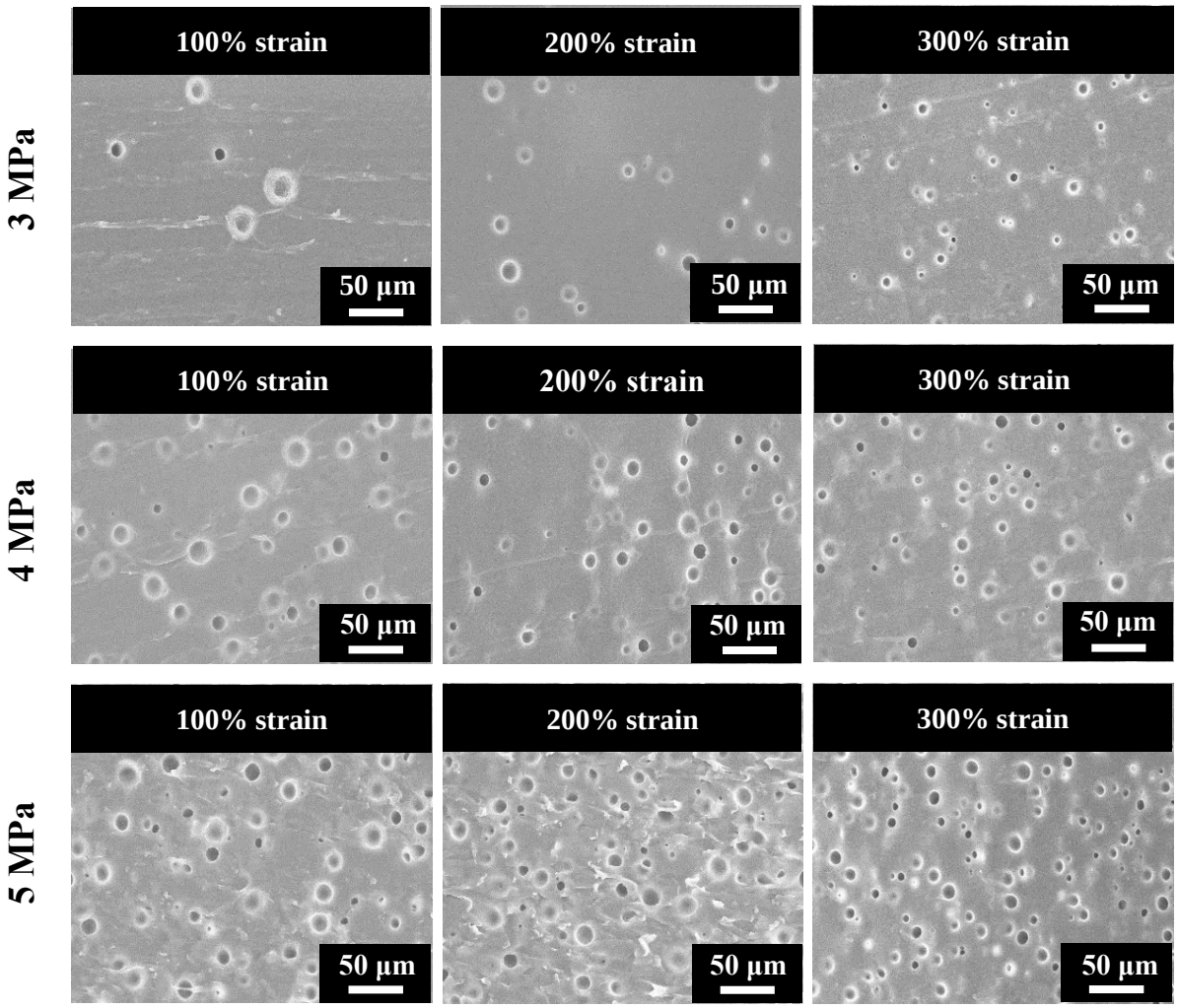

Figure 4.12 SEM images of cell structure of stretching-induced foams of SIBS073T at different strains (100, 200 and 300%) with stretching rate of 400 mm/min and different CO_2 delivery pressure.

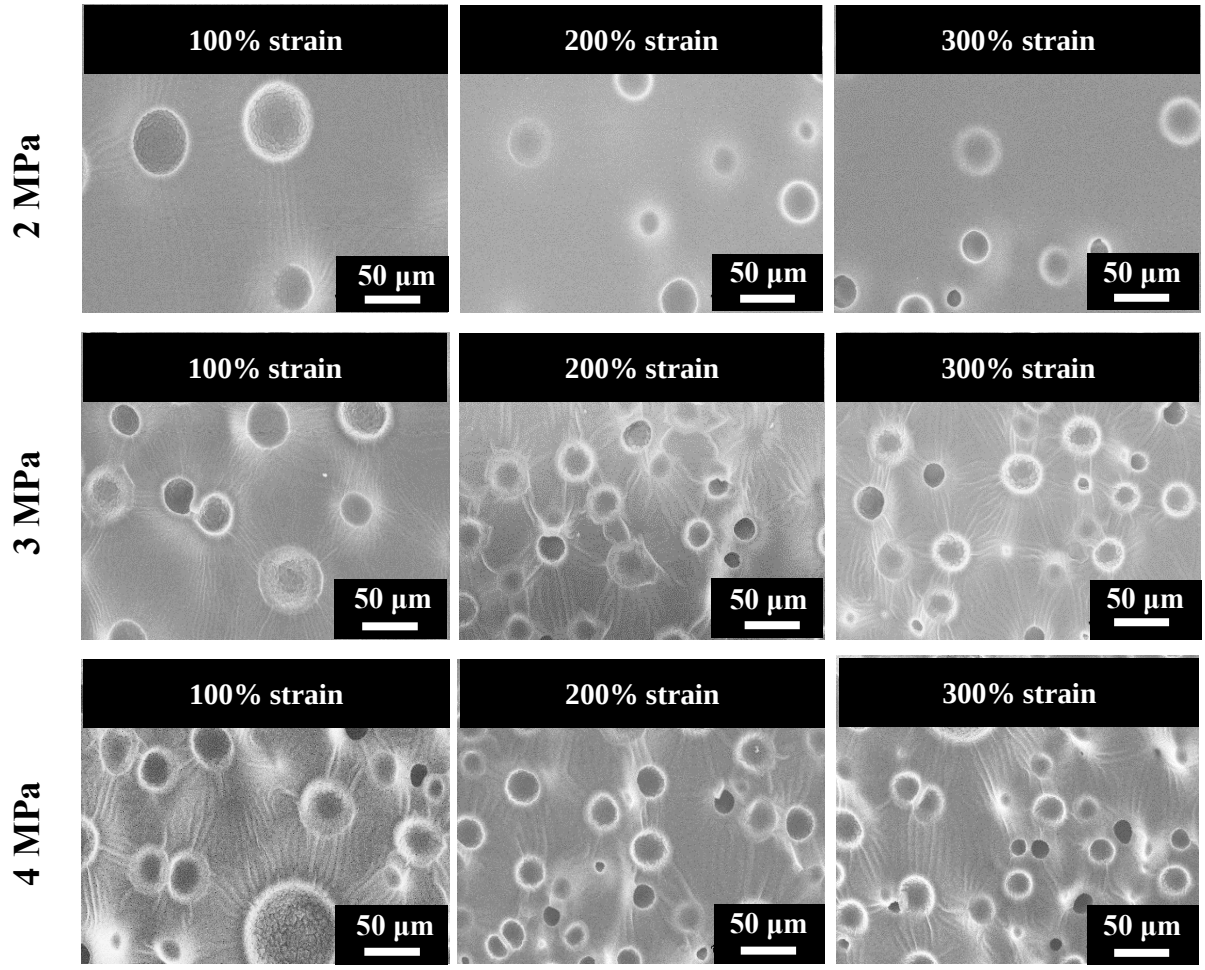

Figure 4.13 SEM images of cell structure of stretching-induced foams of SIBS062M at different strains (100, 200 and 300%) with stretching rate of 400 mm/min and different CO_2 delivery pressure.

S4.7 SEM Images of SIBS073T and 062M Unstretched CO_2-Laden Samples

Figures 4.14 and 4.15 shows morphology of CO2-laden SIBS073T and 062M samples without stretching, respectively. Apparently, no bubbles could be seen under all pressures for SIBS073T as shown in Figure 4.14, while there were some bubbles for SIBS062M in Figure 4.15. Even though bubbles could be observed without stretching for SIBS062M, bubble density was way lower, and bubble size was much larger than those with stretching shown in Figure 4.11 when compared at the same high magnification (Figure 4.15(A'), (B') and **(**C')). It indicates that the positive effect of stretching rates on bubble nucleation for SIBS062M could be also clarified.

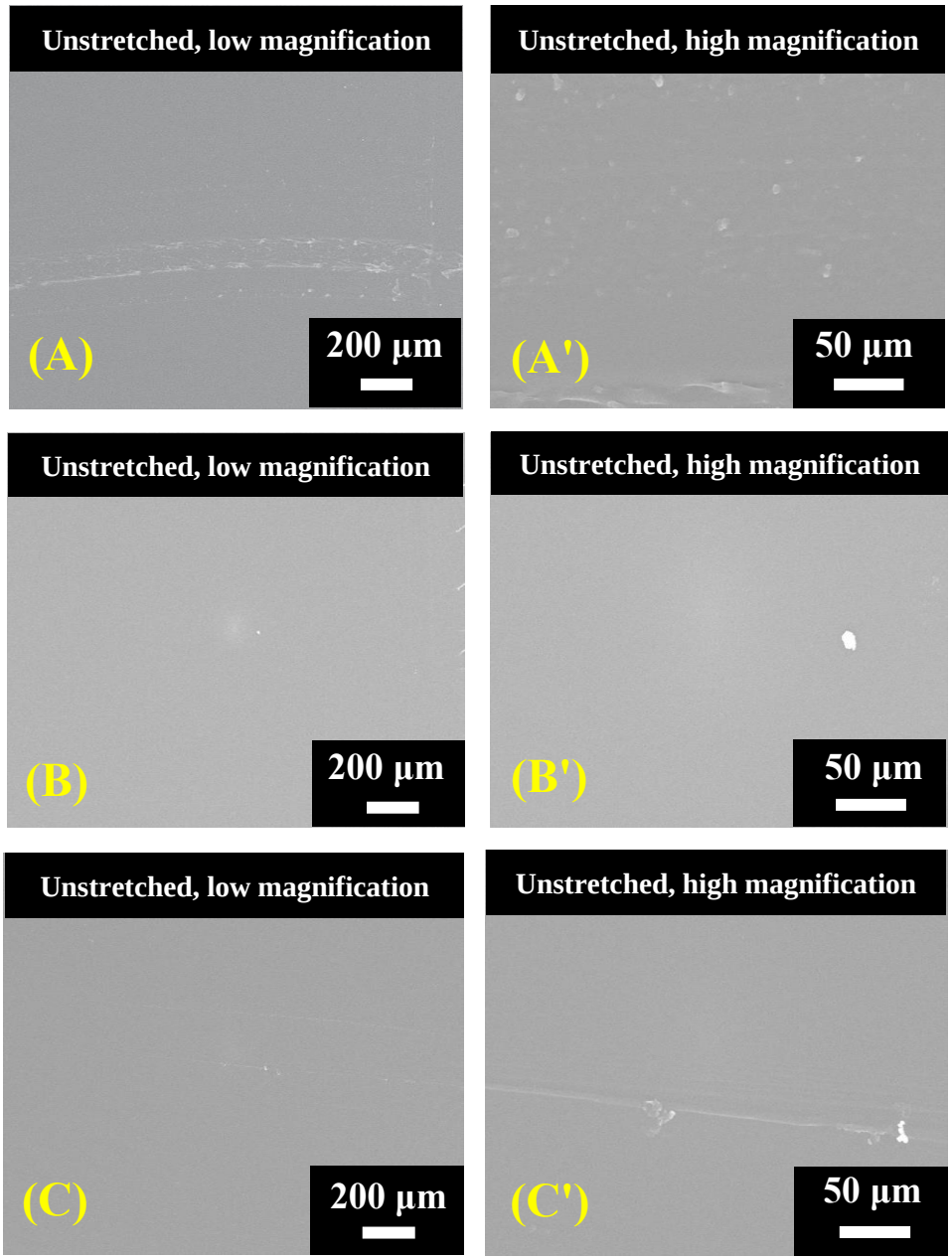

Figure 4.14 SEM images of unstretched CO_2-laden SIBS073T samples. (A), (B) and (C) represent unstretched samples with 3, 4 and 5 MPa at low magnification, respectively; (A'), (B') and (C') represent unstretched samples with 3, 4 and 5 MPa at high magnification, respectively.

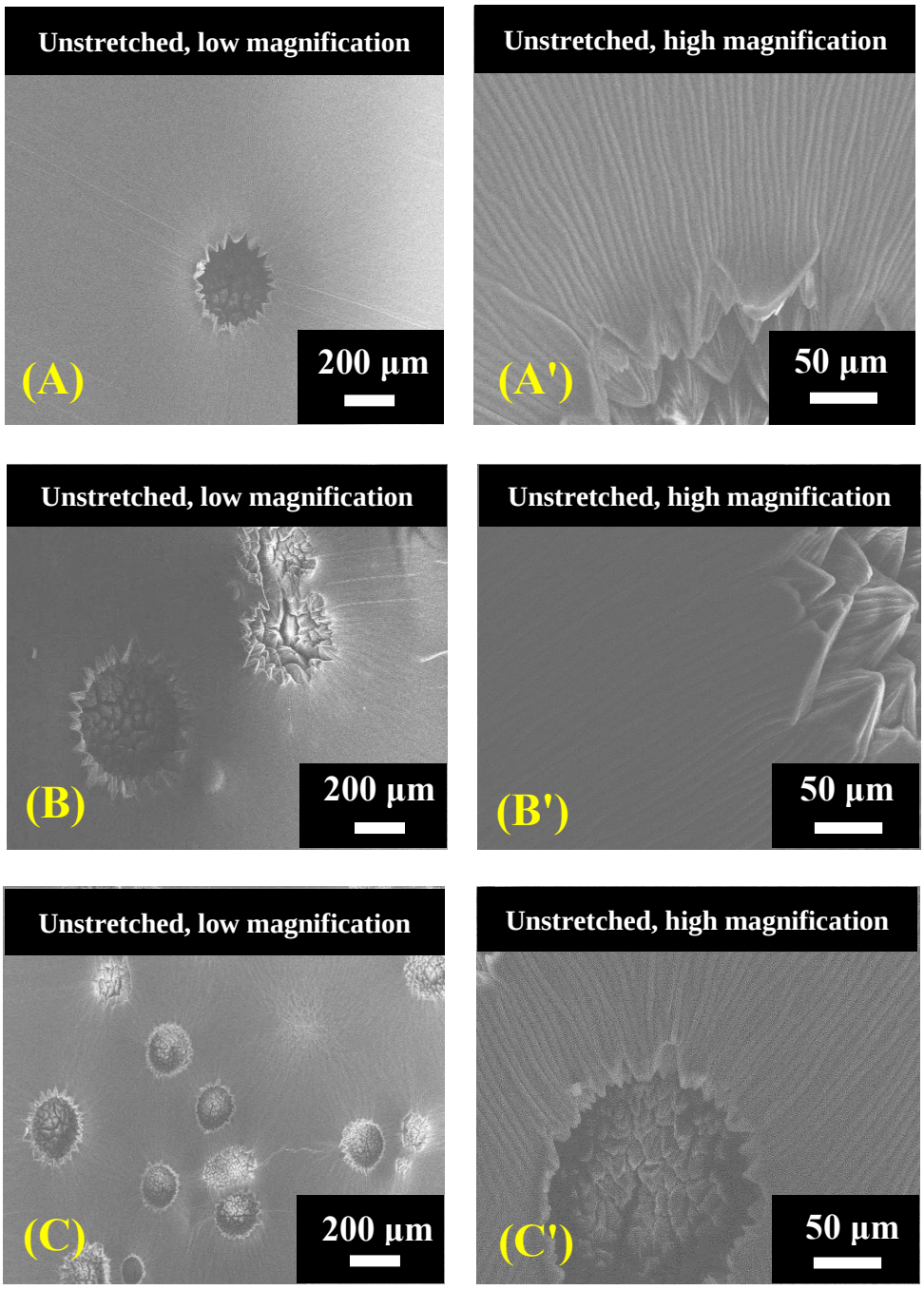

Figure 4.15 SEM images of unstretched CO_2-laden SIBS062M samples. (A), (B) and (C) represent unstretched samples with 2, 3 and 4 MPa at low magnification, respectively; (A'), (B') and (C') represent unstretched samples with 2, 3 and 4 MPa at high magnification, respectively.

References of Supporting Information

[1] Wang, G.; Zhao, J.; Yu, K.; Mark, L. H.; Wang, G.; Gong, P.; Park, C. B.; Zhao, G. Role of Elastic Strain Energy in Cell Nucleation of Polymer Foaming and Its Application for Fabricating Sub-Microcellular TPU Microfilms. *Polymer* 2017, 119, 28–39.

[2] Kim, N. H.; Sankar, B. V.; Kumar, A. V. *Introduction to Finite Element Analysis and Design, 2nd Edition*, John Wiley &Sons Ltd.: New Jersey, 2018.

[3] Ward, I. M. Review: The Yield Behaviour of Polymers. *J. Mater. Sci*. 1971, 6, 1397–1417.

[4] Yu, J.; Fei, Q.; Zhang, P.; Li, Y.; Zhang, D.; Guo, F. An Innovative Yield Criterion Considering Strain Rates Based on von Mises Stress. *J. Press. Vessel Technol.* 2019, 142, 014501-1–014501-6.

[5] Du, X.; Zhang, Q.; Wan, Z. A Nonlinear Constitutive Model for Rayon-Rubber Composite in the Medium Strain Rate Range. *J. Elastomers Plast.* 1995, 27, 91–99.

[6] Bower, A. F.; *Applied Mechanics of Solid – Chapter 3 Constitutive Models: Relations between Stress and Strain*; CRC Press: Boca Raton, 2009.

Chapter 5 General Conclusion

5.1 Conclusion of Each Chapter

This dissertation has introduced several issues in microcellular foam injection molding and methods to improve the foamability and performances. In Chapter 1, the basic knowledge about polymer foaming was discussed, and purposes of this dissertation were revealed.

In Chapter 2, microcellular foaming injection molding of a kind of amorphous thermoplastic elastomer SIBS was conducted with high pressure of N_2. By introducing a semi-crystalline polymer PP, the foamability can be improved in foam injection molding processes. By adjusting the foaming temperature to the crystallization temperature of PP, it is shown that PP crystals promote the generation of bubble nucleation sites and increase the viscosity to suppress bubble growth. Microcellular foams with introduction of PP possesses high cell density and small cell size, which were achieved at 10^8 cells/cm^3 and about 13 μm respectively. Additionally, shrinkage has been one of critical issues of injection-molded elastomer foams, as described in advance in Dissertation Overview of Chapter 1. The result of shrinkage ratio change shown in Figure 11, PP can also impede the shrinkage of SIBS foams.

In Chapter 3, a novel method has been proposed to reduce the surface imperfections of injection-molded PP foam from the viewpoint of material property perspective. By introducing SIBS, reduced viscosity lower than crystallization temperature can have positive effect on reduction of surface imperfection, where bubbles can be easily dissolved at polymer/mold interface. However, since there is no significant crystallization retarding effect of SIBS. Interestingly, increased *Sa* with increasing SIBS content can be obtained, which can be possibly owing to large bubble size caused by large-sized domains. This phenomenon limits the efficacy of SIBS on surface improvement. LMPP and MD were used as surface appearance modifier based on different mechanism: LMPP is able to delay the crystallization of HPP at the skin layer and also solidification, which is allowed to have enough time to squeeze the bubbles smaller; MD has efficacy in increasing the viscosity at high temperature during the filling stage, which is helpful to reduce the generated bubble size at the flow front. The results also indicate the prominent effect of LMPP and MD on surface appearance improvement. Surface roughness (*Sa*) of HPP/60%LMPP

foam can achieve as low as 4.03 μm, compared with that of HPP foam (9.79 μm), while *Sa* of HPP/30%LMPP/0.3%MD foam is around 5.09 μm.

In Chapter 4, a method of stretching-induced microcellular foaming of gas-laden SIBS has been proposed. As described in Dissertation Overview of Chapter 1, there is difficulty in fabricating microcellular injection-molded SIBS foam with low pressure of blowing agent. Whereas, gas-laden SIBS with low-pressure CO_2 can be prepared. Hence, stretching-induced microcellular foaming has been conducted to promote the generation of bubbles. It is demonstrated that high-pressure blowing agents, high stretching rates and high strains are favorable to high bubble densities and small bubble sizes. By comparing A_1, B_1 and B_2 of SIBS073T and SIBS062M, sensitivity of bubble density to stretching rate and strain with both SIBS has been explained. Furthermore, proposed stretching rate-dependent model with bubble growth and total mass balance models can be combined for precise simulation in the future.

5.2 Future Prospects

This dissertation mainly focuses the microcellular foaming of thermoplastic elastomer. As discussed in Chapter 3, SIBS has potential in biomedical application owing to its biocompatibility and biostability. More significantly, SIBS possesses similar biocompatibility with much better dynamic fatigue properties in comparison with those of silicone rubber.[1,2] In recent years, a variety of studies concentrating on SIBS application in biomedical area. For example, a liquid-infused SIBS microfiber coating was prepared by Yuan. et al.,[3] which could help reduce the infection and thrombosis when coated on the medical device. Zhu et al.[4] reported that sulfonated SIBS (S-SIBS) showed better hemocompatibility with superior inflammation reduction property compared with standard drug-cluting stents. Despite biomedical applications, Elabd et al.[5] found the higher iso-exchange capacity of S-SIBS and revealed higher proton conductivity compared with those of sulfonated polystyrene and Nafion 117. Based on this findings, Ramos-Rivera et al.[6] fabricated poly(arylene ether sulfone)/S-SIBS proton exchange membranes for direct methanol fuel cell , where blend membranes showed enhanced transport properties and proton conductivity. These properties and applications of SIBS signify the potential applications and promising future of SIBS foaming.

Besides SIBS, physical foaming of other thermoplastic elastomer has also been attractive in the future. Elastomer foams in various shape such as microfilm, films, sheet, bead foams can be prepared by physical foaming technologies (e.g. foam injection molding) for different purposes.[7] It is possible and potential for researchers to fabricate thermoplastic elastomer foams with valuable properties for specific applications.

References

[1] Maji, P.; Naskar, K. Styrenic Block Copolymer-Based Thermoplastic Elastomers in Smart Applications: Advances in Synthesis, Microstructure, and Structure–Property Relationships—a Review. *J. Appl. Polym. Sci*. 2022, 139, e52942.

[2] El Fray, M.; Prowans, P.; Puskas, J. E.; Altstädt, V. Biocompatibility and Fatigue Properties of Polystyrene−Polyisobutylene−Polystyrene, an Emerging Thermoplastic Elastomeric Biomaterial. *Biomacromolecules* 2006, 7, 844–850.

[3] Yuan, S.; Li, Z.; Song, L.; Shi, H.; Luan, S.; Yin, J. Liquid-Infused Poly(Styrene-B-Isobutylene-B-Styrene) Microfiber Coating Prevents Bacterial Attachment and Thrombosis. *ACS Appl.Mater. Interfaces* 2016, 8, 21214–21220.

[4] Zhu, J.-Z.; Xiong, X.-W.; Du, R.; Jing, Y.-J.; Ying, Y.; Fan, X.-M.; Zhu, T.-Q.; Zhang, R.-Y. Hemocompatibility of Drug-Eluting Coronary Stents Coated with Sulfonated Poly (Styrene-Block-Isobutylene-Block-Styrene). *Biomaterials* 2012, 33, 8204–8212.

[5] Elabd, Y. A.; Napadensky, E.; Walker, C. W.; Winey, K. I. Transport Properties of Sulfonated Poly(Styrene-B-Isobutylene-B-Styrene) Triblock Copolymers at High Ion-Exchange Capacities. *Macromolecules* 2005, 39, 399–407.

[6] Ramos-Rivera, G.; Suleiman, D. High-Performance Blended Membranes Based on Poly(Arylene Ether Sulfone) and Sulfonated Poly(Styrene-Isobutylene-Styrene) for Direct Methanol Fuel Cell Applications. *J. Appl. Polym. Sci*. 2022, 139, 52027.

[7] Zhai, W.; Jiang, J.; Park, C. B. A Review on Physical Foaming of Thermoplastic and Vulcanized Elastomers. *Polym. Rev.* 2021, 62, 95–141.

List of Figures and Tables

Figures

Tables

Acknowledgement

All the research was done in the Materials Processing Engineering Laboratory, Department of Chemical Engineering, Graduate School of Engineering, Kyoto University, with kind help and support from many people.

First of all, I would like to show my sincerest and deepest gratitude to my supervisor, Prof. Masahiro Ohshima, for his guidance and support during my 3-year Ph.D. course in Kyoto University. Whenever I have question with research, you have always given me the biggest support. Being under your instruction, I've learnt so much experience in research and study about microcellular foaming and material processing. Furthermore, you have cared about my financial situation and offered me a part-time job in the lab. It does really help. More significantly, you have taught me what is research, and encouraged me to be confident and think independently. Your kind support and education policies have instructed me to become a responsible researcher.

Secondly, I would like to thank Dr. Yuta Hikima. You are always kind to every student in the MPE laboratory, and willing to care about students' daily life and research. You would always discuss with me when I was struggling in the research. Your valuable advice on crystallization and rheology was indeed helpful which provided me a new way of thinking. Your knowledge about crystallization and ideas on thermal analysis have become one of essential parts in the dissertation. Besides, your assistance in booking experiment instruments has promoted the progress of my research.

I am really thankful to Assoc. Prof. Shinsuke Nagamine. You've taught me how to use experiment instruments and provided me some valuable advice on data analysis. I am also grateful to Project-Specific Assist. Prof. Long Wang who has been back to China since October 2019. In my first semester, you gave me many insight comments about the experiments and knowledge about foaming. In daily life, you've provided me great help and suggestions. It reminds me of the days when we have dinner, play badminton and doing experiments together. Without your support, my life of Ph.D. wouldn't be such fulfilling. In addition, I would like to show my gratitude to Prof. Shuji Matsusaka (Department of Chemical Engineering, Kyoto University) for permission to use his laser microscope.

I would like to sincerely thank Mr. Yoshiki Hamamoto, who has given great help in the paper of surface quality improvement. His ideas and thoughts have indeed inspired me, and become one of the key reasons for the paper.

I would like to express my thanks to Ms. Maki Yamamoto in our lab who helped and supported me with office-related procedures which brings great convenience to my daily life. I would also like to thank the former and current students in the MPE laboratory for their help and support during these years.

I feel thankful to my best friends Dr. Jintao Li, Mr. Zirui Lu, Mr. Yan Xu, Dr. Chenchen Liu, etc., who also provide me with great support in Kyoto University.

Finally, I would like to show my sincere gratitude to my family. Their support and encouragement has allowed me to pursue my Ph.D degree in Japan. I would like to show my vehement love to my girlfriend Ms. Huiying Chen, who has given me strong support in my daily life.

Weiyuan Lin

Materials Process Engineering Laboratory, Department of Chemical Engineering
Graduate School of Engineering, Kyoto University

Publication and Conference

Publications

1) "Microcellular foam of styrene–isobutylene–styrene copolymer with N_2 using polypropylene as a crystallization nucleating and shrinkage reducing agent", Weiyuan Lin, Yuta Hikima, Masahiro Ohshima, *Journal of Applied Polymer Science*, vol.139, 40, e52977, https://doi.org/10.1002/app.52977 – Chapter 2

2) "Improvement of the surface quality of foam injection molded products from a material property perspective", Weiyuan Lin, Yoshiki Hamamoto, Yuta Hikima, Masahiro Ohshima, *Polymer Engineering and Science*, Published online, https://doi.org/10.1002/pen.26183 – Chapter 3

3) "Stretching-induced foaming of gas-laden thermoplastic elastomers", Weiyuan Lin, Masahiro Ohshima, *Polymer* (already submitted) – Chapter 4

Conferences

1) "Core-Back Foam Injection Molding of Styrene-Isobutylene-Styrene (SIBS) with N_2 Using Polypropylene as A Nucleating Agent", **Weiyuan Lin**, Long Wang, Yuta Hikima, Masahiro Ohshima, AWPP 2019 in Beijing, 2019, October (poster presentation).
2) "Core-Back Foam Injection Molding of Styrene-Isobutylene-Styrene (SIBS) with N_2 Using Polypropylene as A Nucleating Agent", **Weiyuan Lin**, Yuta Hikima, Masahiro Ohshima, PPS37 in Fukuoka, 2022, April (oral presentation, international conference).
3) 大嶋 正裕, 濵本 禎樹, **Lin Weiyuan**, 引間 悠太、発泡射出成形品の表面粗さの制御、プラスチック成形加工学会　第 33 回年次大会、A-21 2, 2022, June.